Redacted for privacy

Abstract approved:

Timothy C. Kennedy

Cavitation instabilities in elastic-plastic solids under spherically-symmetric and axisymmetric loadings were investigated using the finite element method. Both quasi-static and dynamic analyses were used to solve these problems.

In the quasi-static analyses, we investigated a cavitation instability in elastic/perfectly-plastic, linear hardening elastic-plastic, power hardening elastic-plastic, and constrained silver materials. Here, when the instability occurs, the cavity expands under no change in remote stresses and strains in all cases. In the case of axisymmetric loading on power hardening elastic-plastic material ($\varepsilon_y = 0.003$ and $n = 0.25$), we found good agreement between our FEA solution and the approximate solution (Hou and Abeyaretne, 1992) only when the remote field remained elastic. In the case of axisymmetric loading on constrained silver, we found good agreement between our FEA solution and the experimental results of Kassner et al. (1998). Moreover, a cavitation instability was found for stress ratios, σ_2/σ_1, beyond the range proposed by Kassner et al. (1998), i.e. as low as $\sigma_2/\sigma_1 = 0.5$. Unfortunately, when the stress ratio was small, FEA simulations appeared to have difficulty determining the exact cavitation instability state because the mesh along the boundaries deteriorated very fast during the onset of instability.

In the dynamic analyses, we investigated cavity expansion in incompressible and elastic/perfectly-plastic materials. Both inertia and strain-rate

hardening effects were considered. For dynamic loads below the critical load required for cavitation in the quasi-static case, the cavity expanded rapidly initially but eventually decelerated and stopped at a finite value. For dynamic loads above this critical value, the cavity expanded rapidly initially and then decelerated and settled into expansion at a constant rate. This observation held for both spherically-symmetric and axisymmetric loading.

A Study of Cavitation Instabilities in Solids

by
Tumrong Puttapitukporn

A THESIS

submitted to

Oregon State University

in partial of fulfillment of
the requirements for the
degree of

Doctor of Philosophy

Presented February 27, 2003
Commencement June 2003

Doctor of Philosophy thesis of Tumrong Puttapitukporn presented on February 27, 2003.

APPROVED:

Redacted for privacy

Major Professor, representing Mechanical Engineering

Redacted for privacy

Chair of Department of Mechanical Engineering

Redacted for privacy

Dean of Graduate School

I understand that my thesis will become part of the permanent collection of Oregon State University libraries. My signature below authorizes release of my thesis to any reader upon the request.

Redacted for privacy

Tumrong Puttapitukporn, Author

ACKNOWLEDGMENTS

TABLE OF CONTENTS

TABLE OF CONTENTS (Continued)

LIST OF FIGURES

LIST OF TABLES

A STUDY OF CAVITATION INSTABILITIES IN SOLIDS

1. INTRODUCTION

Interlayers consisting of thin (e.g. 1 μm-1mm) and soft ductile material welds, bonds, or brazes between strong base materials, when tested in tension, may exhibit high ultimate tensile strength despite the relatively low strength of the interlayer material. This strength is due to the mechanical constraint provided by the stronger base material that restricts the transverse contraction of the interlayer. This constraint produces a substantial triaxial stress state within the interlayer and reduces the effective Von Mises stress, thus reducing the tendency of the interlayer to plastically deform and fracture in the ductile manner. Although the explanation for the increased ductile fracture stress is reasonable, the low plastic strain to failure is still unclear.

These fracture mechanisms were recently studied by Kassner et al. (1998), for ductile fracture in thin, constrained silver films. They proposed that this fracture results from cavitation instabilities. Here, cavities grow without the necessity for continual increase in remote stress and without substantial far-field plastic strain. Furthermore, their finite element analysis showed that unstable cavity growth could be extended to some axisymmetric stress states where the ratio of the radial stress or the hoop stress $(\sigma_2 \cong \sigma_3)$ to the normal stress, σ_1, is greater than 0.65. This is beyond the range of the stress ratio, σ_2/σ_1, proposed by Haung et al. (1991) in which $\sigma_2/\sigma_1 > 0.75$.

The purpose of this dissertation is to study: (1) the mechanism of ductile fracture related to cavitation instabilities under both spherically-symmetric and axisymmetric loading, (2) the range of applied triaxial stress stages, σ_2/σ_1, in which the unstable cavity growth can occur, and (3) the dynamic effects on prediction of

cavitation instabilities, including rate-sensitive plasticity and inertia. Both analytical and finite element techniques are used in developing the solutions.

2. LITERATURE REVIEW

Cavitation in solids has been observed in experiments of metals under many circumstances, i.e. Yerzley (1939), Gent and Lindley (1958), and recently Kassner et al. (1998). However, mathematical models of cavitation instabilities have been developed to elucidate this phenomenon since 1948. The objective of this chapter is to review the mathematical formations and FEA analyses relevant to cavitation instabilities in which a cavity contained inside an infinite solid medium can expand unstably under no change in applied loading. Particular focus was given to both quasi-static and dynamic analyses.

2.1 QUASI-STATIC ANALYSIS OF CAVITATION INSTABILITIES IN ELASTIC-PLASTIC SOLIDS

Quasi-static analysis is a well-known method in analyzing structural responses when the frequency of excitation applied to the structure is less than roughly one-third of the structure's lowest natural frequency of vibrating. Consequently, the effects of inertia can be neglected and the structure is, therefore, in static equilibrium.

The analysis is divided into two groups by loading conditions: spherically-symmetric loading and axisymmetric loading. In spherically-symmetric loading, the load is applied in the radial direction of a spherical cavity. This is a simplified version of the axisymmetric loading, and it is easy to analyze because the equations can often be integrated explicitly. In the other, the load applied in the axial direction of the cavity is generally different from load in the radial direction.

Hill (1950) pioneered developing the mathematical method for an expansion of a spherical cavity in an infinite solid medium in which pressure, p, is applied gradually to the cavity surface so that the dynamic effects can be negligible.

The material is assumed to be an isotropic and elastic/perfectly plastic solid. The generalized coordinates were chosen to be the spherical coordinates, r, θ, and ϕ. To calculate the large strains in the plastic zone (after the onset of yielding on the cavity surface), he introduced the incremental displacement of a particle as

$$du = \frac{\partial u}{\partial c} dc + \frac{\partial u}{\partial r} dr = \left(\frac{\partial u}{\partial c} dc + \upsilon \frac{\partial u}{\partial r} \right) dc, \tag{2.1}$$

where r is the radial distance to a particle in the plastic zone, c is the radius of plastic zone, and υ is the velocity of a particle. Both r and c are taken as the independent variables. The increments of stress and strain could be written as

$$d\varepsilon_r = \frac{\partial}{\partial r}(du) = \frac{\partial \upsilon}{\partial r} dc,$$

$$d\varepsilon_\theta = d\varepsilon_\phi = \frac{du}{dr} = \frac{\upsilon dc}{r},$$

$$d\sigma_r = \left(\frac{\partial \sigma_r}{\partial c} dc + \upsilon \frac{\partial \sigma_r}{\partial r} \right) dc,$$

$$d\sigma_\theta = d\sigma_\phi = \left(\frac{\partial \sigma_\theta}{\partial c} dc + \upsilon \frac{\partial \sigma_\theta}{\partial r} \right) dc. \tag{2.2}$$

The compressibility condition gives

$$d\varepsilon_r + d\varepsilon_\theta + d\varepsilon_\phi = \frac{1-2v}{E}(d\sigma_r + d\sigma_\theta + d\sigma_\phi). \tag{2.3}$$

where v is Poisson's ratio and E is Young's Modulus. Substituting equation (2.2) into (2.3) and integrating lead to the relationship between c and the deformed cavity radius, a, as

$$\frac{c}{a} = \left\{ \frac{E}{3(1-v)Y} \right\}^{\frac{1}{3}}, \tag{2.4}$$

and the approximation of the threshold pressure, p_∞, at which the cavity grows without bound as

$$p_\infty = \frac{2Y}{3} \left\{ 1 + \ln\left(\frac{E}{3(1-\upsilon)Y} \right) \right\}, \tag{2.5}$$

where Y is the yield stress. He also extended his analysis to include a work-hardening medium. For simplification, the stress-strain curve of the material in compression is taken to be of the form

$$\sigma = Y + H(\varepsilon),$$
(2.6)

where H is the amount of hardening expressed as a function of the logarithmic total equivalent strain, ε. In the case when a cavity is expanded from zero radius in an infinite medium, he arrived with the approximation of p_∞ as

$$p_\infty = \frac{2Y}{3}\left\{1+\ln\left(\frac{2E}{3+2Y}\right)\right\} + 2\int_1^{c/a} H\left\{\frac{2}{3}\ln\left(\frac{z^3}{z^3-1}\right)\right\}\frac{dz}{z},$$
(2.7)

where $z = \dfrac{r}{a}$.

In particular, if $H \equiv H'\varepsilon$ where H' is a constant rate of hardening, Bishop et al. (1945) have shown that

$$p_\infty = \frac{2Y}{3}\left[1+\ln\left(\frac{2E}{3Y}\right)\right] + \frac{2\pi^2 H'}{27}.$$
(2.8)

Chadwick (1957) modified the work done by Hill (1950) in the area of the treatment of the large displacement in the plastic zone after the onset of yielding. He introduced the logarithmic strain,

$$\varepsilon_r = \ln\left(\frac{dr}{dr_0}\right) = \frac{du}{dr} + \frac{1}{2}\left(\frac{du}{dr}\right)^2 + ...,$$

$$\varepsilon_\theta = \ln\left(\frac{r}{r_0}\right) = \frac{u}{r} + \frac{1}{2}\left(\frac{u}{r}\right)^2 + ...,$$
(2.9)

where

$$r = u + r_0.$$
(2.10)

The expression of the deformed cavity radius, a, as a function of the cavity pressure, p, was written as

$$a = a_0 \exp\left(\frac{1}{3} - \frac{p}{2Y}\right)\left[\left(1-\delta\right)^{-1}\left\{\exp\left(\delta-1\right)\left(\frac{3p}{2Y}-1\right)\right\} + \left(1-\varepsilon\right)^3\right]^{-\frac{1}{3}}, \quad (2.11)$$

where

$$\delta = \frac{2}{E}(1-2v),$$
$$\varepsilon = \frac{Y}{3E}(1+v), \quad (2.12)$$

and a_0 is the initial cavity radius. A plot of cavity expansion versus load factor p/Y in a medium of heavily cold work copper assuming no work-hardening (with $Y/E = 2.19 \times 10^{-3}$ and $v = 0.34$) is shown in Figure 2.1. It was also found; in particular, that the radius of the cavity increases indefinitely as the applied pressure approaches p_∞.

$$p_\infty = \frac{2}{3}Y\left[1 - (1-\alpha)^{-1}\ln\left\{1 - (1-\delta)(1-\varepsilon)^3\right\}\right]. \quad (2.13)$$

This equation is in good agreement with the values obtained from Hill (1950) in equation (2.5). By assuming an incompressible medium and the work-hardening represented by a polynomial expression of the type

$$H\left(\int d\varepsilon^p\right) = \sum_{n=1}^{N} H_n\left(\int d\varepsilon^p\right)^n. \quad (2.14)$$

p_∞ apparently becomes

$$p_\infty = \frac{2}{3}Y\left[1 - \ln(\tau)\right] + \sum_{n=1}^{N}\left(\frac{2}{3}\right)^{n+1} n!\zeta(n+1), \quad (2.15)$$

where $\tau = 1 - (1-\varepsilon)^3$ and ζ is the Reimann zeta function (Appendix A). In the case of linear work-hardening, $N = 1$ and $\zeta(2) = \frac{1}{6}\pi^2$, and

$$p_\infty = \frac{2}{3}Y\left[1 - \ln(\tau)\right] + \frac{2}{27}\pi^2 H_1, \quad (2.16)$$

where H_1 is the linear work-hardening constant. This equation is the same as in equation (2.8) presented by Bishop, Hill, and Mott (1945).

The Quasi-Static Analysis of Cavity Expansion in Copper
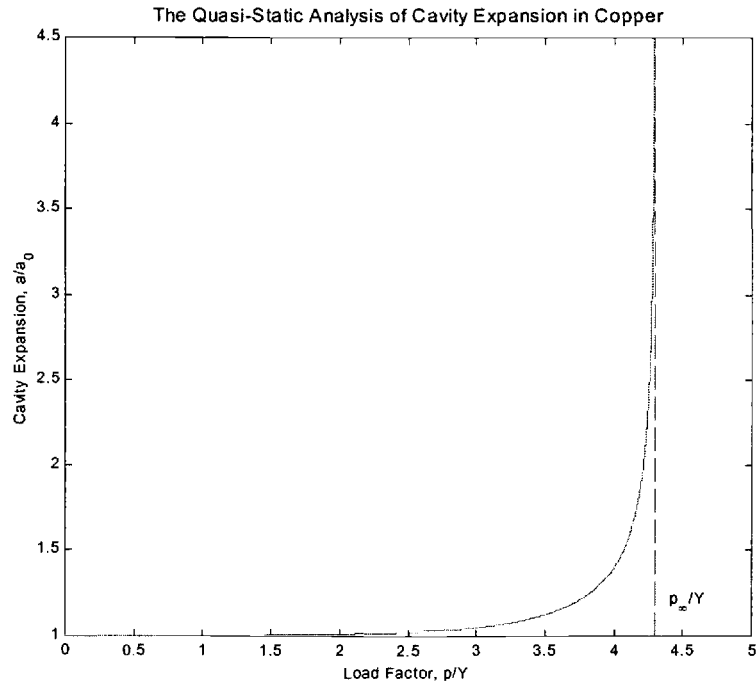
Figure 2.1 Cavity expansion vs. load factor in copper without work-hardening in a medium of cold-worked copper.

McClintock (1968) investigated the expansion of a long cylindrical hole in a elastic/perfectly plastic solid. He determined the relationships of the void growth rate, $\dot{b}/b$, on the imposed axial strain rate, $\dot{\varepsilon}$, and the transverse stress, σ_∞, as shown in Figure 2.2. The cylindrical void has the initial radius, r_0, and the current radius, b. The analysis was performed using the stress-strain relationships of elastic-plastic system associated with the von Mises yield criterion. He finally obtained

$$\frac{\dot{b}}{b} = \frac{\sqrt{3}}{2}\sinh\left(\frac{\sigma_\infty}{\sqrt{3}Y}\right) - \frac{1}{2}.$$

(2.17)

This equation shows an exponential increase in the void growth rate with positive transverse stress.
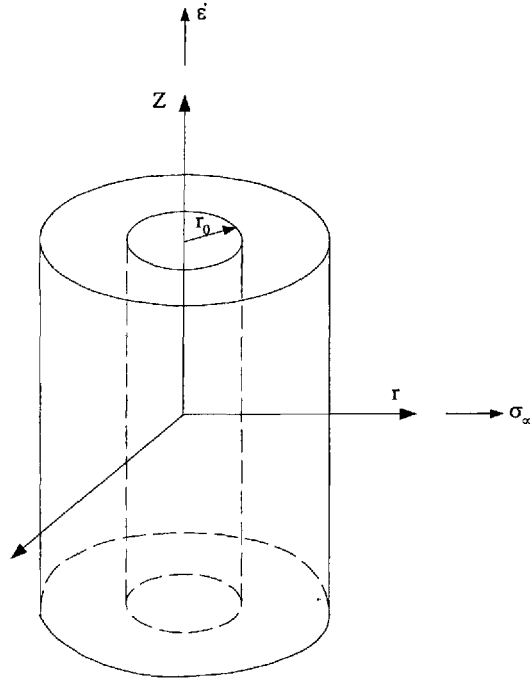
Figure 2.2 Long cylinder void extended along the r and z-axis.

Rice and Tracey (1969) studied the ductile enlargement of voids in a triaxial stress field in an infinite body under an axisymmetric strain field $\dot{\varepsilon}$ as shown in Figure 2.3. To simplify their analysis, they assumed that the material was incompressible, rigid-plastic. If $\dot{\varepsilon}_3^\infty = \dot{\varepsilon}$, then the incompressibility requires

$$\dot{\varepsilon}_1^\infty = \dot{\varepsilon}_2^\infty = -\dot{\varepsilon}/2.$$

They solved this problem using the Rayleigh-Ritz method. This involves choosing mathematical functions that are capable of approximation the true solution. These functions contain parameters that are optimized (though a variational formula) so that the approximate solution comes as close as it possibly can to the true solution.
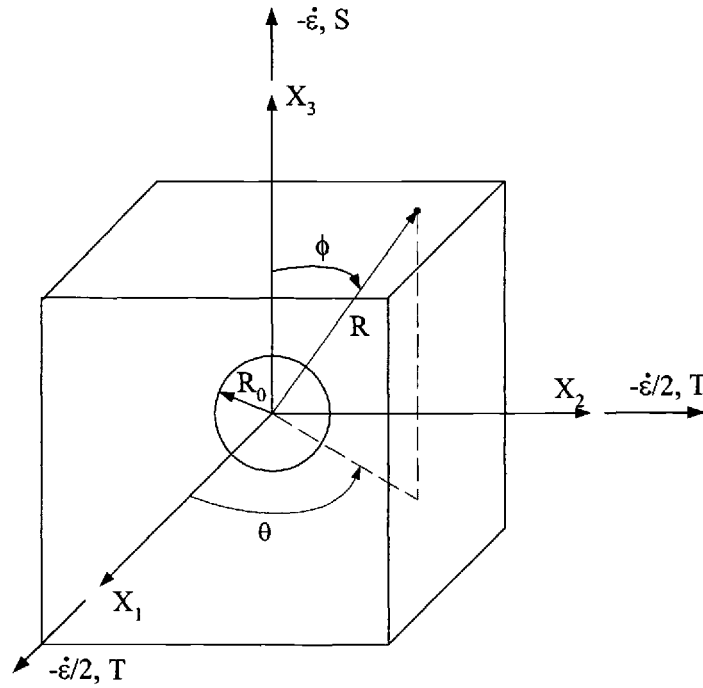
Figure 2.3 Spherical void in a remote simple tension rate field. Applied tensile loads are T and S.

The approximate velocity field is chosen as

$$\dot{u}_i = \dot{\varepsilon}_{ij}^{\infty} x_j + D\dot{u}_i^D + E\dot{u}_i^E, \tag{2.18}$$

where D and E are constants to be determined, $\dot{u}_i^D$ is a spherically-symmetric volume changing field, and $\dot{u}_i^E$ is a shape changing field which preserves void volume.

The first term of the above equation is a uniform strain field and represents the solution for points in the body far from the cavity. The second term represents a spherically-symmetric velocity field corresponding to a change in volume of the cavity but no change in shape. They used the following mathematical function to represent $\dot{u}_i^D$ as

$$\dot{u}_i^D = \dot{\varepsilon}\left(\frac{R_0}{R}\right)^3 x_i. \tag{2.19}$$

The term D that multiplies this is the parameter that will be optimized to get the best possible approximation. The third term represents a velocity field that changes the void shape but not its volume. The mathematical functions chosen for this are fairly complicated. This term was found to have a small effect on the overall solution. Therefore, it will not be considered in detail. E is the parameter to be optimized to get the best possible approximation.

They assumed that the volume changing part of void growth far overwhelms the shape changing part when the remote mean stress is large. The closed form approximate formula for D is obtained by substituting equation (2.18) (without the third term) into the variational formula, which yields

$$D = 0.283\exp\left(\frac{\sqrt{3}\sigma_m}{2\tau_0}\right), \tag{2.20}$$

or $\quad \dfrac{\dot{R}_0}{R_0} = 0.283\dot{\varepsilon}\exp\left(\dfrac{\sqrt{3}\sigma_m}{2\tau_0}\right), \tag{2.21}$

where $\dot{R}_0$ is the average radial velocity of the cavity boundary, σ_m is the mean remote normal stress and τ_0 is the yield stress in shear. The plot of D as a function of σ^∞/τ_0 is shown in Figure 2.4.
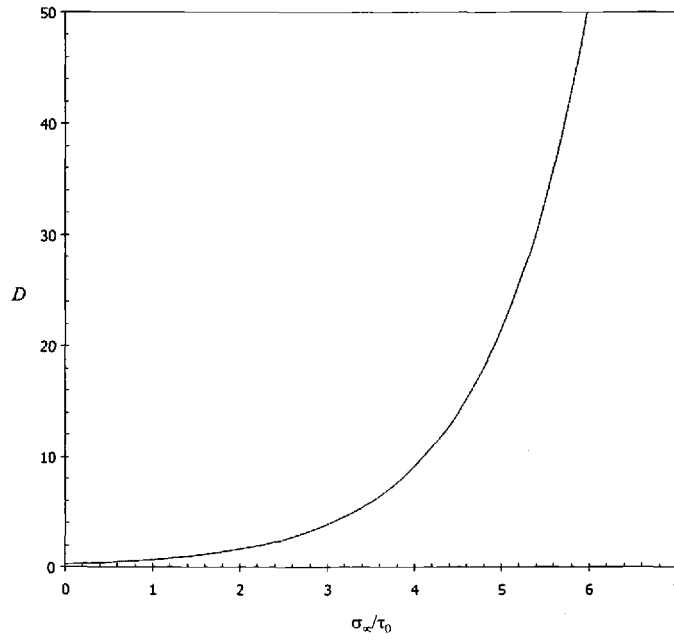
Figure 2.4 High triaxiality solution of Rice and Tracey. Radial expansion of a cavity is exponentially related to the mean stress/yield stress ratio.

Schrems (1999) extended the work of Rice and Tracey to determine the relationships between the remote final strain, ε_f, and the triaxiality,

$$\Sigma = T/S,$$ (2.22)

as a function of the cavity expansion. S and T are the remote axial stress and the remote radial stress respectively. By assuming an incompressible solid medium, the mean stress, σ_m, can be given by the Tresca yield criterion as

$$\sigma_m = \frac{\sigma_1 + \sigma_2 + \sigma_3}{3} = \frac{1 + 2\Sigma}{3(1 - \Sigma)} Y.$$ (2.23)

According to the von Mises yield criterion for the uniaxial tension in the remote field, τ_0 can be expressed as

$$\tau_0 = \frac{Y}{\sqrt{3}}.$$ (2.24)

She substituted equations (2.23) and (2.24) into the high triaxiality equation (2.21) presented by Rice and Tracey (1969). After evaluating the integrations, she finally obtained

$$\varepsilon_f = 3.534 e^{-\frac{1+2\Sigma}{2(1-\Sigma)}} \ln \frac{R_f}{R_i}, \tag{2.25}$$

where the subscript i and f represent an initial and final state respectively. For example, to expand the cavity by a factor of 100, the remote strain is

$$\varepsilon_f = 16.275 e^{-\frac{1+2\Sigma}{2(1-\Sigma)}}. \tag{2.26}$$

Radial cavity expansion by a factor of 100, 5, and 1.6 is shown graphically in Figure 2.5. It is found that strain decreases rapidly as the triaxiality increases.
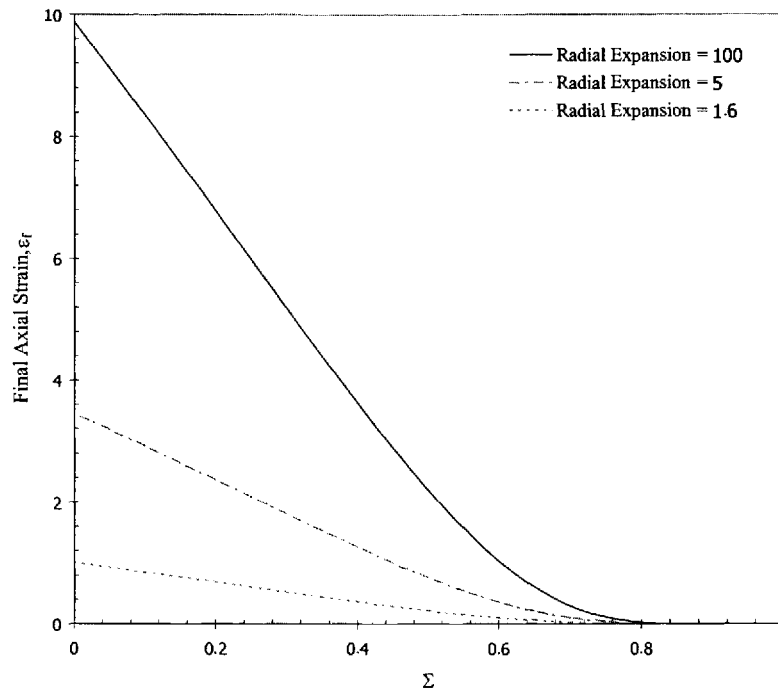
Figure 2.5 The remote axial strain vs. the triaxiality as a function of the cavity expansion.

Huang et al. (1991) studied cavitation instabilities in an infinite elastic-plastic solid. Later, Tvergaard et al. (1992) extended their work (Huang et al., 1991) to account for a power hardening elastic-plastic solid. The cavitation instabilities occur when an isolated void in an infinite, remotely stressed elastic-plastic solid, grew without bound under no change of remote stress or strain. They studied the problem for cavitation states under both spherically-symmetric stress and under general axisymmetric stress.

In the case of the spherically-symmetric cavitation state, the material was assumed an isotropic, incompressible elastic-plastic solid. Using the equilibrium equation and integrating with the boundary conditions, they obtained

$$\frac{\sigma^{\infty}}{Y} = -2\int_{1}^{\infty} f\left[\frac{2}{3}\ln\left\{1-\frac{1-R_i/R_0}{\eta^3}\right\}\right]\frac{d\eta}{\eta}.$$ (2.27)

The cavitation limit stress, $\sigma^{\infty} \equiv S_{cr}$, was obtained from equation (2.27) by letting $R_0/R_i \to \infty$; i.e,

$$\frac{S_{cr}}{Y} = -2\int_{1}^{\infty} f\left[\frac{2}{3}\ln\left\{1-\eta^{-3}\right\}\right]\frac{d\eta}{\eta},$$ (2.28)

$$= -\int_{0}^{\infty}\left[e^{3\xi/2}-1\right]^{-1} f(-\xi)d\xi.$$ (2.29)

The cavity limit exists if $e^{-3\xi/2}f(-\xi)$ can be integrate. Consider an elastic-perfectly plastic material with an initial tensile yield strain, ε_y. A direct evaluation of equation (2.29) gives

$$S_{cr}/Y = \frac{2}{3}\int_{0}^{1}\ln\left[1-e^{-3\varepsilon_y\xi/2}\right]d\xi,$$ (2.30)

$$= \frac{2}{3}\left\{1+\ln\left(\frac{2}{3\varepsilon_y}\right)\right\}+O(\varepsilon_y).$$ (2.31)

The approximation in equation (2.31) is obtained from the exact expression in equation (2.30) using $1-\exp\left(-3\varepsilon_y\xi/2\right) \cong 3\varepsilon_y\xi/2$. This is accurate for $\varepsilon_y < 0.01$. The radius of the plastic zone, R_y, satisfies

$$\ln\left(\frac{R_y}{R_0}\right) = \frac{1}{2}\frac{\sigma^\infty}{\sigma_y} - \frac{1}{3}. \tag{2.32}$$

In the limiting cavitation state, equation (2.31) gives

$$R_y / R_0 \cong \left(3\varepsilon_y / 2\right)^{-1/3}. \tag{2.33}$$

Equations (2.31) and (2.33) are given by Hill (1950). The plastic zone has a fixed size relative to the current size of the cavity (typically 4 to 8 times the current radius of the cavity, depending on ε_y). Outside the plastic zone is an elastic field in which the strains diminish to zero as R^{-3}.

Next, they considered a power-law hardening solid with

$$\begin{aligned}
\sigma / Y \equiv f(\varepsilon) &= \varepsilon / \varepsilon_y, \text{ when } |\varepsilon| \le \varepsilon_y, \\
&= sign(\varepsilon)\left(|\varepsilon|/\varepsilon_y\right)^N, \text{ when } |\varepsilon| > \varepsilon_y.
\end{aligned} \tag{2.34}$$

Values of S_{cr} / Y were obtained numerically from equation (2.29). The relationship between σ^∞ / Y and R_0 / R_i from equation (2.27) is plotted in Figure 2.6 for $N = 0$, 0.1, 0.2, and 0.3. The cavitation limit stress is approached rapidly and is effectively attained once the void has expanded to about three times its original radius.

When the material is elastically compressible the analysis is not so simple but some specific results can be obtained. In particular the limit yield stress for the elastic-perfectly plastic solid with Poisson's ratio, ν, is

$$\begin{aligned}
\frac{S_{cr}}{\sigma_y} = &-\frac{2}{3\alpha}\ln\left\{1 - \alpha e^{-(1+\nu)\varepsilon_y}\right\} \\
&+ \frac{2(1-\nu)}{(1+\nu)\varepsilon_y}\int_0^{(1+\nu)\varepsilon_y} \xi\left[(1+\nu)\left(e^\xi - 1\right) + 2(1-2\nu)\xi\right]^{-1} d\xi,
\end{aligned} \tag{2.35}$$

where $\alpha = 1 - 2(1-2\nu)\varepsilon_y$. With terms of order ε_y and smaller neglected, equation (2.35) becomes

$$\frac{S_{cr}}{\sigma_y} = -\frac{2}{3\alpha}\left\{1 + \ln\left(\frac{1}{3(1-\nu)\varepsilon_y}\right)\right\}. \tag{2.36}$$

This equation is the same as equation (2.5) presented by Hill (1950).
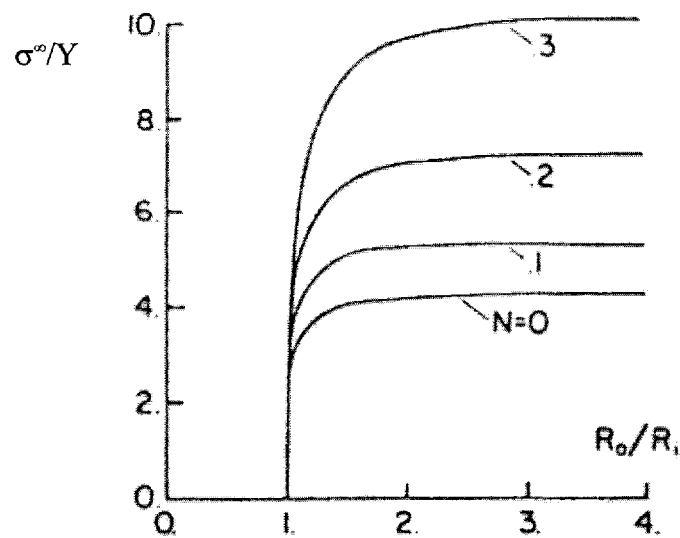
Figure 2.6 Remote stress vs. radius of the cavity for the spherically-symmetric loading.

In the case of axisymmetric loading, they solved the problem by coupling an analytical solution for points away from the cavity to a finite element solution for points near the cavity. They solved the problem for two cases: (1) when the far–field state is elastic, and (2) when the far-field state is plastic. These results are shown in Figure 2.7. The solid lines on the left hand side of the dashed line represent the results when the far-field state is elastic. The others represent the results when the far-field state is plastic.
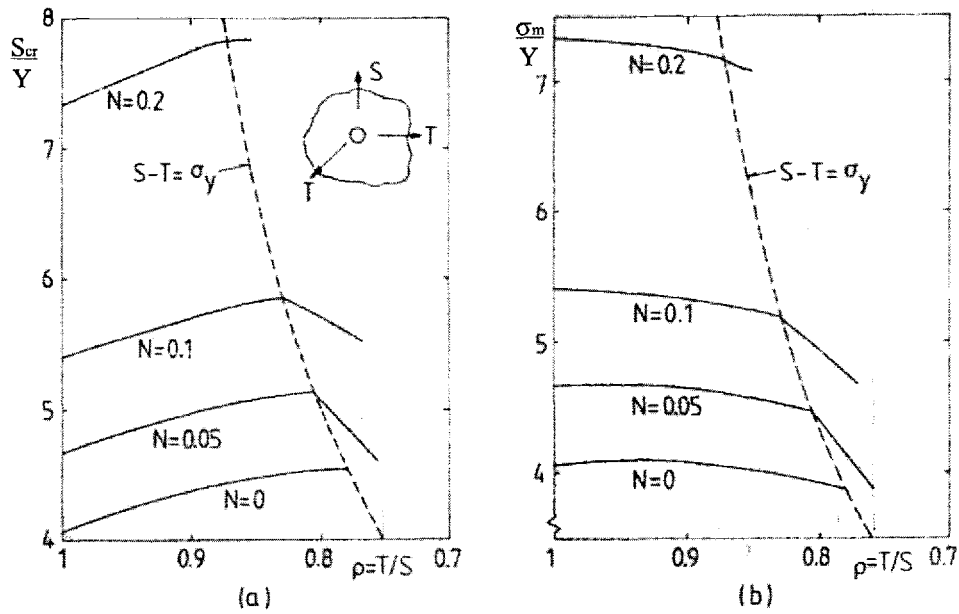
Figure 2.7 Cavitation limits for a spherical void in elastic-plastic power hardening solid subjected to remote axisymmetric stressing ($Y/E = 0.003$ and $v = 0.3$). (a) Axial tensile stress; (b) Mean stress.

Hou and Abeyaratne (1992) examined the phenomenon of cavitation under axisymmetric loading. They seek all points in ($\sigma_1, \sigma_2, \sigma_3$) stress space, such that, when the local principal true stress components ($\sigma_1, \sigma_2, \sigma_3$) at a particle reach a point on that set, cavitation ensues. This set can be described by a surface $\varsigma(\sigma_1, \sigma_2, \sigma_3) = 0$ in stress space, which is referred to as a cavitation surface, and corresponds to a cavitation criterion that arises naturally from the analysis. In the case of a piecewise power-law elastic material, the agreement of cavitation between their approximate criterion and Tvergaard et al. (1992) is good only if the cavitation occurs before yielding in the remote field.

Since determining an exact solution of the non-linear field equations and non-symmetric boundary conditions was difficult, they focused attention instead on finding an approximate solution. By considering a particular subclass solution of

the set of all kinematically admissible deformation fields, they found an approximate solution by construction of a three-parameter family of deformation fields, with parameters β (representing the cavity size), α_2 and α_3 (representing the overall ratios of cavity), and obtained three algebraic equations for determining these three constants:

$$\sigma_1 + \sigma_2 + \sigma_3 = \frac{3}{4\pi\beta^2} \frac{\partial \xi(\beta,\alpha_2,\alpha_3)}{\partial \beta}, \tag{2.37}$$

$$\sigma_2 - \sigma_1 = \frac{3\alpha_2}{4\pi(1+\beta^3)} \frac{\partial \xi(\beta,\alpha_2,\alpha_3)}{\partial \alpha_2}, \tag{2.38}$$

$$\sigma_3 - \sigma_1 = \frac{3\alpha_3}{4\pi(1+\beta^3)} \frac{\partial \xi(\beta,\alpha_2,\alpha_3)}{\partial \alpha_3}, \tag{2.39}$$

where $\xi(\beta,\alpha_2,\alpha_3)$ is the total internal energy stored in the body corresponding to the three-parameter deformation field. In the case of axisymmetric cavitation, the deformation field is assumed axisymmetric. Consequently, the overall ratios of cavity can be written as

$$\alpha = \alpha_2 = \alpha_3. \tag{2.40}$$

The occurrence of cavitation can be described by a cavitation curve in the (σ_1,σ_2)-plane when $\beta = 0$. Substituting equation (2.40) into (2.37)-(2.39) and manipulating, there results

$$\sigma_m = \left(\frac{1}{4\pi\beta^2} \frac{\partial \xi(\beta,\alpha)}{\partial \beta} \right)\Bigg|_{\beta=0}, \tag{2.41}$$

$$\sigma_1 - \sigma_2 = \frac{3\alpha_2}{8\pi} \frac{\partial \xi(\beta,\alpha)}{\partial \alpha}\Bigg|_{\beta=0}, \tag{2.42}$$

where σ_m is the mean stress. The total energy can be written as

$$\xi(\beta,\alpha) = 2\pi \int_0^\pi \int_0^1 \int_0^{\varepsilon_e} f(\varepsilon) d\varepsilon R^2 dR \sin\theta d\theta,$$

$$\sigma = f(\varepsilon), \tag{2.43}$$

$$R = \sqrt{x_1^2 + x_2^2 + x_3^2},$$

where ε_e is the equivalent strain; f characterizes the response of the material in uniaxial tension as a function of the logarithmic strain, ε; x_1, x_2, and x_3 are the location of a particle in the reference configuration. Then, they evaluated the integrals, which result from substituting equation (2.43) into (2.41) and (2.42), numerically. The cavitation curves associated with different values of the initial yield strain, ε_y, at a fixed value of the hardening exponent are illustrated in Figure 2.8. Figure 2.9 depicts the cavitation curves associated with different values of ε_y at a fixed value of hardening exponent. It is seen that, as ε_y decreases, the critical stress-levels increase.
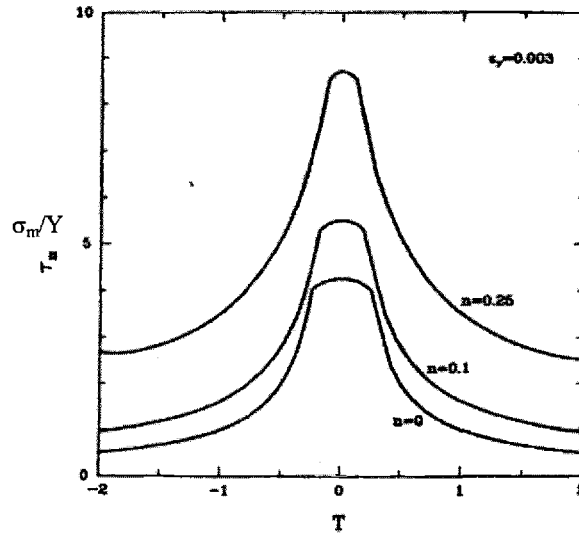
Figure 2.8 Cavitation curves for elastic-plastic materials on (σ_m, T) plane, where for different yield strains $|T|$ is the triaxiality. The hardening exponent is n and $n = 0$ coresponds to an elastic/perfectly-plastic material.
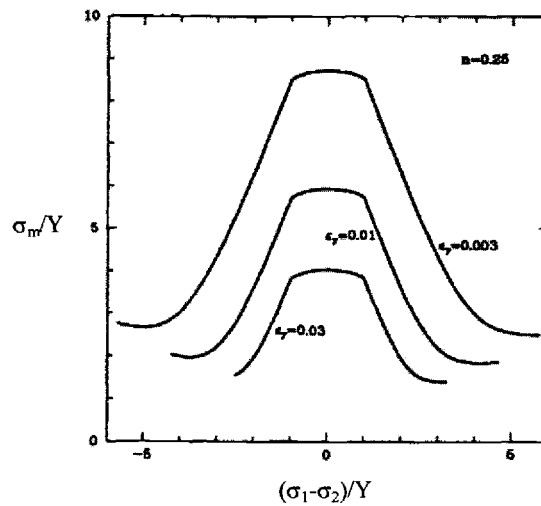
Figure 2.9 Cavitation curves for elastic-plastic materials for different yield strains ε_y. $\varepsilon_y = 0$ corresponds to a rigid-plastic material.

Kassner et al. (1998) studied cavitation instabilities in constrained thin silver film in both experiments and a finite element analysis. They demonstrated that the cavities growth without the necessity for continued increase in remote stress and without substantial far-field plastic strain. In the finite element analysis, they used a pure finite element analysis approach (near field) with an arc-length solver capable of handling limit points.

The finite element analysis of an axisymmetric model composed of a single cavity contained in a finite body was performed where the outer boundaries were 300 cavity radii from the cavity radius. The finite element mesh consisted of 400 elements graded with a fine mesh near the cavity and a coarse mesh away from the cavity. The model was simulated using a quarter-symmetry mesh in the finite element code, ANSYS. Unstable cavity growth was assumed to occur when the cavity continued to expand without increase in remote stress or strain. This approach gave results that were with in 1% of those reported by Tvergaard et al. (1992). Moreover, they showed that unstable cavity growth such as described by Tvergaard et al. (1992) can be extended to at least some axisymmetric stress states

where $\sigma_2/\sigma_1 < 0.75$. Figure 2.10 shows the expansion of a single cavity versus remote axial strain for various axisymmetric triaxial stress states for silver. Figure 2.11 illustrates the maximum principal stress, σ_1, versus the corresponding σ_2/σ_1 at which an isolated cavity will growth without further increases in far-field stresses. Here, the agreement between FEA predicted stresses and straines for instability are in reasonable agreement with the experimental values.

(a)
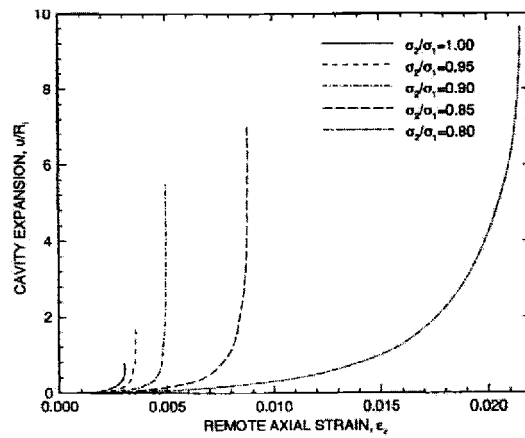
(b)
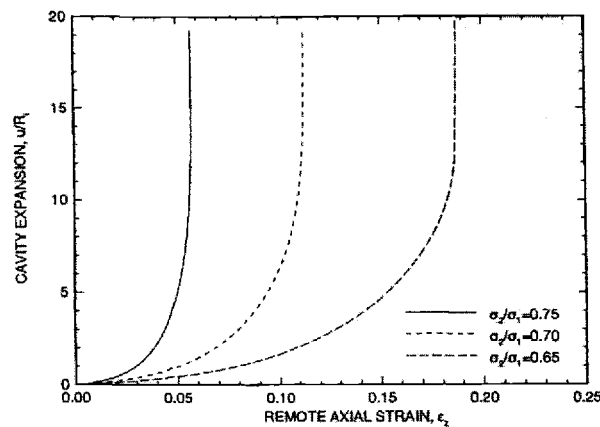
Figure 2.10 Single cavity expansion vs. remote axial strain for (a) axisymmetric loading at a silver interlayer for $\sigma_2/\sigma_1 \geq 0.8$, (b) $\sigma_2/\sigma_1 \leq 0.75$.
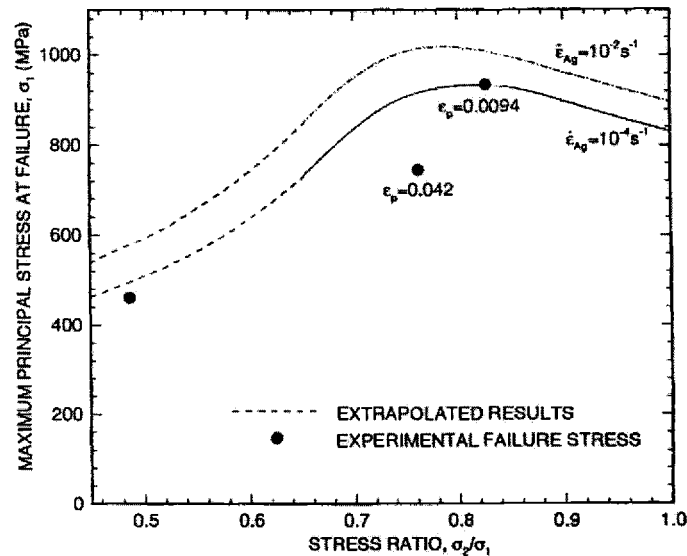
Figure 2.11 The FEA predicted maximum principal stress for failure vs. σ_2/σ_1 based on unstable expansion of isolated at two strain rates. The predicted plastic strains to failure are also reported. The experimental stresses for ductile fracture are indicated.

Tvergarrd (1999) extended the work of Tvergaard et al. (1992) to consider the effect of a large initial yield strain on a power hardening elastic-plastic material. It was shown how the critical stress value decayed for increasing value of the yield strain. Analyses were carried out for remote spherically-symmetric tension as well as for more general axisymmetric remote stress field, with an initially spherical void. Different levels of strain hardening were also considered.

2.2 DYNAMIC ANALYSIS OF CAVITATION INSTABILITIES IN ELASTIC-PLASTIC SOLIDS

The dynamic analysis of spherical cavity formation has been recognized as having complex general governing equations. A further important complication is that under the practical conditions of cavity formation due to high-explosive action

some return motion following the important first expansion phase is to be expected. As a result, some simplifying assumptions must be made if analytical solutions are required. Otherwise, purely numerical solutions of the integration of the governing equations need to be developed. Since cavitation instabilities are determined only by the analysis of the first phase expansion, this literature review will be confined to this analysis.

Hill (1948) pioneered the development of mathematical models of the dynamics of cavity formation from zero radius. He focused attention on deriving general conclusions concerning earth movement near a deep underground explosion. However, his theory is limited to frictionless solids such as fully saturated clays, because otherwise the correct yield criterion is that of Coulomb rather than that of Tresca. In particular, for the case of an incompressible and elastic/perfectly plastic material, the equation of motion of plastic-elastic response was written as

$$P(t) = \frac{2}{3}Y\left\{1 + \ln\left(\frac{2\mu}{Y}\right)\right\} + \rho(a\ddot{a} + \tfrac{3}{2}\dot{a}^2),\tag{2.44}$$

in which cavity pressure, $P(t)$, related with cavity radius, $a(t)$, and its time derivative where Y is yield stress, ρ is density, and μ is shear modulus.

Hoskins (1960) developed the mathematical procedures for analyzing dynamic expansion of a spherical cavity in an infinite solid medium subjected to a known function of internal pressure, $P(t)$, on the current cavity surface. He focused his analysis on the first phase of expansion and also the nature of the return motion following the first expansion phase. To simply his analysis, he assumed that material is incompressible and elastic-perfectly plastic. The incompressibility condition eliminates the wave effects of the elastic region from the analysis. By using the conservation of mass and the hypothesis of the constant density, ρ, of the medium, he showed that the particle velocity, υ, could be determined in terms of the velocity of the cavity surface, $\dot{a}$, as

$$\upsilon = \frac{a^2 \dot{a}}{r^2},$$
(2.45)

where a is the current cavity radius. The equation of motion of the elastic response was obtained as

$$\sigma_r = -\frac{4}{9}E\frac{a^3 - a_0^3}{r^3} - \rho\left\{\left(a^2\ddot{a} + 2a\dot{a}\right)/r - a^4\dot{a}^2/2r^4\right\} + f(t),$$
(2.46)

where $f(t)$ is an arbitrary function. However, if the radial stress, σ_r, is taken to vanish at infinity, then $f(t) \equiv 0$. Consequently, equation (2.46) simplifies to that cavity pressure, $P(t)$, can be written as

$$P(t) = \tfrac{4}{9}E\left(1 - a_0^3/a^3\right) + \rho\left(a\ddot{a} + \tfrac{3}{2}\dot{a}^2\right).$$
(2.47)

This equation is subjected to the initial conditions, $a = a_0$ and $\dot{a} = 0$ at $t = 0$. It is valid throughout the elastic response. He also found, in particular, that the onset of yielding at the cavity surface was quite independent of inertia effects. For the plastic-elastic response, the equations of motion were given by the same procedures as equation (2.46), but, instead, there was one equation for each region: a plastic and elastic region. Moreover, the radial stress, σ_r, must be continuous across the plastic-elastic boundary at $r = c$ so that the equation of motion becomes

$$P(t) = \tfrac{2}{3}Y + \tfrac{2}{3}\ln(c/a) + \rho\left(a\ddot{a} + \tfrac{3}{2}\dot{a}^2\right).$$
(2.48)

In this equation, the first two terms correspond the quasi-static result, and the remaining term represents the modification due to inertial effects. The requirement that elastic material at the plastic-elastic boundary is just about to yield is

$$\frac{a^3 - a_0^3}{c^3} = \frac{3Y}{2E},$$
(2.49)

Substituting equation (2.49) into (2.48) yields

$$P(t) = \frac{2}{3}Y\left(1 + \ln\left\{\frac{2E}{3Y}\left(1 - \frac{a_0^3}{a^3}\right)\right\}\right) + \rho\left(a\ddot{a} + \tfrac{3}{2}\dot{a}^2\right).$$
(2.50)

This equation is subjected to the initial conditions determined by equation (2.46) at the time of the initial yielding on the cavity surface.

Hunter and Crozier (1968) studied the similarity solution for the rapid uniform expansion of a spherical cavity from zero initial radius in a compressible elastic-plastic solid. Their motivation was that the incompressible theory could lead to supersonic value of interface velocity, $\dot{b}$ (≈ 5 times of cavity velocity in general solid material) for values of cavity velocity, $\dot{a}$, in excess of one-fifth the velocity of small amplitude plastic wave. Such behavior is unacceptable in the context of an incompressible approximation. Other nonphysical features of the incompressible model are the instantaneous transmission of energy to the remote regions and the complete failure of the continuous velocity field to allow for a description of the shock discontinuities that arise in real material.

Unfortunately, the introduction of compressibility precludes the possibility of obtaining a completely general solution for arbitrary monotonic $a(t)$, and it becomes necessary to specify initially the form of $a(t)$. So, they introduced the simplest cavity expansion as

$$a = \upsilon t, \tag{2.51}$$

where υ is the constant velocity of expansion and t is time. For the case of equation (2.51), the problem admits a similarity solution in which stress, density and velocity depend on a single similarity variable

$$\xi = rt^{-1}. \tag{2.52}$$

Consequently, the governing partial differential equations reduced to ordinary nonlinear differential equations; for the small values of υ the latter may be solved analytically, while for larger value it is necessary to resort to numerical methods of integration.

Substituting $\ddot{a} = 0$ and $\dot{a} = \upsilon$ into equation (2.5) given by Hill (1948) reduces to

$$P(\upsilon) = \tfrac{2}{3}Y\left\{1 + \ln\left(2\mu/Y\right)\right\} + \tfrac{3}{2}\rho\upsilon^2, \tag{2.53}$$

and the predictions of the compressible theory were compared directly with this result. They found from the compressible theory that

$$P = \rho c^2 \left[\exp\left\{ p_\infty / \rho c^2 + (\upsilon/c)^2 K(\upsilon/c, \nu, Y/\rho c^2) \right\} - 1 \right], \qquad (2.54)$$

where ν is Poisson's ratio, c is the velocity of small amplitude plastic waves, and p_∞ is the threshold pressure given by Hill (1950), and K is a function of the indicated variables which is known analytically for $\upsilon/c \ll 1$, and numerically for large values of υ/c.

Forrestal and Luk (1988) developed an analytical model for an elastic-plastic response of compressible materials from a uniform expansion of a spherical cavity with the constant expansion velocity, V. Here, they demonstrated the effect of compressibility on 6061-T6 aluminum. Their analysis was basically similar to that presented by Hunter and Crozier (1968); however, intensive work was done on numerical evaluations of the differential equations. Additionally, they found an approximation of the full nonlinear solution by eliminating the nonlinear terms in the differential equations. This approximation leads to the results as shown in Figure 2.12-2.13. The material properties of 6061-T6 aluminum are $Y = 300$ MPa, $Y/K = 0.00435$, $\rho_0 = 2{,}710$ kg/m^3, and $\nu = 1/3$ in which K is the bulk modulus and ρ_0 is the initial density of material. Figure 2.12 shows the elastic–plastic interface velocity, c, versus the expansion velocity. Figure 2.13 shows radial stress at the cavity wall versus expansion velocity.
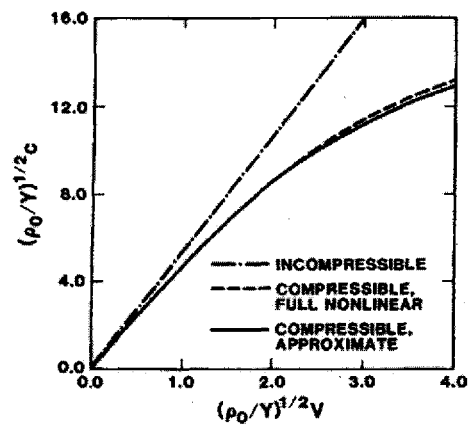
Figure 2.12 Elastic-plastic interface velocity versus cavity-expansion velocity for 6061-T6 aluminum.
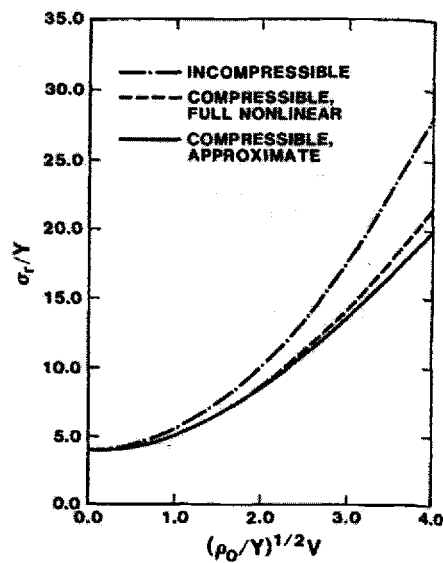
Figure 2.13 Radial stress on the cavity wall versus cavity expansion velocity for 6061-T6 aluminum.

Luk et al. (1991) extended their work (Forrestal and Luk, 1988) to include power-law strain hardening materials defined by the modified Ludwick equation

(Charkrabarty, 1987). The model considered the material as incompressible and compressible. For an incompressible material, they obtained a closed-form solution, where as the compressible results required the numerical solution of differential equations. Their objectives were to present the effects of compressibility on strain-hardening materials and to use the results for formulating the penetration equations of Forrestal et al. (1991), who modeled 6061-T651 targets as a strain hardening material.

The analysis used the same methods outlined in their previous work but with more complexity in the numerical evaluations of differential equations, since the strain-hardening term was introduced into the governing equations. Figure 2.14 shows show the predictions for the strain-hardening exponent, $n = 0$, 0.051, and 0.1 for the incompressible and compressible model of 6061-T651 aluminum.
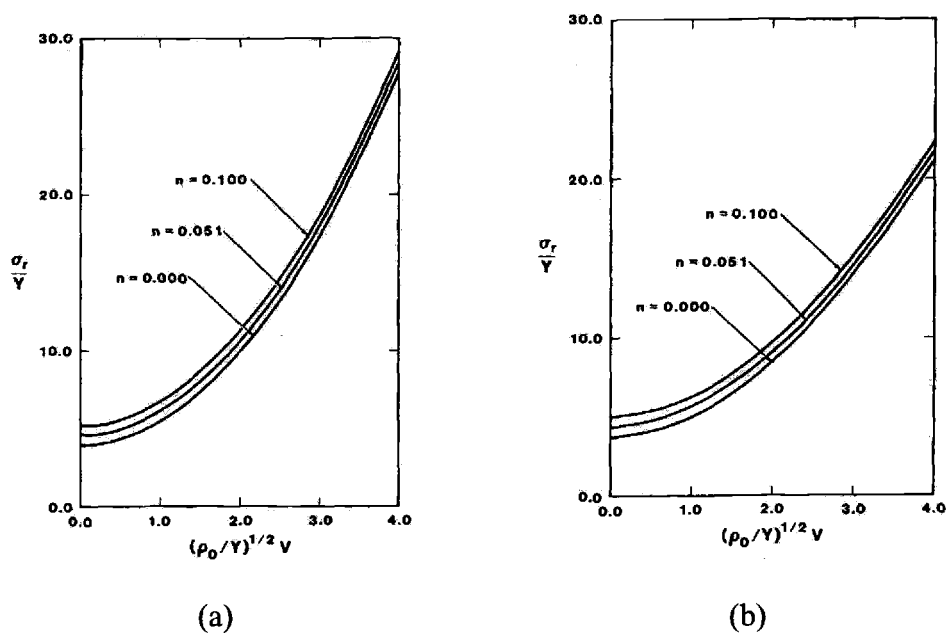
Figure 2.14 Radial stress on the cavity surface versus cavity expansion velocity for (a) an incompressible material and (b) a compressible material.

3. THEORY OF CAVITATION INSTABILITIES UNDER SPHERICALLY-SYMMETRIC LOADING

3.1 QUASI-STATIC ANALYSIS

This analysis follows the work outlined by Chadwick (1957). However, our analysis emphasizes cavitation instabilities in both a finite and infinite solid medium subjected to spherically-symmetric loading, which is gradually increased so that dynamic effects can be negligible. The material is assumed to be an isotropic and elastic-plastic solid.

3.1.1 Cavitation instabilities in a finite solid medium with elastic/perfectly-plastic materials

We begin by considering a spherical solid medium with internal radius, a, and external radius, b, subjected to uniform tension, σ_0, at $r = b$ as shown in Figure 3.1. To simplify our analysis, we assume that b is much larger than a and R throughout the deformation state so that the remote field remains elastic. The initial position of some arbitrary point inside the body is specified by the spherical polar coordinates (r_0, θ, and ϕ) with the origin at the center of the cavity. Since the system has a radial symmetry throughout the deformation, the position after loading is given by (r, θ, and ϕ).
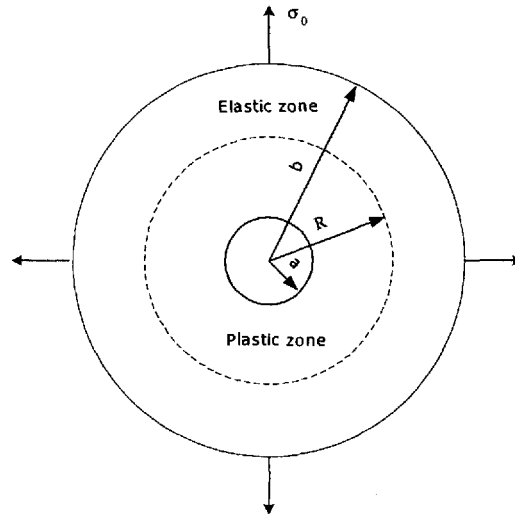
Figure 3.1 Spherical cavity in a finite solid medium under spherically-symmetric loading.

3.1.1.1 The elastic response

As σ_0 gradually increases from zero, the deformation is entirely elastic. As a result, the elastic response is governed by the equilibrium equation (neglecting the convective and acceleration term),

$$\frac{d^2u}{dr^2} + \frac{2}{r}\frac{du}{dr} - \frac{2}{r^2}u = 0, \tag{3.1}$$

and stress-strain relations satisfy

$$\sigma_r = \frac{E}{(1+v)(1-2v)}\left[(1-v)\frac{du}{dr} + 2v\frac{u}{r}\right],$$

$$\sigma_\theta = \sigma_\phi = \frac{E}{(1+v)(1-2v)}\left[v\frac{du}{dr} + \frac{u}{r}\right],$$

$$\varepsilon_r = \frac{du}{dr}, \tag{3.2}$$

$$\varepsilon_\theta = \varepsilon_\phi = \frac{u}{r},$$

where u is the radial displacement, E is Young's Modulus, and v is Poisson's ratio. The boundary conditions are

$$\sigma_r(a) = 0,$$
$$\sigma_r(b) = \sigma_o. \tag{3.3}$$

The solution of equation (3.1) and (3.2) subjected to the boundary conditions (3.3) is

$$\sigma_r = \sigma_0 \left\{ 1 - \left(\frac{a}{r}\right)^3 \right\} \bigg/ \left(1 - \frac{a^3}{b^3}\right), \tag{3.4}$$

$$\sigma_\theta = \sigma_0 \left\{ 1 + \frac{1}{2}\left(\frac{a}{r}\right)^3 \right\} \bigg/ \left(1 - \frac{a^3}{b^3}\right), \tag{3.5}$$

$$u = \frac{1}{E} \left\{ \frac{(1+v)a^3\sigma_0}{2}\frac{1}{r^2} + (1-2v)r \right\} \bigg/ \left(1 - \frac{a^3}{b^3}\right). \tag{3.6}$$

The equations (3.4)-(3.6) are valid until the onset of plastic yielding. At plastic yielding, the state of stress is given by the yield criterion of Tresca as

$$\sigma_\theta - \sigma_r = Y, \tag{3.7}$$

where Y is the yield stress. Since $\sigma_\theta - \sigma_r$ is greatest on the cavity wall, $r = a$, yielding begins there. The corresponding pressure can be obtained by substituting equations (3.4)-(3.5) into (3.7)

$$\sigma_{cr} = \frac{2Y}{3}\left(1 - \frac{a^3}{b^3}\right). \tag{3.8}$$

3.1.1.2 The plastic-elastic response

When $\sigma_o > \sigma_{cr}$, a plastic zone is formed around the cavity with outer radius R while the rest of medium remains elastic. The boundary conditions are given by

$$\sigma_r^E \big|_{r=b} = \sigma_0,$$
$$\sigma_r^P \big|_{r=a} = 0,$$

(3.9)

and the radial stresses must continue across the interface at $r = R$

$$\sigma_r^P \big|_{r=R} = \sigma_r^E \big|_{r=R},$$

(3.10)

where indices E and P represent the elastic and plastic zone respectively.

From equations (3.1)-(3.2), the stresses in the elastic zone, $R \le r \le b$, are

$$\sigma_r^E = -\frac{A}{r^3}\left(\frac{2E}{1+v}\right) + B\left(\frac{E}{1-2v}\right),$$
$$\sigma_\theta^E = \frac{A}{r^3}\left(\frac{E}{1+v}\right) + B\left(\frac{E}{1-2v}\right),$$

(3.11)

where A and B are parameters to be determined by the boundary conditions (3.9) and the yield criterion (3.7). A and B are found to be

$$A = \frac{(1+v)YR^3}{3E},$$
$$B = \frac{(1-2v)}{E}\left(\sigma_0 + \frac{2Y}{3}\frac{R^3}{b^3}\right).$$

(3.12)

The elastic stress-strain distribution is therefore

$$\sigma_r^E = -\frac{2Y}{3}\left[\frac{R^3}{r^3} - \frac{R^3}{b^3}\right] + \sigma_0,$$
$$\sigma_\theta^E = \frac{Y}{3}\left[\frac{R^3}{r^3} + \frac{2R^3}{b^3}\right] + \sigma_0,$$
$$\varepsilon_r^E = -\frac{2Y(1+v)}{3E}\frac{R^3}{r^3} + \frac{1-2v}{E}\left[\sigma_0 + \frac{2Y}{3}\frac{R^3}{b^3}\right],$$
$$\varepsilon_\theta^E = \frac{Y(1+v)}{3E}\frac{R^3}{r^3} + \frac{1-2v}{E}\left[\sigma_0 + \frac{2Y}{3}\frac{R^3}{b^3}\right].$$

(3.13)

The displacement is

$$u^E = \left[\frac{(1+v)Y}{3E}\frac{R^3}{r^3}\right]r + \frac{(1-2v)}{E}\left[\sigma_0 + \frac{2Y}{3}\frac{R^3}{b^3}\right]r.$$

(3.14)

The stresses in plastic zone, $a \le r \le R$, are governed by the equilibrium equation:

$$\frac{d\sigma_r}{dr} + 2\frac{\sigma_r - \sigma_\theta}{r} = 0. \tag{3.15}$$

By using the yield criterion in equation (3.7) and integrating with the boundary conditions (3.10), the stresses distribution is

$$\sigma_r^P = \sigma_0 - \frac{2Y}{3}\left[1 - \frac{R^3}{b^3}\right] + 2Y \ln\left(\frac{r}{R}\right),$$

$$\sigma_\theta^P = \sigma_0 + \frac{Y}{3}\left[1 + \frac{2R^3}{b^3}\right] + 2Y \ln\left(\frac{r}{R}\right). \tag{3.16}$$

and the relationship between a and R satisfies

$$\frac{R}{a} = e^{\frac{\sigma_0}{2Y} - \frac{1}{3}}, \tag{3.17}$$

where $b >> R$. By using the flow rule, the compressibility condition gives the relationship presented in equation (2.3). Then, equation (2.3) is integrated with the boundary condition (3.10), which results

$$\varepsilon_r + 2\varepsilon_\theta = \frac{1}{E}\left[(1 - 2v)\sigma_r + 2(1 - 2v)\sigma_\theta\right] - \frac{3}{E}(1 - 2v)\left[\frac{2Y}{3}\frac{R^3}{b^3} + \sigma_0\right]. \tag{3.18}$$

As σ_0 increases, the strain in the plastic zone becomes large especially near the cavity wall. In order to deal with the large strain in the plastic zone, the most favorable choice is the logarithmic strain:

$$\varepsilon_r = \ln\left(\frac{dr}{dr_0}\right) = \frac{du}{dr} + \frac{1}{2}\left(\frac{du}{dr}\right)^2 + \ldots,$$

$$\varepsilon_\theta = \ln\left(\frac{r}{r_0}\right) = \frac{u}{r} + \frac{1}{2}\left(\frac{u}{r}\right)^2 + \ldots. \tag{3.19}$$

Combining equations (3.16) and (3.19) with equation (3.18) yields

$$\ln\left[\frac{dr}{dr_0}\frac{r^2}{r_0^2}\right] = 3\beta \ln\frac{r}{R},$$

$$r^{2-3\beta}dr = \frac{1}{R^{3\beta}}r_0^2 dr, \tag{3.20}$$

where

$$\beta = \frac{2Y}{E}(1-2\nu).$$ (3.21)

According to a continuity requirement on the displacement at the interface, $r = R$, the solution of equation (3.20) must satisfy

$$\begin{aligned} R_0 &= R - u^E\big|_{r=R}, \\ &= R(1-\alpha), \end{aligned}$$ (3.22)

where

$$\alpha = \frac{Y}{3E}(1+\nu).$$ (3.23)

Integrating equation (3.20) with the upper limit in equation (3.22) and the lower limit at $r = a$ when $r_0 = a_0$, we obtain

$$\begin{aligned} &\int_a^R r^{2-3\beta}dr = \frac{1}{R^{3\beta}}\int_{a_0}^{R_0} r_0^2 dr_0, \\ &\exp[(1-\beta)(1-\tfrac{3\sigma_\infty}{2Y})] - 1 = (1-\beta)\left[\left(\tfrac{a_0}{a}\right)^3 \exp\left(1-\tfrac{3\sigma_\infty}{2Y}\right) - (1-\alpha)^3\right], \end{aligned}$$ (3.24)

or $\qquad a = a_0 \exp[-(\tfrac{\sigma_0}{2Y}-\tfrac{1}{3})]\left\{(1-\beta)^{-1}\left(\exp\left[-(1-\beta)\left(\tfrac{3\sigma_0}{2Y}-1\right)\right]-1\right)+(1-\alpha)^3\right\}^{-1/3}.$ (3.25)

If $a \gg a_0$ then $\dfrac{a_0}{a} \cong 0$ and $p \cong S_{cr}$ where S_{cr} is the cavitation limit stress.

Substituting into equation (3.24) results in

$$\frac{S_{cr}}{Y} = \frac{2}{3}\left[1 - \frac{1}{1-\beta}\ln\left\{1 - (1-\beta)(1-\alpha)^3\right\}\right].$$ (3.26)

Moreover, we found that the cavitation limit could be accurately determined by the slope between a and ε_θ. Let us consider

$$\lim_{\sigma_0 \to S_{cr}} \frac{da}{d\varepsilon_\theta^E\big|_{r=b}} \equiv \lim_{\sigma_0 \to S_{cr}} \frac{\frac{da}{d\sigma_0}}{\frac{d\varepsilon_\theta^E}{d\sigma_0}\big|_{r=b}}.$$ (3.27)

If a is large but less than an infinity, σ_0 is less than S_{cr}. As the result, we introduced a parameter, δ, into equation (3.26) as

$$S^* = \frac{2Y}{3}\left[1 + \frac{1}{1-\beta}\ln\left\{1 - (1-\beta)(1-\alpha)^3\right\} - \delta\right]. \tag{3.28}$$

Thus, equation (3.27) becomes

$$\lim_{\sigma_0 \to S_{cr}} \frac{da}{d\varepsilon_\theta^E\Big|_{r=b}} \equiv \lim_{\delta \to 0} \frac{\frac{da}{d\sigma_0}\Big|_{\sigma_0=S^*}}{\frac{d\varepsilon_\theta^E}{d\sigma_0}\Big|_{\substack{r=b \\ \sigma_0=S^*}}}. \tag{3.29}$$

We evaluated equation (3.29) using Mathematica program, which results

$$\lim_{\sigma_0 \to S_{cr}} \frac{da}{d\varepsilon_\theta^E\Big|_{r=b}} \cong \infty. \tag{3.30}$$

This equation implies that the cavitation limit occurs when the slope between a and ε_θ becomes infinite.

3.1.2 Cavitation instabilities in an infinite solid medium with elastic/perfectly-plastic materials

Consider an infinite solid medium containing an internal cavity with inner radius, a, subjected to uniform far-field tension, σ_∞, on the outer surface, $r = \infty$, as shown in Figure 3.2. The analysis proceeds using the same methods as those discussed in Section 3.1.1. It is obvious that these solutions can be obtained by directly replacing b and σ_0 in solutions of the previous section with infinity and σ_∞ respectively.

3.1.2.1 The elastic response

The elastic solutions are given as

$$\sigma_r = \sigma_\infty\left\{1 - \left(\frac{a}{r}\right)^3\right\}, \tag{3.31}$$

$$\sigma_\theta = \sigma_\infty \left\{ 1 + \frac{1}{2}\frac{a^3}{r^3} \right\},$$ (3.32)

$$u = \frac{(1+v)a^3\sigma_\infty}{2E}\frac{1}{r^2},$$ (3.33)

and the applied pressure at the onset of yielding is

$$\sigma_{cr} = \frac{2Y}{3}.$$ (3.34)
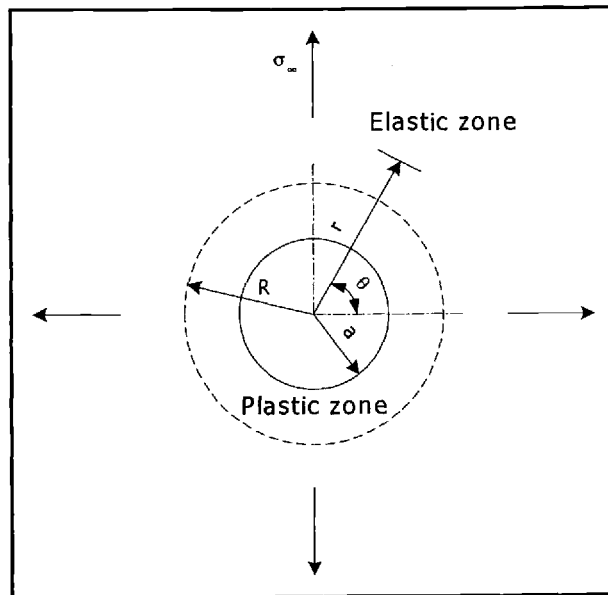
Figure 3.2 Spherical cavity in an infinite medium under remote spherically-symmetric loading.

3.1.2.2 The plastic-elastic response

In the elastic zone, $R \le r \le \infty$, the elastic solutions can be written as

$$\sigma_r^E = -\frac{2Y}{3}\frac{R^3}{r^3} + \sigma_\infty,$$

$$\sigma_\theta^E = \frac{Y}{3}\frac{R^3}{r^3} + \sigma_\infty,$$

$$\varepsilon_r^E = -\frac{2Y(1+v)}{3E}\frac{R^3}{r^3},$$

$$\varepsilon_\theta^E = \frac{Y(1+v)}{3E}\frac{R^3}{r^3},$$

$$u^E = \left[\frac{1+v}{3E}\left(\frac{R}{r}\right)^3\right]r.$$

(3.35)

In the plastic zone, $a \leq r \leq R$, the stress distribution is

$$\sigma_r^P = \sigma_\infty - \frac{2Y}{3} + 2Y \ln\left(\frac{r}{R}\right),$$

$$\sigma_\theta^P = \sigma_\infty + \frac{Y}{3} + 2Y \ln\left(\frac{r}{R}\right).$$

(3.36)

Additionally, the relationship between a and σ_∞ can be written as

$$a = a_0 \exp[-(\tfrac{\sigma_\infty}{2Y}-\tfrac{1}{3})]\left\{(1-\beta)^{-1}\left(\exp\left[-(1-\beta)\left(\tfrac{3\sigma_\infty}{2Y}-1\right)\right]-1\right)+(1-\alpha)^3\right\}^{-1/3}, \quad (3.37)$$

and the cavity limit stress, S_{cr}, is given by equation (3.26). Equations (3.14) and (3.37) are the same as those of Chadwick (1957). Figure 3.3 illustrates the plot of the cavity expansion a_0/a versus the load factor σ_∞/Y for the case of the perfectly plastic medium: $E = 10$ Mpsi, $Y = 40,000$ psi, and $v = 0.33$.

In order to compare equation (3.26) with those of Hilll (1950) and Huang et al. (1991) for the case of cavitation instabilities in an elastic-plastic medium, substituting equations (3.21) and (3.23) into (3.26) results in

$$\frac{S}{Y} = \frac{2}{3}\left[1 + \frac{1}{1-2\varepsilon_y(1-2v)}\ln\left\{1-(1-2\varepsilon_y(1-2v))\left(1-\frac{\varepsilon_y}{3}(1-v)\right)^3\right\}^{-1}\right]. \quad (3.38)$$

Values of $1-2\varepsilon_y(1-2v)$ for various combinations of v and ε_y are displayed in Table 3.1. It is seen that

$$1-2\varepsilon_y(1-2v) \cong 1, \tag{3.39}$$

when $\varepsilon_y < 10^{-2}$. Therefore, substituting equation (3.39) and

$$\left(1 - \frac{\varepsilon_y}{3}(1-v)\right)^3 = 1 - \varepsilon_y(1-v) + O(\varepsilon_y^2),$$ (3.40)

into equation (3.38) and rearranging lead to

$$\frac{S_{cr}}{Y} = \frac{2}{3}\left[1 + \ln\left\{1 - \left(1 - 2\varepsilon_y(1-2v)\right)\left(1 - \varepsilon_y(1-v)\right)\right\}^{-1}\right] + O(\varepsilon_y^2),$$

$$= \frac{2}{3}\left[1 + \ln\left\{\frac{1}{3(1-v)\varepsilon_y}\right\}\right] + O(\varepsilon_y^2).$$ (3.41)

Equation (3.35) is the same as those of Hill (1950) and Huang et al. (1991).
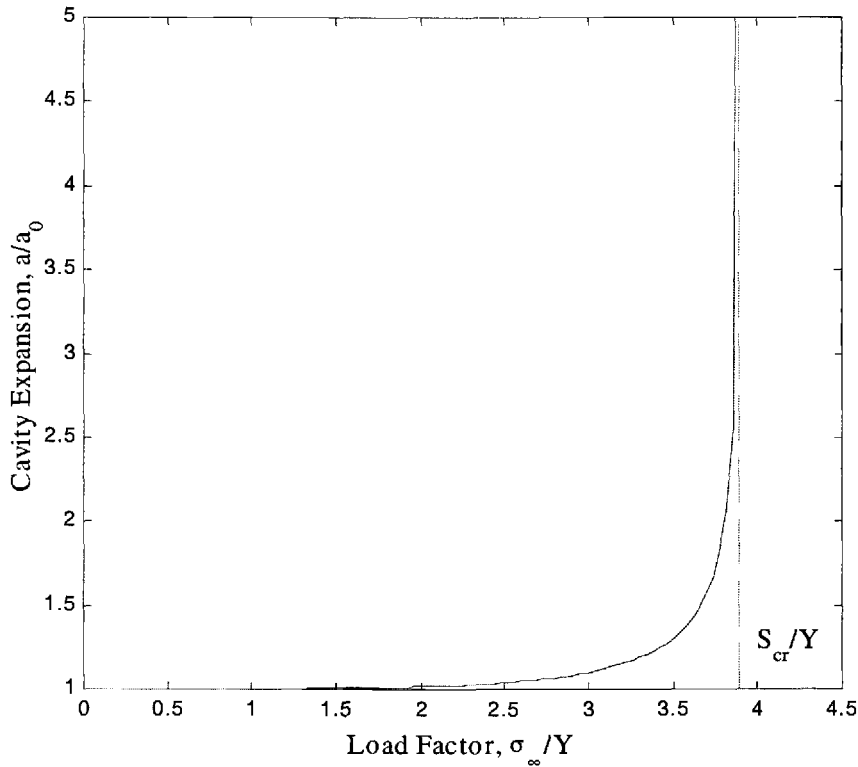
Figure 3.3 Cavity expansion vs. load factor in elastic/perfectly-plastic material: $E = 10$ Mpsi, $\varepsilon_y = 0.004$, and $v = 0.33$.

Table 3.1 The variation of $1 - 2\varepsilon_y \left(1 - 2v\right)$ with v and ε_y

ε_y \ v	0.2	0.3	0.4
10^{-2}	0.98800	0.99200	0.99600
10^{-3}	0.99880	0.99920	0.99960
10^{-4}	0.99988	0.99992	0.99996

3.1.3 Cavitation instabilities in an infinite solid medium with strain-hardening, elastic-plastic, materials

The analysis of cavitation instabilities with strain-hardening materials is derived using the same methods as those described in Section 3.1.2. In order to include the strain-hardening effects into the governing equation, the yield condition is given in the form of

$$\sigma_\theta - \sigma_r = Y + H\left(\int d\hat{\varepsilon}^p\right),$$
$$\sigma_\theta = \sigma_\varphi,$$

(3.42)

where H is the work-hardening function and $d\hat{\varepsilon}^p$ is the increment of equivalent plastic strain. The boundary conditions are

$$\sigma_r \big|_{r=a} = 0,$$
$$\sigma_r^p \big|_{r=R} = \sigma_r^E \big|_{r=R} = -\frac{2Y}{3} + \sigma_\infty,$$

(3.43)

where $\sigma_r^E \big|_{r=R}$ is given by equation (3.35).

For the plastic-elastic response, the radial stress is obtained by integrating the equilibrium equation (3.15) with the boundary conditions (3.43):

$$\sigma_\infty = \frac{2Y}{3}\left[1 + 3\ln\left(\frac{R}{a}\right)\right] + 2\int_a^R H\left(\int d\hat{\varepsilon}^p\right)\frac{dr}{r}.$$

(3.44)

To simplify our analysis, we assumed that the medium is incompressible. Then the equation of mass conservation can be expressed as

$$r^3 - r_0^3 = a^3 - a_0^3 = R^3 - R_0^3. \tag{3.45}$$

Manipulating the last equality in equations (3.45) and making use of the displacement relation in equation (3.35) yields

$$R^3 - R_0^3 = \gamma R^3, \tag{3.46}$$

where

$$\gamma = 1 - (1 - \phi)^3, \\ \phi = Y/2E. \tag{3.47}$$

Next, equating the middle equality in equations (3.45) with (3.46) yields

$$\frac{R}{a} = \left(\frac{\delta}{\gamma}\right)^{1/3}, \tag{3.48}$$

where

$$\delta = 1 - a_0^3 / a^3. \tag{3.49}$$

By combining the Prandlt-Reuss relations,

$$d\hat{\varepsilon}^p = -d\varepsilon_r^p = 2d\varepsilon_\theta^p, \tag{3.50}$$

with the assumption that the plastic strain components are much larger than the corresponding elastic strain, we obtain

$$\int d\hat{\varepsilon}^p = 2\varepsilon_\theta = 2\ln(r/r_0). \tag{3.51}$$

Substituting equations (3.48) and (3.51) into (3.44) results

$$\sigma_\infty = \tfrac{2Y}{3}\left[1 + \ln\delta - \ln\gamma\right] + 2\int_\delta^\gamma H\left(\tfrac{2}{3}\ln\tfrac{1}{1-\psi}\right)\tfrac{d\psi}{\psi}, \tag{3.52}$$

where

$$\psi = 1 - r_0^3/r^3. \tag{3.53}$$

It is found that

$$\frac{d\delta}{d\sigma_\infty} = \frac{3\delta}{2}\left[Y + H\left(2\ln\frac{a}{a_0}\right)\right]^{-1} > 0. \tag{3.54}$$

This equation implies that a/a₀ increases monotonically with σ_∞. Thus, if σ_∞ is equal to a finite value, S_{cr}, when $\delta = 1$, we have a cavitation instability similar to the one shown in Figure 3.3. By changing the integration variable of the second term in equation (3.52), we obtain the expression for the cavitation limit stress, S_{cr}, as

$$S_{cr} = \tfrac{2}{3} Y [1 - \ln \gamma] + \int_{-\frac{2}{3}\ln(1-\phi)}^{\infty} \frac{H(\eta)}{\exp(\frac{3}{2}\eta) - 1} d\eta. \qquad (3.55)$$

The integral on the right appears to converge for varieties of functions, H. Chadwick (1957) demonstrated that a function of H could be accurately represented by a polynomial expression given in equation (2.14). Finally, he evaluated the corresponding form of equation (3.55), which results in

$$S_{cr} = \frac{2}{3} Y [1 - \ln \gamma] + \sum_{n=1}^{N} \left(\frac{2}{3}\right)^{n+1} n! \zeta(n+1), \qquad (3.56)$$

where ζ is the Reimann zeta function. In the case of linear work-hardening, $N = 1$ and $\zeta(2) = \dfrac{\pi^2}{6}$,

$$S_{cr} = \frac{2}{3} Y [1 - \ln(\gamma)] + \frac{2}{27} \pi^2 H_1, \qquad (3.57)$$

where H_1 is the linear work-hardening constant.

Let consider a stress-strain curve for the linear strain-hardening material illustrated in Figure 3.4. It is found that the stress-strain relation is

$$\sigma = Y + \left(\frac{m}{1-m} E\right) \varepsilon^p, \qquad (3.58)$$

where m is the linear strain-hardening constant. Comparing equations (3.42) with (3.58), it is found that

$$H_1 = \frac{m}{1-m} E. \qquad (3.59)$$
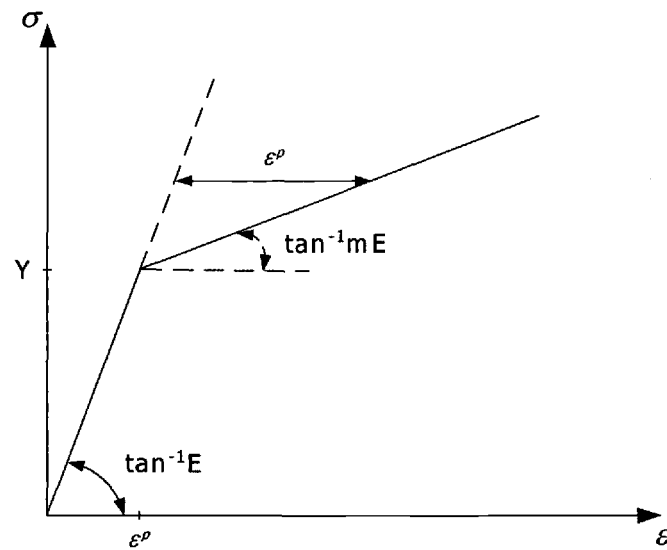
Figure 3.4 Stress-strain curve for linear hardening elastic-plastic materials.

3.2 DYNAMIC ANALYSIS

This analysis follows the work presented by Hopkins (1960) on the analysis of dynamic expansion of an internal pressurized spherical cavity in incompressible medium. However, in this analysis a remote tension is applied. Furthermore, we included the strain-rate hardening effects into our analysis. As mentioned by many authors, the rate of cavity expansion is relatively high during the first expansion phase in which it will directly affect to material properties. This phenomenon is observed in rate-dependent materials such as metals. We will study effects of inertia and strain-rate hardening on dynamic responses of the medium independently.

3.2.1 Cavitation instabilities in an infinite solid medium with combined strain-rate hardening and inertia effects

We begin by considering an infinite solid medium containing an internal cavity with inner radius, a, subjected to uniform far-field pressure, σ_∞, on an outer surface, $r = \infty$, as shown in Figure 3.2. In order to deal with large deflections, we use strain-rates in the forms of

$$\dot{\varepsilon}_r = \partial \varepsilon_r / \partial t = \partial v / \partial r,$$
$$\dot{\varepsilon}_\theta = \dot{\varepsilon}_\phi = v / r,$$

(3.60)

where v is a velocity field depending on the radial distance measured from the center of cavity, r, and time, t. To simply our analysis we assume that (1) σ_∞ is suddenly applied at $t = 0$ and remains constant for all time and (2) the medium is incompressible. The incompressibility requires that

$$\dot{\varepsilon}_r + \dot{\varepsilon}_\theta + \dot{\varepsilon}_\phi = 0.$$

(3.61)

Substituting equations (3.60) into (3.61) gives

$$\frac{\partial}{\partial r}\left(r^2 v\right) = 0,$$

(3.62)

so that the particle velocity can be written in term of the velocity of cavity expansion as given in equation (2.44) by Hopkins (1960). Thus, the strain-rates can be written as

$$\dot{\varepsilon}_r = -2a^2 \dot{a} / r^3,$$
$$\dot{\varepsilon}_\theta = a^2 \dot{a} / r^3,$$

(3.63)

and the equation of motion is

$$\frac{\partial \sigma_r}{\partial r} + \frac{2}{r}(\sigma_r - \sigma_\theta) = \rho\left(\frac{\partial v}{\partial t} + v\frac{\partial v}{\partial r}\right),$$
$$= \rho\left[\frac{1}{r^2}\left(a^2 \ddot{a} + 2a\dot{a}^2\right) - 2a^4 \frac{\dot{a}^2}{r^5}\right],$$

(3.64)

where ρ is the density of material and a is the current cavity radius.

To describe the post-yield behavior of yield stress on strain-rate hardening materials, we use the yield stress equation (Perzyna, 1966):

$$Y = Y_0\left[1 + C\dot{\bar{\varepsilon}}_p^m\right],$$

(3.65)

where Y and Y_0 are the yield stresses in the initial and current states respectively; $\dot{\bar{\varepsilon}}_p$ is the equivalent plastic strain-rate; m and C are constants. To simplify our analysis further, we assume that the elastic strain rate components are much smaller than the plastic strain rate components; therefore, $\dot{\bar{\varepsilon}}_p \cong \dot{\bar{\varepsilon}}$. For radial symmetry, the equivalent plastic strain rate can be written as

$$\dot{\bar{\varepsilon}}_p = \frac{\sqrt{2}}{3}\left[\left(\dot{\varepsilon}_r - \dot{\varepsilon}_\theta\right)^2 + \left(\dot{\varepsilon}_r - \dot{\varepsilon}_\phi\right)^2 + \left(\dot{\varepsilon}_\theta - \dot{\varepsilon}_\phi\right)^2\right]^{1/2},$$

$$= \frac{2}{3}\left(\dot{\varepsilon}_\theta - \dot{\varepsilon}_r\right),$$

(3.66)

$$= \frac{2a^2\dot{a}}{r^3}.$$

Thus, the expression of the yield stress for linear strain-rate hardening ($m = 1$) is

$$Y = Y_0\left[1 + C\frac{2a^2\dot{a}}{r^3}\right].$$

(3.67)

3.2.1.1 The elastic response

The initial response is purely elastic throughout the medium such that small strain components are expected. The boundary conditions are

$$\sigma_r\big|_{r=a} = 0,$$

$$\sigma_r\big|_{r=\infty} = \sigma_\infty.$$

(3.68)

By integrating the particle velocity equation (2.44), and substituting it into the expression for the hoop strain, we arrive at

$$\varepsilon_\theta = \frac{u}{r} = \frac{a^3 - a_0^3}{3r^3},$$

(3.69)

where a_0 is the initial cavity radius at $t = 0$. In case of the radial symmetry, the hoop strain is given by Hooke's law as

$$\varepsilon_\theta = \frac{1}{2E}(\sigma_\theta - \sigma_r),$$

(3.70)

and together with equation (3.69), we obtain

$$\sigma_r - \sigma_\theta = -2E\frac{a^3 - a_0^3}{3r^3}.$$

(3.71)

Substituting equations (3.71) into (3.64) and then integrating with boundary conditions (3.68), obtain

$$\sigma_\infty - \tfrac{4}{9}E\left(1 - \tfrac{a_0^3}{a^3}\right) = \rho\left[a\ddot{a} + \tfrac{3}{2}\dot{a}^2\right].$$

(3.72)

Let us define the displacement of cavity surface, δ, as

$$\delta = a - a_0.$$

(3.73)

It follows from equation (3.72) and the assumption of small δ and $\dot{\delta}$ that the governing equation becomes

$$\ddot{\delta} + \frac{4}{3}\frac{E}{\rho a_0^2}\delta = \frac{\sigma_\infty}{\rho a_0}.$$

(3.74)

This is a linear ordinary differential equation subjected to the initial conditions, $\delta = \dot{\delta} = 0$ at $t = 0$. Integrating equation (3.74) yields

$$\delta = \frac{3}{4}\frac{\sigma_\infty a_0}{E}\left[1 - \cos\sqrt{\frac{4E}{3\rho a_0^2}}t\right].$$

(3.75)

This equation is valid until the onset of yielding on the cavity wall. At yielding, the state of stress is given by substituting equations (3.67) into the yield condition (3.7):

$$\sigma_\theta - \sigma_r = Y_0\left[1 + C\frac{2a^2\dot{a}}{r^3}\right].$$

(3.76)

Equating equations (3.71) with (3.76) and evaluating at $r = a$ results

$$Y_0\left[1 + C\frac{2\dot{a}}{a}\right] = 2E\frac{a^3 - a_0^3}{3a^3}.$$

(3.77)

This equation is used to determine the initial conditions for the plastic response where the expressions for a and $\dot{a}$ are given by equations (3.73) and (3.75).

3.2.1.2 The plastic response

After the onset of yielding on the cavity surface, the yielding spreads outward from the cavity. The boundary conditions are

$$\sigma_r\big|_{r=a} = 0,$$
$$\sigma_r\big|_{r=\infty} = \sigma_\infty,$$

(3.78)

and radial stresses must be continuous across the interface

$$\sigma_r^P\big|_{r=R} = \sigma_r^E\big|_{r=R}.$$

(3.79)

In the plastic zone, $a < r < R$, the radial stress, σ_r^P, is given by substituting the yield condition (3.76) into equation (3.64) and integrating with the boundary condition (3.78):

$$\sigma_r^P = 2Y_0\left[\ln\left(\frac{r}{a}\right) - \frac{2}{3}Ca^2\dot{a}\left\{\frac{1}{r^3} - \frac{1}{a^3}\right\}\right]$$
$$- \rho\left[\frac{1}{r}\left(a^2\ddot{a} + 2a\dot{a}^2\right) - \frac{a^4\dot{a}^2}{2r^4} - a\ddot{a} - \frac{3}{2}\dot{a}^2\right].$$

(3.80)

In the elastic zone, $R < r < \infty$, it follows from equation (3.64) that

$$\sigma_r^E = \sigma_\infty - \frac{4}{9}E\frac{\left(a^3 - a_0^3\right)}{r^3} - \rho\left[\frac{1}{r}\left(a^2\ddot{a} + 2a\dot{a}^2\right) - \frac{a^4\dot{a}^2}{2r^4}\right].$$

(3.81)

The relationship between a and R is obtain by equating equations (3.71) with (3.76) and then evaluating at $r = R$:

$$R^3 = \frac{2}{3Y_0}\left[E\left(a^3 - a_0^3\right) - 3Y_0Ca^2\dot{a}\right].$$

(3.82)

By applying the boundary condition (3.79) and making use of equation (3.82), we arrive at the differential equation of the cavity radius,

$$\ddot{a} = \frac{1}{\rho a}\left[\sigma_\infty - \frac{2Y_0}{3}\frac{E\left(1-\frac{a_0^3}{a^3}\right)}{\left(E\left\{1-\frac{a_0^3}{a^3}\right\}-3Y_0 C\frac{\dot{a}}{a}\right)}\right.$$

$$-\frac{2Y_0}{3}\ln\left[\frac{2}{3Y_0}\left(E\left\{1-\frac{a_0^3}{a^3}\right\}-3Y_0 C\frac{\dot{a}}{a}\right)\right] \tag{3.83}$$

$$\left.+\frac{4Y_0 C}{3}\frac{\dot{a}}{a}\left(\frac{3}{2}\frac{Y_0}{E\left\{1-\frac{a_0^3}{a^3}\right\}-3Y_0 C\frac{\dot{a}}{a}}-1\right)-\frac{3}{2}\rho\dot{a}^2\right],$$

which is subjected the initial condition obtained from equation (3.77).

For the quasi-static case where $\dot{a} = \ddot{a} = 0$, it follows from equation (3.83) that

$$\sigma_\infty = \frac{2Y}{3}\left[1+\ln\left(\frac{2E}{3Y_0}\left\{1-\frac{a_0^3}{a^3}\right\}\right)\right], \tag{3.84}$$

and letting $a \to \infty$ at $\sigma_\infty = S_{cr}$, it results in

$$S_{cr} = \frac{2Y}{3}\left[1+\ln\left(\frac{2E}{3Y_0}\right)\right]. \tag{3.85}$$

This equation has the same result as Huang et al. (1991).

For the dynamic case we assume that σ_∞ is different from S_{cr} by an amount Δ:

$$\sigma_\infty = \frac{2Y}{3}\left[1+\ln\left(\frac{2E}{3Y_0}\right)\right]+\Delta. \tag{3.86}$$

Next, substituting equation (3.86) into (3.83) yields

$$\ddot{a} = \frac{1}{\rho a}\left[\frac{2Y_0}{3}\left[1+\ln\left(\frac{2E}{3Y_0}\right)\right] + \Delta - \frac{2Y_0}{3}\frac{E\left(1-\frac{a_0^3}{a^3}\right)}{\left(E\left\{1-\frac{a_0^3}{a^3}\right\}-3Y_0C\frac{\dot{a}}{a}\right)}\right.$$

$$-\frac{2Y_0}{3}\ln\left[\frac{2}{3Y_0}\left(E\left\{1-\frac{a_0^3}{a^3}\right\}-3Y_0C\frac{\dot{a}}{a}\right)\right] \qquad (3.87)$$

$$\left. +\frac{4Y_0C}{3}\frac{\dot{a}}{a}\left(\frac{3}{2}\frac{Y_0}{E\left\{1-\frac{a_0^3}{a^3}\right\}-3Y_0C\frac{\dot{a}}{a}}-1\right) - \frac{3}{2}\rho\dot{a}^2\right].$$

If the cavitation instabilities does not exist, the maximum value of cavity radius, a_{max}, will be finite and at this point $\dot{a} = 0$ and $\ddot{a} < 0$. Then, substituting these values into equation (3.87) results in

$$\frac{1}{\rho a_{max}}\left[\Delta - \frac{2Y_0}{3}\ln\left(1-\frac{a_0^3}{a_{max}^3}\right)\right] < 0. \qquad (3.88)$$

Since $0 < a_0^3/a_{max}^3 < 1$, $\Delta < 0$. Therefore, σ_∞ must be below the static cavitation stress to avoid a cavitation instability in the dynamic case.

These nonlinear differential equation (3.83) was solved by using ODE 45 code, in the Matlab program. The numerical scheme is based on an explicit Runge-Kutta 45 formula, the Dormand-Prince pair. The tolerances were set at 10^{-8} for both real and absolute tolerance. Figure 3.5 illustrates the yield stress versus the strain rate for incompressible and elastic/perfectly-plastic material with various linear strain-rate hardening effects: $E = 10$ Mpsi, $\varepsilon_y = 0.004$, $v = 0.5$, $\rho = 0.000259$ lb-sec^2/in^4, and $0 \leq C \leq 0.1$ sec. Figure 3.6 illustrates the numerical solution at an applied load of 163.094 Ksi slightly above the cavitation limit stress ($S_{cr} = 163.093$ Ksi) for (a) Cavity expansion versus time and (b) Velocity of cavity expansion versus time. As expected, the cavity growth rate is lower when the strain-rate hardening increases.
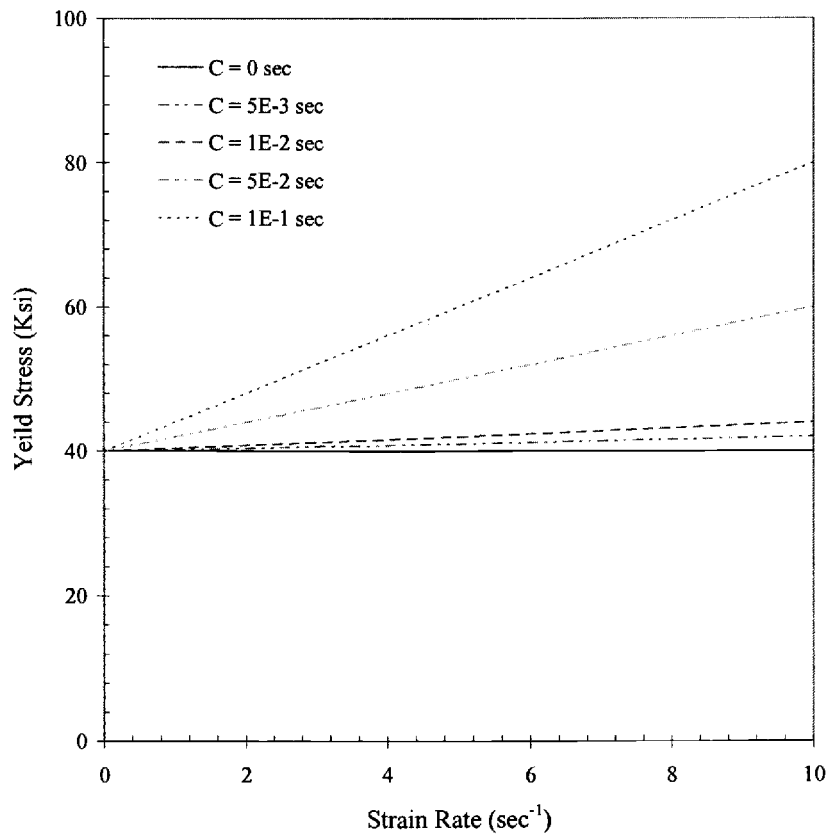
Figure 3.5 Yield stress vs. strain rate for incompressible and elastic/perfectly-plastic material with various linear strain-rate hardening effects: $E = 10$ Mpsi, $\varepsilon_y = 0.004$, $\nu = 0.5$, $\rho = 0.000259$ lb-sec^2/in^4, and $0 \leq C \leq 0.1$ sec.

(a)
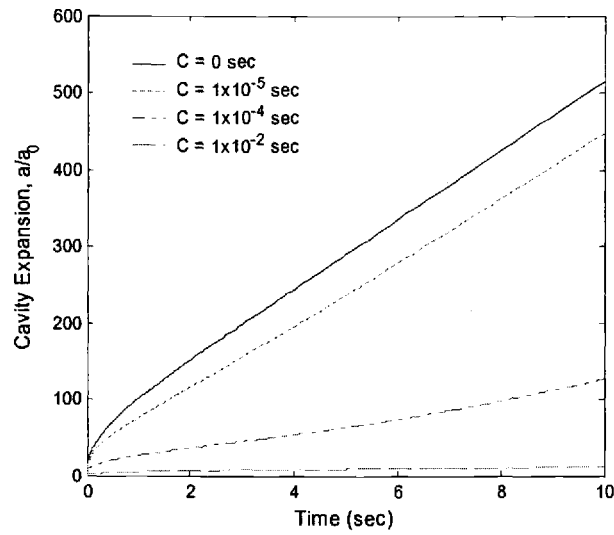
(b)
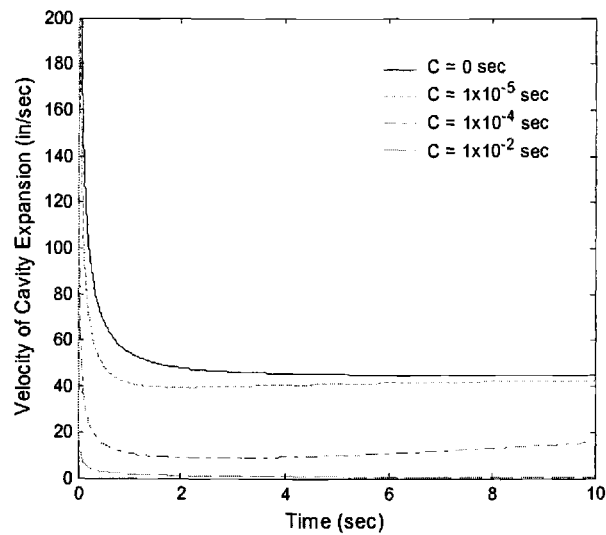
Figure 3.6 Numerical solutions of dynamic responses (with combined strain-rate hardening and inertia effects) under spherically-symmetric loading for various linear strain-rate hardening coefficients, $0 \leq C \leq 0.01$ sec. (a) Cavity expansion vs. time; (b) Velocity of cavity expansion vs. time. The step loading is suddenly applied for magnitude of 163.094 Ksi (slightly above the cavitation limit stress, S_{cr} = 163.093 Ksi) and remains constant for all time.

3.2.2 Cavitation instabilities in an infinite solid medium with only strain-rate hardening effects

The solution for this problem is obviously obtained from ones in Section 3.2.1 by replacing ρ with zero. For the elastic response, it follows from equilibrium equation (3.64) that there is not enough information to construct the differential equation for a cavity radius. For plastic-elastic response, the governing equation is obtained from equation (3.87) as

$$
\sigma_\infty - \frac{2Y_0}{3} \frac{E\left(1 - \frac{a_0^3}{a^3}\right)}{\left(E\left\{1 - \frac{a_0^3}{a^3}\right\} - 3Y_0 C \frac{\dot{a}}{a}\right)}
$$
$$
- \frac{2Y_0}{3} \ln\left[\frac{2}{3Y_0}\left(E\left\{1 - \frac{a_0^3}{a^3}\right\} - 3Y_0 C \frac{\dot{a}}{a}\right)\right]
$$
$$
+ \frac{4Y_0 C}{3} \frac{\dot{a}}{a}\left(\frac{3}{2} \frac{Y_0}{E\left\{1 - \frac{a_0^3}{a^3}\right\} - 3Y_0 C \frac{\dot{a}}{a}} - 1\right) = 0. \tag{3.89}
$$

There are no initial conditions given for this equation; however, they can be determined in an approximate way. First, we have to determine a minimum value of a at which equation (3.89) is still valid. Then, we solve for the corresponding value of $\dot{a}$. Finally, we assume that a and $\dot{a}$ are responses at $t = 0$. This approximation is quite accurate since, by without inertia mass, the time at initial yielding is apparently very close to zero. This nonlinear equation is solved numerically by using the Secant method (Hoffman, 1992) in the Matlab program. The material is assumed to be incompressible and elastic/perfectly-plastic solids with various linear strain-rate hardening effects: $E = 10$ Mpsi, $\varepsilon_y = 0.004$, $v = 0.5$, $\rho = 0.000259$ lb-sec^2/in^4, and $C = 0.1, 0.05,$ and 0.01 sec. Figure 3.7 illustrates the numerical solution at an applied load of 163.094 Ksi slightly above the cavitation limit stress ($S_{cr} = 163.093$ Ksi) for (a) Cavity expansion versus time and (b) Velocity of cavity expansion versus time. Again, the cavity growth rate is lower when the strain-rate hardening increases.

(a)

(b)
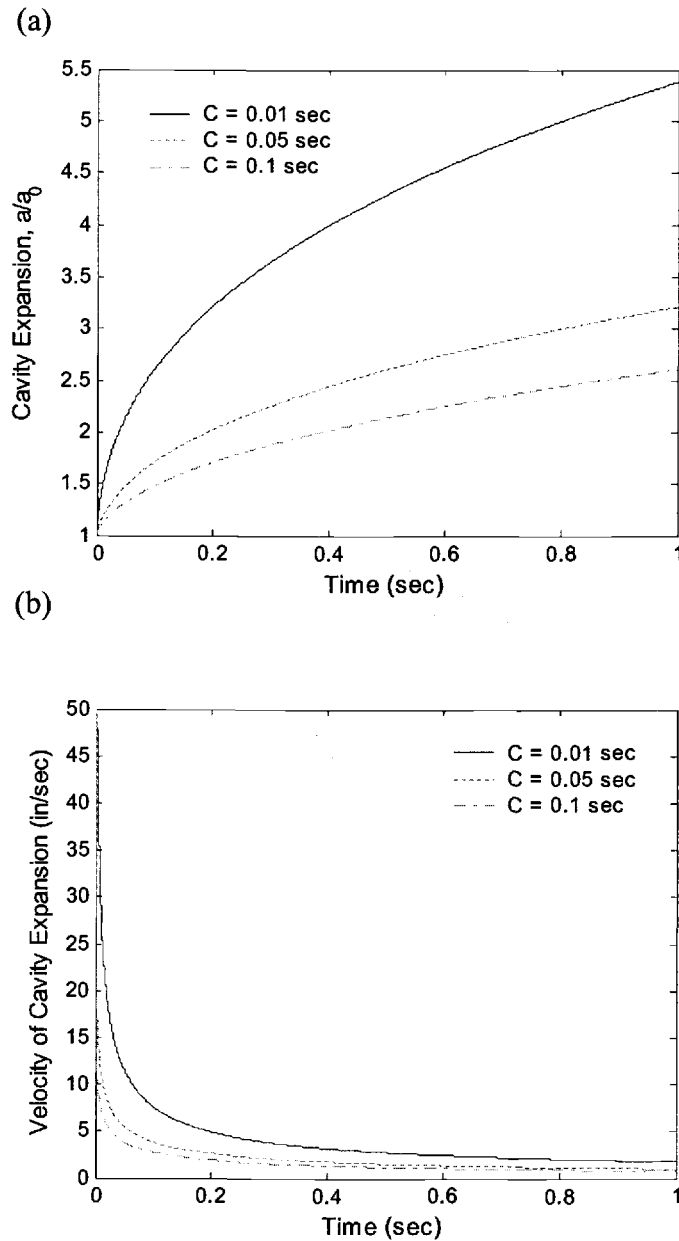
Figure 3.7 Numerical solution of dynamic responses (with only strain-rate hardening effects) under spherically-symmetric loading for various linear strain-rate hardening coefficients, $0.01 \leq C \leq 0.1$ sec. (a) Cavity expansion vs. time; (b) Velocity of cavity expansion vs. time. The step loading is suddenly applied for magnitude of 163.094 Ksi (slightly above the cavitation limit stress, $S_{cr} = 163.093$ Ksi) and remains constant for all the time.

3.2.3 Cavitation instabilities in an infinite solid medium with only inertia effects

The solution for this problem is apparently obtained from ones in Section 3.2.1 by replacing C with zero. Therefore, for the elastic response the governing differential equation is the same as equation (3.74). At the onset of yielding on the cavity wall, the yield condition is obtained from equation (3.77) as

$$Y = 2E\varepsilon_\theta\big|_{r=a} = 2E\frac{\delta_1}{a_0}, \tag{3.90}$$

where δ_I is cavity displacement when $t = t_I$ at the initial yielding. Substituting equations (3.75) into (3.90), results in

$$t_1 = \sqrt{\frac{3\rho a_0^2}{4E}}\cos^{-1}\left(1 - \frac{2Y}{3\sigma_\infty}\right), \tag{3.91}$$

and corresponding a_I and $\dot{a}_1$ are

$$a_1 = \left(1 + \frac{Y}{2E}\right)a_0,$$

$$\dot{a}_1 = \sqrt{\frac{\sigma_\infty Y}{E\rho}\left(1 - \frac{Y}{3\sigma_\infty}\right)}. \tag{3.92}$$

These are the initial conditions for a governing equation in the plastic-elastic response.

In the plastic-elastic response, the differential equation of the cavity radius is

$$\ddot{a} = \frac{1}{\rho a}\left[\sigma_\infty - \frac{2Y_0}{3}\left(1 + \ln\left(\frac{2E}{3Y}\left\{1 - \frac{a_0^3}{a^3}\right\}\right)\right) - \frac{3}{2}\rho\dot{a}^2\right]. \tag{3.93}$$

Furthermore, the velocity of cavity expansion at steady state response can explicitly solved from equation (3.93) by letting $\ddot{a} = 0$ at $a \to \infty$:

$$\dot{a} = \sqrt{\frac{2}{3\rho}(\sigma_\infty - S_{cr})}, \tag{3.94}$$

where S_{cr} is the cavitation limit stress given by the quasi-static analysis.

The nonlinear differential equation is solved by using ODE 45 code in the Matlab program with both real and absolute tolerance set at 10^{-8}. The material is assumed to be incompressible and elastic/perfectly-plastic solid: $E = 10$ Mpsi, $\varepsilon_y =$ 0.004, $v = 0.5$, and $\rho = 0.000259$ lb-sec^2/in^4. Figure3.8-3.10 illustrates the cavity growth for various far field loadings. Figure 3.8 demonstrates the return motion of the cavity following the first expansion phase when the applied load is 158 Kpsi below the cavitation limit stress ($S_{cr} = 163.093$ Ksi) as described by Hoskin (1960). Figure 3.9 demonstrates the responses when the applied load is equal to the cavitation limit stress. Figure 3.10 demonstrates a cavitation instability when the applied load is slightly greater than the cavitation limit stress.

(a)

(b)
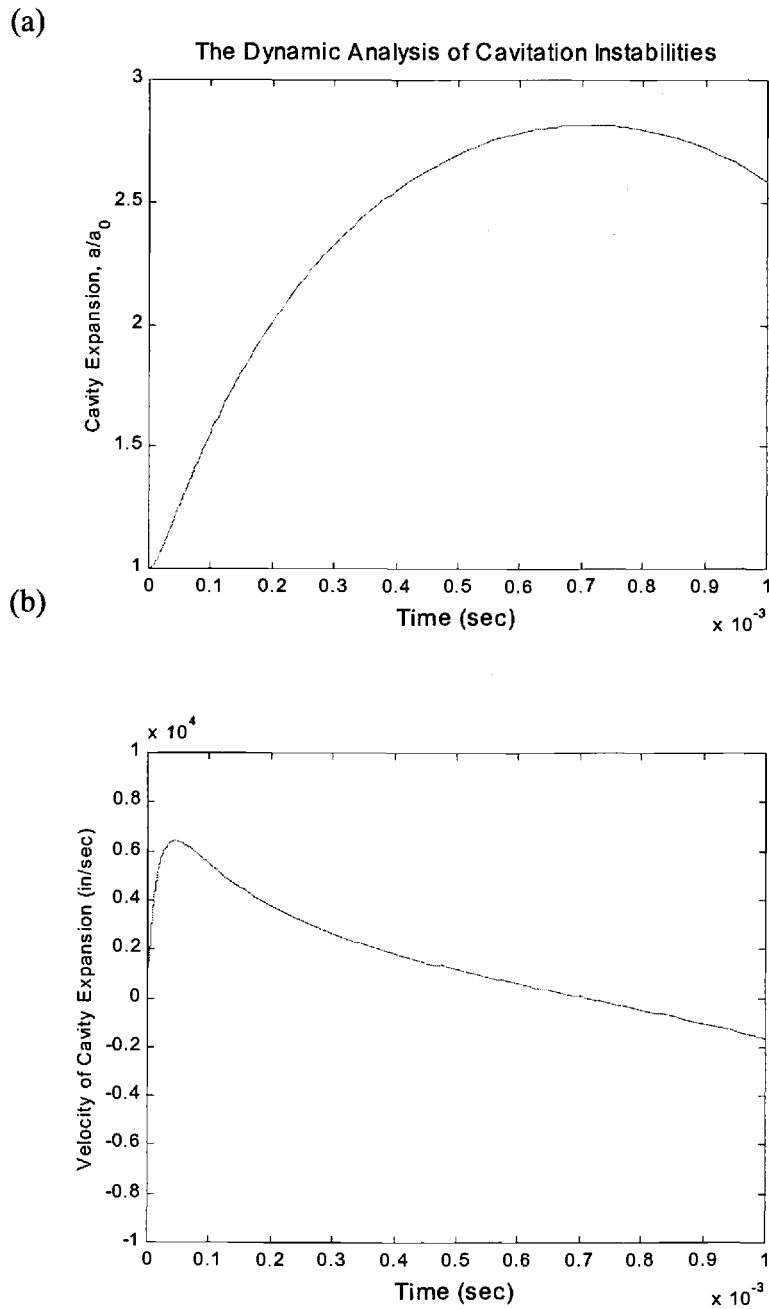
Figure 3.8 Numerical solution (with only inertia effects) under spherically-symmetric loading at $\sigma_\infty = 158$ Ksi (below the cavitation limit stress, $S_{cr} = 163.093$ Ksi) for (a) cavity expansion vs. time and (b) velocity of cavity expansion vs. time. The step loading is suddenly applied for magnitude of 158 Ksi and remains constant for all time.

(a)

(b)
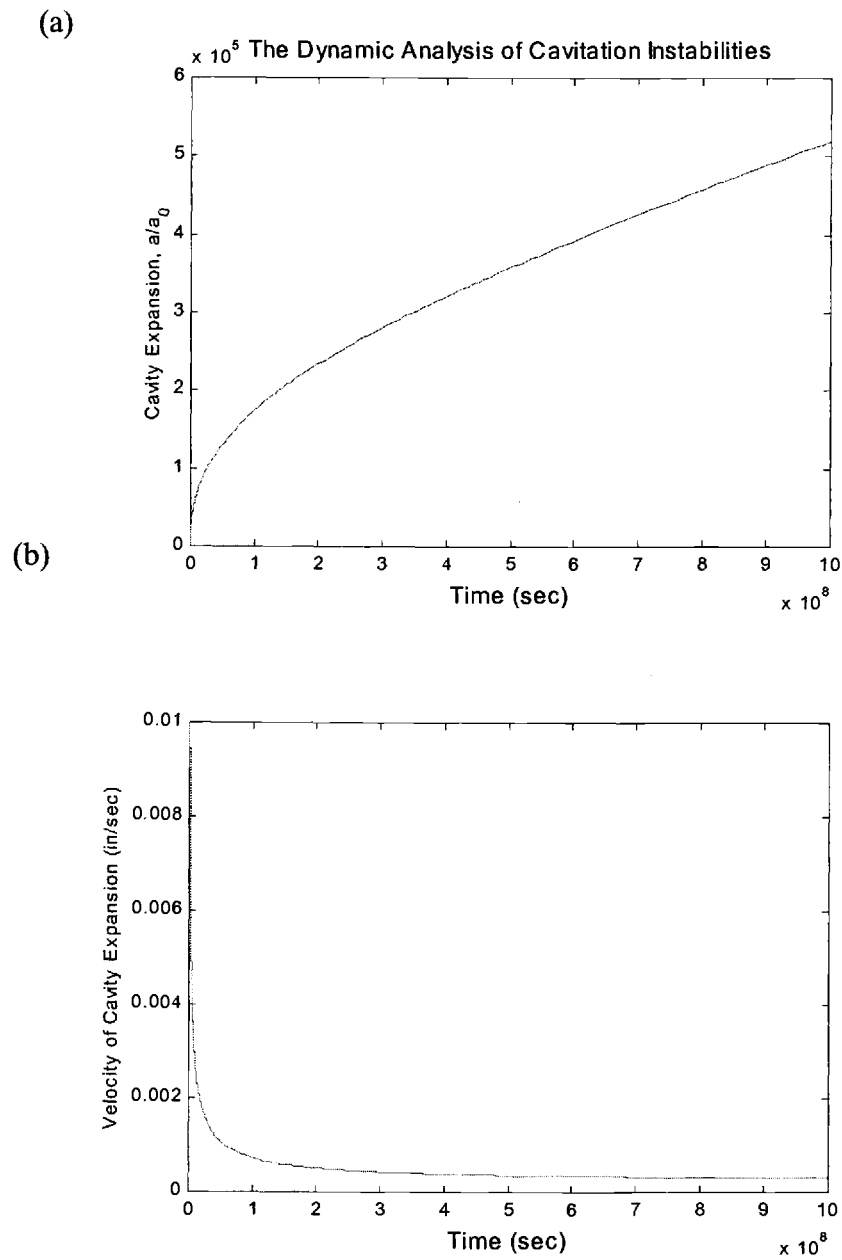
Figure 3.9 Numerical solution (with only inertia effects) under spherically-symmetric loading at $\sigma_\infty = 163.093$ Ksi (equal to the cavitation limit stress) for (a) cavity expansion vs. time and (b) velocity of cavity expansion vs. time. The step loading is suddenly applied for magnitude of 163.093 Ksi and remains constant for all time.

(a)
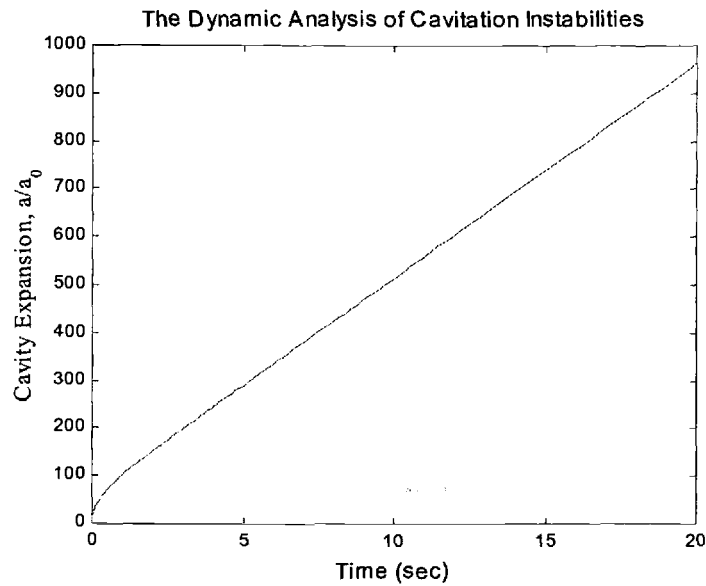
(b)
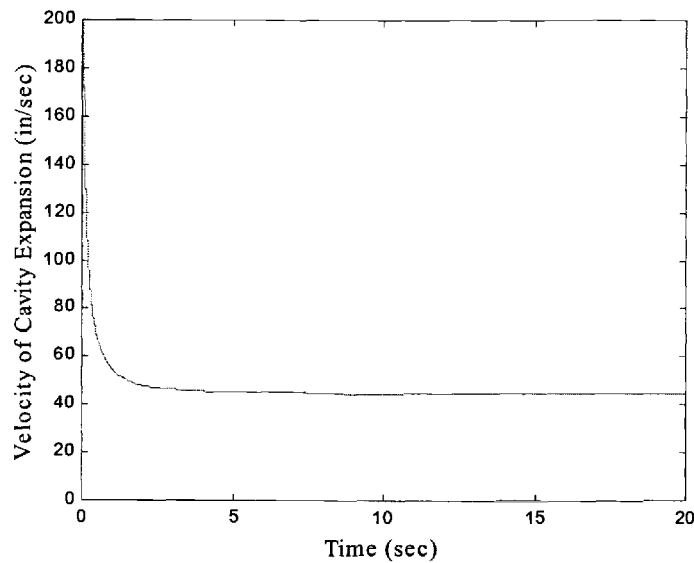
Figure 3.10 Numerical solution (with only inertia effects) under spherically-symmetric loading at $\sigma_\infty = 163.094$ Ksi (slightly above the cavitation limit stress, $S_{cr} = 163.093$ Ksi) for (a) cavity expansion vs. time and (b) velocity of cavity expansion vs. time. The step loading is suddenly applied for magnitude of 163.094 Ksi and remains constant for all time.

3.2.4 Cavitation instabilities in a finite solid medium with only inertia effects

We begin by considering a spherical solid medium with internal radius, a, and external radius, b, subjected to uniform tension, σ_0, at $r = b$ as shown in Figure 3.1. The analysis is performed with the same method as the one mentioned in Section 3.2.3. For the elastic response, the boundary conditions are

$$
\begin{aligned}
\sigma_r\big|_{r=a} &= 0, \\
\sigma_r\big|_{r=b} &= \sigma_0 .
\end{aligned}
\tag{3.95}
$$

Substituting equations (3.71) into (3.64) and then integrating with boundary conditions (3.95), we obtain

$$
\ddot{a} = \frac{1}{\rho(1/a - 1/b)}\left[\sigma_0 - \frac{4}{9}E\left(a^3 - a_0^3\right)\left(1/a^3 - 1/b^3\right) \right.
$$
$$
\left. + \rho\dot{a}^2\left\{ \frac{a^4}{2}\left(1/a^4 - 1/b^4\right) - 2a\left(1/a - 1/b\right)\right\}\right].
\tag{3.96}
$$

This differential equation is subjected to the initial conditions: $a = \dot{a} = 0$ at $t = 0$. To simplify, we assume that $b \gg a$; therefore, the initial conditions of the plastic-elastic response are given by equations (3.91) and (3.92).

For the plastic-elastic response, the boundary conditions are

$$
\begin{aligned}
\sigma_r\big|_{r=a} &= 0, \\
\sigma_r\big|_{r=b} &= \sigma_0.
\end{aligned}
\tag{3.97}
$$

and radial stresses must be continuous across the interface

$$
\sigma_r^P\big|_{r=R} = \sigma_r^E\big|_{r=R}.
\tag{3.98}
$$

In the plastic zone, $a < r < R$, the radial stress, σ_r^P, is given by substituting the yield condition (3.7) into equation (3.64) and integrating with the boundary condition (3.97):

$$
\sigma_r^P = 2Y_0 \ln\left(\frac{r}{a}\right) - \rho\left[\frac{1}{r}\left(a^2\ddot{a} + 2a\dot{a}^2\right) - \frac{a^4\dot{a}^2}{2r^4} - a\ddot{a} - \frac{3}{2}\dot{a}^2 \right].
\tag{3.99}
$$

In the elastic zone, $R < r < b$, it follows from equation (3.64) that

$$\sigma_r^E = \sigma_\infty - \frac{4}{9} E \frac{\left(a^3 - a_0^3\right)}{r^3} - \rho \left[\frac{1}{r}\left(a^2 \ddot{a} + 2a\dot{a}^2\right) - \frac{a^4 \dot{a}^2}{2r^4}\right]. \tag{3.100}$$

The relationship between a and R is obtained by equating equations (3.71) with the yield condition (3.7) and then evaluating it at $r = R$:

$$R^3 = \frac{2}{3Y_0} E\left(a^3 - a_0^3\right). \tag{3.101}$$

It follows from the boundary condition (3.98) that the differential equation for cavity radius is

$$\ddot{a} = \frac{1}{\rho a \left(1 - a/b\right)} \left[\sigma_0 - \frac{2Y_0}{3}\left(1 + \ln\left(\frac{2E}{3Y}\left\{1 - \frac{a_0^3}{a^3}\right\}\right)\right) - \frac{2E}{3Y}\frac{\left(a^3 - a_0^3\right)}{b^3}\right.$$
$$\left. - \frac{3}{2}\rho\dot{a}^2\left\{3 - 4a/b + a^4/b^4\right\}\right]. \tag{3.102}$$

The nonlinear differential equation is solved by using ODE 45 code in the Matlab program with the real and absolute tolerance set at 10^{-8}. The material is assumed to be incompressible and elastic/perfectly-plastic solid: $E = 10$ Mpsi, $\varepsilon_y = 0.004$, $v = 0.5$, and $\rho = 0.000259$ lb-sec^2/in^4. Figure 3.18 illustrates an effect of medium size on the prediction of cavitation instabilities when the applied load is equal to 163.094 Ksi ($L/D = 300$) slightly above the cavitation limit stress ($S_{cr} = 163.093$ Ksi). The medium size, L/D, is the ratio of an external radius to an internal radius of a spherical medium at time, $t = 0$. For a small medium size, we found that the cavity grew exponentially when time increased. This is caused by insufficient inertia force to retard the cavity growth. However, a sufficiently large medium size has cavity growth similar to that of an infinite medium.
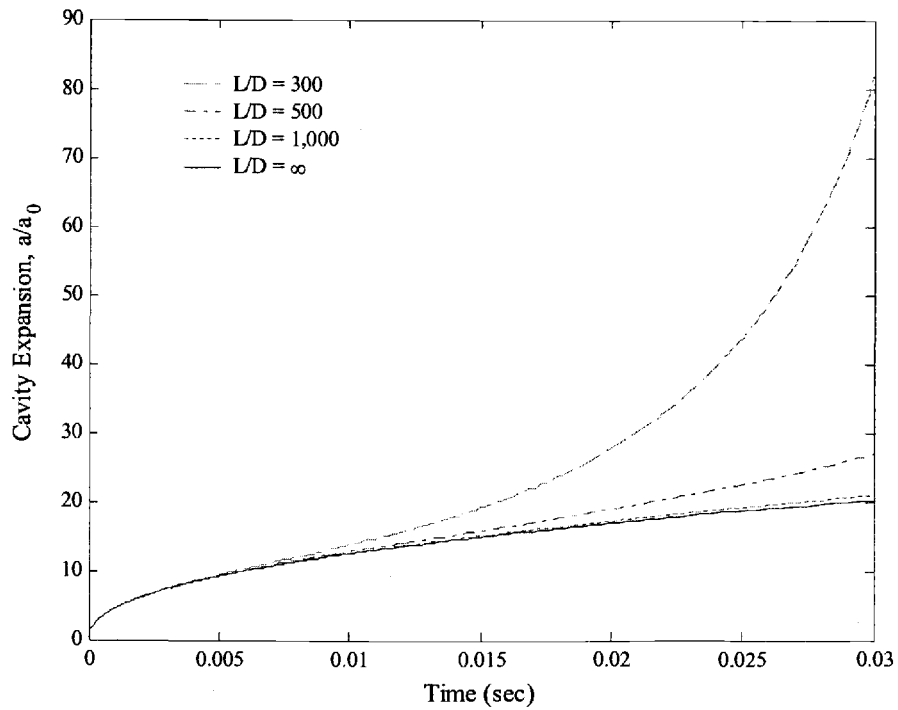
Figure 3.11 The effects of model sizes on the prediction of dynamic responses (with only inertia effects) of cavitation instabilities using a finite body modeling. The plot of cavity expansion vs. time for various model sizes. The step loading is suddenly applied for magnitude of 163.094 Ksi (slightly above the cavitation limit stress, $S_{cr} = 163.093$ Ksi) and remains constant for all the time.

4. THEORY OF CAVITATION INSTABILITIES UNDER AXISYMMETRIC LOADING

Since it is difficult to determine an exact solution for a cavitation instability under axisymmetric loading conditions, we focus our attention on solutions using the finite element method.

4.1 PROBLEM FORMULATION

We use the cylindrical coordinate system (r, θ, and z) to specify a medium configuration as illustrated in Figure 4.1 where X_1 and X_2 represent the r and z-axis respectively. The spherical void and the cylindrical medium have an initial radius, r_0 and R_0 respectively. The boundary conditions satisfy

$$
\begin{aligned}
u_1 \big|_{X_1=0} &= 0, \\
u_2 \big|_{X_2=0} &= 0, \\
P_{x_1} \big|_{X_1=R_0} &= \sigma_2, \\
P_{x_2} \big|_{X_2=R_0} &= \sigma_1,
\end{aligned}
\tag{4.1}
$$

where the ratio of σ_2/σ_1 was kept fixed throughout a numerical analysis.

The governing equations for dynamic response of a medium will be derived by requiring the work of external forces to be absorbed by the work of internal, viscous, and inertia forces for any small kinematically admissible motion. By neglecting body and viscous forces, the principal of virtual work is written as

$$
\int_V \{\delta\varepsilon\}^T \{\sigma\} dV + \int_V \{\delta u\}^T \rho \{\ddot{u}\} dV = \int_S \{\delta u\}^T \{P\} dS,
\tag{4.2}
$$

where δu and $\delta\varepsilon$ are small arbitrary displacements and their corresponding strains respectively, P are prescribed surface tractions, ρ is the mass density of the medium, and V and S are the volume and surface area respectively.
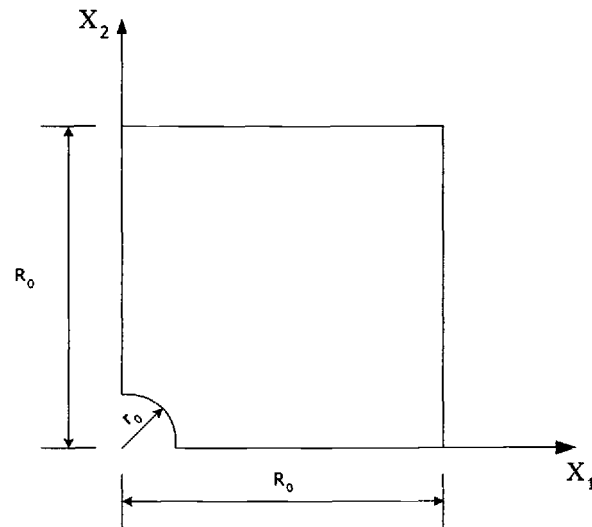
Figure 4.1 A quarter-symmetry model of a body containing a spherical cavity at the center.

4.2 FEA THEORY

The main benefit of a finite element method is the ability to represent a structure as an assemblage of discrete finite elements with the elements being interconnected at nodal points on the element boundaries. In this section, we will go through the theoretical development of a finite element method.

4.2.1 Finite element linear analysis

We begin by considering the finite element formulation of a four-node isoparmetric, axisymmetric element with two degrees of freedom (x_1 and x_2) at each node as illustrated in Figure 4.2. The advantage of using isoparametric formulation is the ability to generate nonrectangular elements. The displacements in the local

coordinates (X_1 and X_2) within an element are assumed to be a function of the displacements at the four finite element nodal points. Therefore, we obtain

$$\{u\} = [H]\{\hat{u}\}, \qquad (4.3)$$

where H is the displacement interpolation matrix, and $\hat{u}$ is the vector of the nodal global displacement components. The displacement interpolations can be written in the matrix form:

$$\begin{Bmatrix} u_1(\xi,\eta) \\ u_2(\xi,\eta) \end{Bmatrix} = \begin{bmatrix} h_1 & 0 & h_2 & 0 & h_3 & 0 & h_4 & 0 \\ 0 & h_1 & 0 & h_2 & 0 & h_3 & 0 & h_4 \end{bmatrix} \begin{Bmatrix} u_1^1 \\ u_2^1 \\ u_1^2 \\ \vdots \\ u_2^4 \end{Bmatrix}, \qquad (4.4)$$

where

$$\begin{aligned} h_1(\xi,\eta) &= \tfrac{1}{4}(1+\xi)(1+\eta), \\ h_2(\xi,\eta) &= \tfrac{1}{4}(1-\xi)(1+\eta), \\ h_3(\xi,\eta) &= \tfrac{1}{4}(1-\xi)(1-\eta), \\ h_4(\xi,\eta) &= \tfrac{1}{4}(1+\xi)(1-\eta). \end{aligned} \qquad (4.5)$$

u_i^j is the displacement of node j in the X_i direction, and ξ and η are the transformed coordinates in the range -1 to 1. In the isoparametric formulation, the element geometry is interpolated in the same way as displacements:

$$\begin{Bmatrix} x_1(\xi,\eta) \\ x_2(\xi,\eta) \end{Bmatrix} = [H] \begin{Bmatrix} x_1^1 \\ x_2^1 \\ x_1^2 \\ \vdots \\ x_2^4 \end{Bmatrix}. \qquad (4.6)$$

where x_i^j is the coordinate of node j in the X_i direction.
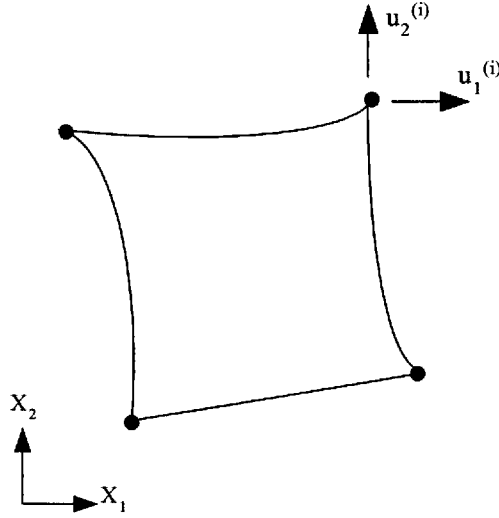
Figure 4.2 Two-dimensional four-node axisymmetric element.

The strain-displacement relations are given as

$$\{\varepsilon\} = \begin{Bmatrix} \varepsilon_{11} \\ \varepsilon_{22} \\ \gamma_{12} \\ \varepsilon_{33} \end{Bmatrix} = \begin{Bmatrix} \partial u_1/\partial x_1 \\ u_2/x_2 \\ \partial u_1/\partial x_2 + \partial u_2/\partial x_1 \\ u_1/x_1 \end{Bmatrix},$$ (4.7)

and it follows from equations (4.4) that

$$\begin{Bmatrix} \varepsilon_{11} \\ \varepsilon_{22} \\ \gamma_{12} \\ \varepsilon_{33} \end{Bmatrix} = \begin{bmatrix} \dfrac{\partial h_1}{\partial x_1} & 0 & \dfrac{\partial h_2}{\partial x_1} & 0 & \dfrac{\partial h_3}{\partial x_1} & 0 & \dfrac{\partial h_4}{\partial x_1} & 0 \\[2mm] 0 & \dfrac{h_1}{x_2} & 0 & \dfrac{h_2}{x_2} & 0 & \dfrac{h_3}{x_2} & 0 & \dfrac{h_4}{x_2} \\[2mm] \dfrac{\partial h_1}{\partial x_2} & \dfrac{\partial h_1}{\partial x_1} & \dfrac{\partial h_2}{\partial x_2} & \dfrac{\partial h_2}{\partial x_1} & \dfrac{\partial h_3}{\partial x_2} & \dfrac{\partial h_3}{\partial x_1} & \dfrac{\partial h_4}{\partial x_2} & \dfrac{\partial h_4}{\partial x_1} \\[2mm] \dfrac{h_1}{x_1} & 0 & \dfrac{h_2}{x_1} & 0 & \dfrac{h_3}{x_1} & 0 & \dfrac{h_4}{x_1} & 0 \end{bmatrix} \begin{Bmatrix} u_1^1 \\ u_2^1 \\ u_1^2 \\ \vdots \\ u_2^4 \end{Bmatrix},$$ (4.8)

$$\{\varepsilon\} = [B]\{\hat{u}\}.$$

Unfortunately, h_1, h_2, h_3, and h_4 are written in terms of ξ and η, but we need to differentiate them with respect to x_1 and x_2. By using the chain rule, we obtain

$$\begin{Bmatrix} \partial h_i / \partial \xi \\ \partial h_i / \partial \eta \end{Bmatrix} = [J] \begin{Bmatrix} \partial h_i / \partial x_1 \\ \partial h_i / \partial x_2 \end{Bmatrix}, \qquad (4.9)$$

where

$$[J] = \begin{bmatrix} \partial x_1 / \partial \xi & \partial x_2 / \partial \xi \\ \partial x_1 / \partial \eta & \partial x_2 / \partial \eta \end{bmatrix}, \qquad (4.10)$$

and $i = 1, 2, 3$, and 4. Multiplying with $[J]^{-1}$ on both sides results in

$$\begin{Bmatrix} \partial h_i / \partial x_1 \\ \partial h_i / \partial x_2 \end{Bmatrix} = [J]^{-1} \begin{Bmatrix} \partial h_i / \partial \xi \\ \partial h_i / \partial \eta \end{Bmatrix}. \qquad (4.11)$$

The stress-strain relations are

$$\{\sigma\} = \begin{Bmatrix} \sigma_1 \\ \sigma_2 \\ \tau_{12} \\ \sigma_3 \end{Bmatrix} = [E]\{\varepsilon\}, \qquad (4.12)$$

where

$$[E] = \frac{(1-\upsilon)E}{(1+\upsilon)(1-2\upsilon)} \begin{bmatrix} 1 & \dfrac{\upsilon}{1-\upsilon} & 0 & \dfrac{\upsilon}{1-\upsilon} \\ \dfrac{\upsilon}{1-\upsilon} & 1 & 0 & \dfrac{\upsilon}{1-\upsilon} \\ 0 & 0 & \dfrac{1-2\upsilon}{2(1-\upsilon)} & 0 \\ \dfrac{\upsilon}{1-\upsilon} & \dfrac{\upsilon}{1-\upsilon} & 0 & 1 \end{bmatrix}. \qquad (4.13)$$

We rewrite the principal of virtual work in equation (4.2) in term of a single finite element as

$$\int_V {}^0\rho\{\delta u\}^T \{\ddot{u}\} dV + \int_V \{\delta \varepsilon\}^T \{\sigma\} dV = \int_S \{\delta u\}^T \{P\} dS, \qquad (4.14)$$

where

$$\{P\} = \begin{Bmatrix} P_{X_1} \\ P_{X_2} \end{Bmatrix}. \qquad (4.15)$$

and $^0\rho$ is the density at time, $t = 0$. Substituting equations (4.3), (4.8), and (4.12) into (4.14), we obtain the equilibrium equation for a single finite element as

$$[M]\{\ddot{\hat{u}}\} + [K]\{\hat{u}\} = \{R\},\qquad(4.16)$$

where M is the mass matrix, K is the stiffness matrix, and F_e is the vector of applied surface tractions

$$[M] = \iiint_V {}^0\rho[H]^T[H]dV,\qquad(4.17)$$

$$[K] = \iiint_V [B]^T[E][B]dV,\qquad(4.18)$$

$$\{R\} = \iint_S [H]^T\{P\}dS.\qquad(4.19)$$

In the quasi static analysis, the finite element equation is obtained from equation (4.16) by neglecting the term associated with the nodal accelerations:

$$[K]\{\ddot{\hat{u}}\} = \{R\}.\qquad(4.20)$$

4.2.2 Finite element nonlinear analysis

Nonlinearity in structures can be classified as material nonlinearity, which is associated with the changes in material properties (i.e., in plasticity), or geometric nonlinearity, which is associated with changes in configuration (i.e., in large deflections of a slender beam). In general, for a time-independent problem in linear analysis both K and R are regarded as independent of $\hat{u}$, whereas in nonlinear analysis K and/or R are regarded as functions of $\hat{u}$. Table 4.1 gives a classification that is used in practical nonlinear analyses.

In a nonlinear analysis, the equilibrium equation of a body has to be established in the current configuration. Moreover, it is necessary to employ an incremental formulation in which a time variable is assumed to describe the loading and the motion of the body. To develop the solution strategy, we use the

Lagrangian (material) formulation by assuming that solutions for the static and kinematic variables from the time 0 to time t are known. Then, we solve for a solution at time, $t + \Delta t$, by using the equilibrium equation at time, $t + \Delta t$, and then we repeat the same processes for each additional time increment until the loading is completely applied to the body.

Table 4.1 Classification of nonlinear analysis.

Type of analysis	Description	Typical formulation used	Stress and strain measures
Materially nonlinear only	Infinitesimal displacements and strains, stress-strain relation is nonlinear	Materially nonlinear only	Engineering stress and strain
Large displacements, large rotations, but small strains	Displacements and rotations of fibers are large, but fiber extensions and angle changes between fibers are small; the stress-strain relation may be linear or nonlinear	1. Total Lagrangian 2. Updated Lagrangian	Second Piola-Kirchhoff stress and Green Lagrange strain
Large displacements, large rotations, and large strains	Fiber extensions and angle changes between fibers are large, fiber displacements and rotations may also be large; the stress-strain relation may be linear or nonlinear	1. Total Lagrangian 2. Updated Lagrangian	Second Piola-Kirchhoff stress and Green Lagrange strain

4.2.2.1 <u>Stress and strain tensor</u>

In a large deformation analysis, the configuration of the body is changed continuously; therefore, auxiliary stress and strain measures are required. In this study, we use the second Piola-Kirchhoff stress, ${}_0^t S$, and Green-lagrange strain, ${}_0^t \varepsilon$. Their benefit over the conventional measures is that their components do not change when the body is undergoing a rigid rotation.

A fundamental measure of the deformation of the body is obtained from the deformation gradient, ${}_0^t X$. In the global coordinates (x_1, x_2, and x_3) at time t, ${}_0^t X$ is defined as

$$
{}_0^t X = \begin{bmatrix} \partial^t x_1 / \partial^0 x_1 & \partial^t x_1 / \partial^0 x_2 & \partial^t x_1 / \partial^0 x_3 \\ \partial^t x_2 / \partial^0 x_1 & \partial^t x_2 / \partial^0 x_2 & \partial^t x_2 / \partial^0 x_3 \\ \partial^t x_3 / \partial^0 x_1 & \partial^t x_3 / \partial^0 x_2 & \partial^t x_3 / \partial^0 x_3 \end{bmatrix},
\tag{4.21}
$$

where superscript, 0, represents a component at time $t = 0$. For a two-dimensional axisymmetric element, ${}_0^t X$ becomes

$$
{}_0^t X = \begin{bmatrix} \partial^t x_1 / \partial^0 x_1 & \partial^t x_1 / \partial^0 x_2 & 0 \\ \partial^t x_2 / \partial^0 x_1 & \partial^t x_2 / \partial^0 x_2 & 0 \\ 0 & 0 & {}^t x_1 / {}^0 x_1 \end{bmatrix}.
\tag{4.22}
$$

The second Piola-Kirchhoff stresses, ${}_0^t S$, and the Green-lagrange strains, ${}_0^t \varepsilon$, are written as

$$
{}_0^t S = \det({}_0^t X) \, {}_t^0 X \, {}^t \sigma \, {}_t^0 X^T,
\tag{4.23}
$$

$$
{}_0^t \varepsilon = \tfrac{1}{2} \left({}_0^t X^T \, {}_0^t X - I \right),
\tag{4.24}
$$

where ${}^t \sigma$ is the Cauchy stress tensor at time t, and I is the identity matrix. Substituting equation (4.23) and (4.24) into (4.14) results in

$$
\int_{{}^0 V} {}^0 \rho \{\delta u\}^T \{{}^t \ddot{u}\} d^0 V + \int_{{}^0 V} \{{}_0^t \varepsilon\}^T \{{}_0^t S\} d^0 V = \int_{{}^0 S} \{\delta u\}^T \{{}^t F\} d^0 S.
\tag{4.25}
$$

This equation is the basic expression for the finite element formulation of nonlinear analysis.

4.2.2.2 Total and updated lagrangian formulation.

To develop a governing equation for the nonlinear finite element method, there are two well-known formulations: the total lagrangian formulation (*TL*) and updated lagragian formulation (*UL*). The *TL* formulation has been recognized as the Lagrangian formulation in which the solution schemes are referred to an initial configuration at time *0*. However, the *UL* formulation is based on the same procedures that are used in the *TL* formulation, but the solution schemes are referred to the last calculated configuration. Both the *TL* and *UL* formulations include all kinematic nonlinear effects due to large displacements, large rotations, and larges strains, but whether the large strain behavior is modeled appropriately depends on the constitutive relations. The only advantage of using one formulation rather than the other depends on its greater numerical efficiency. By manipulating equation (4.25), Bathe (1996) arrived at the basic incremental equations used in the finite element formulations.

Using the *TL* formulations, he obtained:

1. Dynamic analysis with the implicit time integration:

$$[M]\left\{{}^{t+\Delta t}\Delta\ddot{\hat{u}}\right\} + \left[{}_0^t K_L + {}_0^t K_{NL}\right]\{\Delta\hat{u}\} = \left\{{}^{t+\Delta t}R\right\} - \left\{{}_0^t F\right\}, \tag{4.26}$$

2. Dynamic analysis with the explicit time integration:

$$[M]\left\{{}^t\ddot{\hat{u}}\right\} = \left\{{}^t R\right\} - \left\{{}_0^t F\right\}, \tag{4.27}$$

3. Static analysis:

$$\left[{}_t^t K_L + {}_t^t K_{NL}\right]\{\Delta\hat{u}\} = \left\{{}^{t+\Delta t}R\right\} - \left\{{}_0^t F\right\}, \tag{4.28}$$

and using the *UL* formulations yields:

4. Dynamic analysis with the implicit time integration:

$$[M]\left\{{}^{t+\Delta t}\ddot{\hat{u}}\right\} + \left[{}_t^t K_L + {}_t^t K_{NL}\right]\{\Delta\hat{u}\} = \left\{{}^{t+\Delta t}R\right\} - \left\{{}_t^t F\right\}, \tag{4.29}$$

5. Dynamic analysis with the explicit time integration:

$$[M]\left\{{}^t\ddot{\hat{u}}\right\} = \left\{{}^t R\right\} - \left\{{}_t^t F\right\}, \tag{4.30}$$

6. Static analysis:

$$\left[{}_t^t K_L + {}_t^t K_{NL} \right] \{\Delta \hat{u}\} = \left\{ {}^{t+\Delta t} R \right\} - \left\{ {}_t^t F \right\},$$ (4.31)

where

M = Time-independent mass matrix,

${}^t K$ = Linear strain incremental strain incremental stiffness matrix, not including the initial displacement effect,

${}_0^t K_L, {}_t^t K_L$ = Linear strain incremental stiffness matrices,

${}_0^t K_{NL}, {}_t^t K_{NL}$ = Nonlinear strain incremental stiffness matrices,

${}^{t+\Delta t} R$ = Vector of externally applied nodal point load at time $t+\Delta t$; this vector is also used at time t in explicit time integration,

${}^t F, {}_0^t F, {}_t^t F$ = Vectors of nodal point forces equivalent to the element stresses at time t; these vectors are also employed corresponding to time $t+\Delta t$,

$\Delta \hat{u}$ = Vector of increments in the nodal point displacements

${}^t \ddot{u}$ = Vector of nodal point accelerations at time t; this vector is also employed corresponding to time $t+\Delta t$.

In this finite element discretization, it is assumed that damping effects are negligible and the externally applied loads are deformation-independent. The corresponding matrix and vector evaluations are summarized in Table (4.2). In the case of the *TL* and *UL* formulations, the procedure of generating matrices and vectors are described in details in Appendix B.

Table 4.2 Finite element matrix formulations.

Analysis types	Matrix evaluations
All Analyses	$\left[M^{t+\Delta t}\right]\{\ddot{u}\} = \left(\int_{{}^{0}V} {}^{0}\rho [H]^{T}[H] dV\right)\{\ddot{u}\}$ $\{{}^{t+\Delta t}R\} = \int_{{}^{0}S}[H]^{T}\{{}^{t+\Delta t}_{0}f\} d\,{}^{0}S$
Total Largrangian formulation	$\left[{}^{t}_{0}K_{L}\right]\{\hat{u}\} = \left(\int_{{}^{0}V}\left[{}^{t}_{0}B_{L}\right]^{T}\left[{}_{0}E\right]\left[{}^{t}_{0}B_{L}\right] d\,{}^{0}V\right)\{\hat{u}\}$ $\left[{}^{t}_{0}K_{NL}\right]\{\hat{u}\} = \left(\int_{{}^{0}V}\left[{}^{t}_{0}B_{NL}\right]^{T}\left[{}^{t}_{0}S\right]\left[{}^{t}_{0}B_{NL}\right] d\,{}^{0}V\right)\{\hat{u}\}$ $\{{}^{t}_{0}F\} = \int_{{}^{0}V}\left[{}^{t}_{0}B_{L}\right]^{T}\{{}^{t}_{0}S\} d\,{}^{0}V$
Updated Largrangian formulation	$\left[{}^{t}_{t}K_{L}\right]\{\hat{u}\} = \left(\int_{{}^{t}V}\left[{}^{t}_{t}B_{L}\right]^{T}\left[{}_{t}E\right]\left[{}^{t}_{t}B_{L}\right] d\,{}^{t}V\right)\{\hat{u}\}$ $\left[{}^{t}_{t}K_{NL}\right]\{\hat{u}\} = \left(\int_{{}^{t}V}\left[{}^{t}_{t}B_{NL}\right]^{T}\left[{}^{t}\sigma\right]\left[{}^{t}_{t}B_{NL}\right] d\,{}^{t}V\right)\{\hat{u}\}$ $\{{}^{t}_{t}F\} = \int_{{}^{t}V}\left[{}^{t}_{t}B_{L}\right]^{T}\{{}^{t}\sigma\} d\,{}^{t}V$

4.3 Numerical procedures for nonlinear finite element analysis

In this section, we study numerical techniques used to evaluate nonlinear finite element equations in both static and dynamic analyses as presented by Bathe (1996).

4.3.1 Static analysis

As we discussed in Section 4.2.2.2 that basic equations in nonlinear analysis are solved at time $t+\Delta t$. Therefore, the force equilibriums are written as

$$\{{}^{t+\Delta t}R\} - \{{}^{t+\Delta t}F\} = 0, \qquad (4.32)$$

where the vector ${}^{t+\Delta t}R$ stores the externally applied nodal load, and ${}^{t+\Delta t}F$ is the vector of nodal point forces that are equivalent to the element stresses. Since the

nodal forces $^{t+\Delta t}F$ depend nonlinearly on the nodal displacements, it is necessary to iterate in the solution of equation (4.32) so that an out-of-balance forces become zero.

4.3.1.1 Modified Newton-Raphson method

One of the most well-known iteration schemes for the solution of nonlinear finite element equations is the modified Newton-Raphson method. This numerical scheme is suitable for the static and transient analyses. Basically, it can be written as

$$\{\Delta R\}^{(i-1)} = \{{}^{t+\Delta t}R\} - \{{}^{t+\Delta t}F\}^{(i-1)}, \tag{4.33}$$

$$\left[{}^{t}K\right]\{\Delta\hat{u}\}^{(i)} = \{\Delta R\}^{(i-1)}, \tag{4.34}$$

$$\{{}^{t+\Delta t}\hat{u}\}^{(i)} = \{{}^{t+\Delta t}\hat{u}\}^{(i-1)} + \{\Delta\hat{u}\}^{(i)}, \tag{4.35}$$

where

$$\begin{aligned} \{{}^{t+\Delta t}\hat{u}\}^{(0)} &= \{{}^{t}\hat{u}\}, \\ \{{}^{t+\Delta t}F\}^{(0)} &= \{{}^{t}F\}, \end{aligned} \tag{4.36}$$

and $i = 1, 2, 3, \ldots$. These equations were obtained by linearizing the response of the finite element system about conditions at time t. In each iteration, we calculate an out-of-balance load vector in equation (4.33), which yields an increment in displacements obtained in equation (4.34). Then, we continue the iteration until the out-of-balance load vector, $\Delta R^{(i-1)}$, or the displacement increments, $\Delta\hat{u}^{(i)}$, are sufficiently small as illustrated in Figure 4.3.

The convergence rate of this procedure is generally slower than the full-Newton-Raphson procedure, since it uses the same stiffness matrix, ${}^{t}K$, for some increments in each time step. The frequency of the updated stiffness matrix

depends on the degree of nonlinearity of the system response. Nonetheless, it requires fewer reformations and inversions on ^tK.
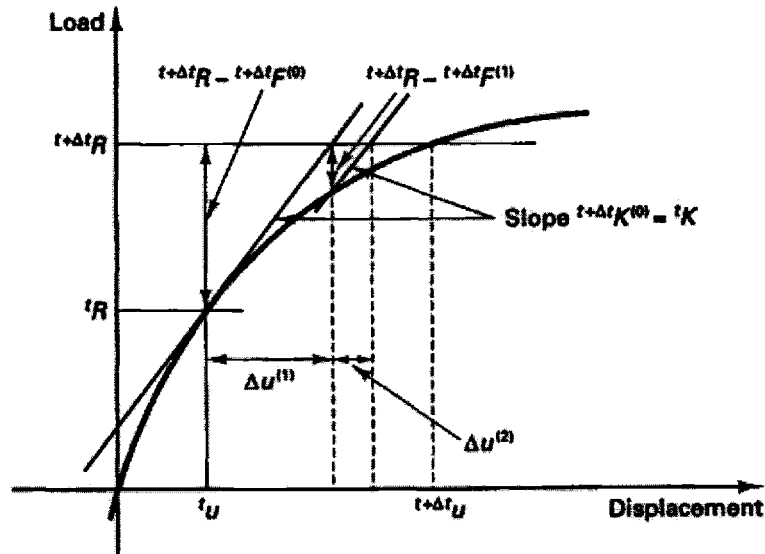
Figure 4.3 Illustration of Modified Newton-Raphson iteration scheme (for single degree of freedom simplification).

4.3.1.2 Arc-length method

The arc-length method is suitable for nonlinear static equilibrium solution of unstable problems. Applications of arc-length method involve the tracing of a complex path in the load-displacement response into the buckling/post buckling regimes. The arc-length method uses the explicit spherical iterations to maintain the orthogonality between the arc-length radius and orthogonal directions. It is assumed that all load magnitudes are controlled by a single scalar parameter, i.e. the total load factor, λ. Unsmooth or discontinuous load-displacement response in the cases often seen in contact analyses and elastic-perfectly plastic analyses cannot be traced effectively by the arc-length solution method.

Mathematically, the arc-length method can be viewed as the trace of the total load factor. Therefore, all strategies of the Newton-Raphson method are still the basic method for the arc-length solution. As the displacement vectors and the scalar load factor are treated as unknowns, the arc-length method itself is an automatic load step method. In the arc–length procedure, the governing finite element equations at time $t+\Delta t$ are written as

$$^{t+\Delta t}\lambda\{R\}-\left\{^{t+\Delta t}F\right\}=0, \tag{4.37}$$

where $^{t+\Delta t}\lambda$ is an unknown scalar load factor (normally within the range $-1 \geq \lambda \geq 1$). The nonlinear equilibrium equations are rewritten in term of total load factor, λ, as

$$\left[^{t}K\right]\{\Delta\hat{u}\}^{(i)} = \left(^{t+\Delta t}\lambda^{(i-1)} + \Delta\lambda^{(i)}\right)\{R\}-\left\{^{t+\Delta t}F\right\}^{(i-1)}, \tag{4.38}$$

where

$$\begin{aligned}
\{\Delta\hat{u}\}^{(i)} &= {}^{t+\Delta t}\hat{u}^{(i)} - {}^{t}\hat{u}, \\
\Delta\lambda^{(i)} &= {}^{t+\Delta t}\lambda^{(i)} - {}^{t}\lambda.
\end{aligned} \tag{4.39}$$

In order to solve equation (4.38) in an incremental manner, we rewritte it as

$$\begin{aligned}
\left[^{t}K\right]\{\Delta\hat{u}_{I}\}^{(i)} &= {}^{t+\Delta t}\lambda^{(i-1)}\{R\}-\left\{^{t+\Delta t}F\right\}^{(i-1)}, \\
\left[^{t}K\right]\{\Delta\hat{u}_{II}\} &= R, \\
\{\Delta\hat{u}\}^{(i)} &= \{\Delta\hat{u}_{I}\}^{(i)} + \Delta\lambda^{(i)}\{\Delta\hat{u}_{II}\},
\end{aligned} \tag{4.40}$$

where

$$\begin{aligned}
\lambda^{(i)} &= \lambda^{(i-1)} + \Delta\lambda^{(i)}, \\
\{\hat{u}\}^{(i)} &= \{\hat{u}\}^{(i-1)} + \{\Delta\hat{u}\}^{(i)}.
\end{aligned} \tag{4.41}$$

Furthermore, there are two fundamental methods generally used to determine an additional relationship between $\Delta\lambda^{(i)}$ and $\Delta\hat{u}^{(i)}$: the spherical constant arc-length criterion and the constant increment of external work criterion. In the spherical constant arc-length criterion (Crisfield, 1981 and Ram, 1981), this relationship is given as

$$\left(\lambda^{(i)}\right)^2 + \frac{\{\Delta\hat{u}\}^{(i)^T}\{\Delta\hat{u}\}^{(i)}}{\beta} = \left(\Delta l\right)^2,$$ (4.42)

where Δl is the arc length for the step as illustrated in Figure 4.4a, and β is a normalizing factor. Substituting equations (4.41) into (4.42) results in a quadratic equation in $\Delta\lambda^{(i)}$. To initialize this numerical computation, the initial arc-length radius must be defined. The arc-length radius will be updated at each time step according to the degree of nonlinearity that is involved during the analysis.

In the constant increment of external work criterion (Bathe and Dovorkin, 1999), this relationship is written as

$$\left(^t\lambda + \tfrac{1}{2}\Delta\lambda^{(i)}\right)\{R\}^T\{\Delta\hat{u}\}^{(i)} = W,$$
$$\left(^{t+\Delta t}\lambda^{(i-1)} + \tfrac{1}{2}\Delta\lambda^{(i)}\right)\{R\}^T\{\Delta\hat{u}\}^{(i)} = 0,$$ (4.43)

where W is an increment value of external work, which is selected based on the history of iterations in the previous incremental steps, as illustrated in Figure 4.4b. Consequently, $\Delta\lambda^{(1)}$ is directly calculated from equation (4.43) and then the $\Delta\lambda^{(i)}$ values for $i = 2, 3, \ldots$ are obtained from equation (4.43) as

$$\Delta\lambda^{(i)} = -\frac{\{R^T\}\{\Delta\hat{u}_I\}^{(i)}}{\{R^T\}\{\Delta\hat{u}_{II}\}}.$$ (4.44)

For problems with the sharp turns in the arc-length curve or path dependent materials, it is necessary to limit the arc-length radius (arc-length load step size).
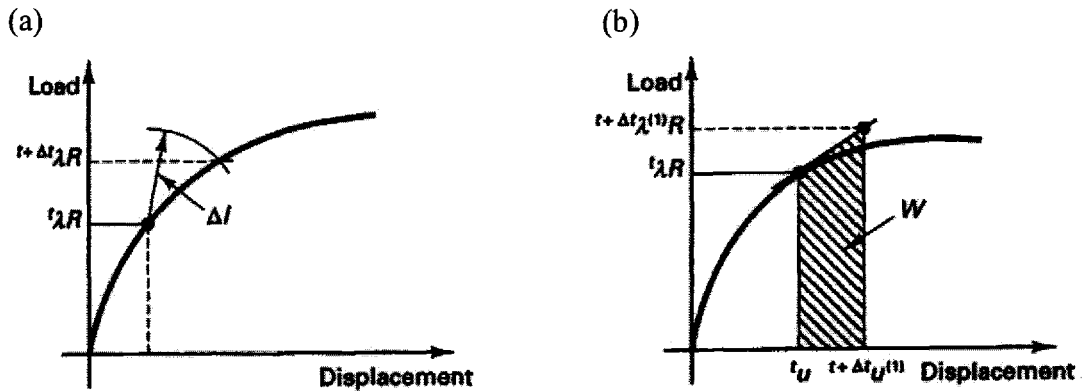
Figure 4.4 Load-displacement constraint criterion (single degree of freedom simplification) for (a) Spherical constant arc-length criterion and (b) Constant increment of external work criterion.

4.3.1.3 Convergence Criteria

If an incremental solution strategy based on iterative methods is to be effective, convergence criteria should be established for the termination of the iteration. At the end of each iteration, the solution should be checked whether it has converged in with preset tolerances, or whether the iteration is diverging. If the convergence tolerances are too loose, inaccurate results are obtained, and if the tolerances are too tight, much computational effort is spent to obtain needless accuracy. Similarly, an ineffective divergence check can terminate the iteration when the solution is not actually diverging or force the iteration to search for an unattainable solution.

Since we are seeking the displacement configuration corresponding to time $t+\Delta t$, it is natural to require that the displacements at the end of each iteration be within a certain tolerance of the true displacement solution. Hence, the first convergence criterion is given as

$$\frac{\left\|\Delta\hat{u}^{(i)}\right\|_2}{\left\|^{t+\Delta t}\hat{u}\right\|_2} = \varepsilon_D, \tag{4.45}$$

where ε_D is a displacement convergence tolerance. The vector $^{t+\Delta t}\hat{u}$ is unknown and must be approximated. Practically, it is appropriate to use the last calculated $^{t+\Delta t}\hat{u}^{(i)}$ as an approximation to $^{t+\Delta t}\hat{u}$. However, in some problems the actual solution may still be far from the value obtained when convergence is measured using equation (4.45) with $^{t+\Delta t}\hat{u}^{(i)}$. This is the case when the calculated displacements change only little in each iteration, but continue to change for many iterations, for example, in elastoplastic analysis under loading conditions.

A second convergence criterion is obtained by measuring the out-of-balance load vector. For example, we may require the norm of the out-of-balance load vector be within a preset tolerance, ε_F, of the original load increment:

$$\frac{\left\| ^{t+\Delta t}R - ^{t+\Delta t}F^{(i)} \right\|_2}{\left\| ^{t+\Delta t}R - {}^{t}F^{(i)} \right\|_2} \le \varepsilon_F. \tag{4.46}$$

These criteria (4.45) and (4.46) are not normally considered as the termination measure. For example, in an elastic-plastic system with a very small strain-hardening modulus entering the plastic region, the out-of-balance loads may be very small while the displacements may still be grossly in error. Thus, in general it is required that ε_D and ε_F are set to a very small values.

In order to provide some indication of when both displacements and the forces are near their equilibrium values, a third convergence criterion may be useful, in which the increment in energy during each iteration is compared to the initial internal energy increment. Convergence is assumed to be reached when a present energy tolerance, ε_E, satisfies

$$\{\Delta\hat{u}\}^{(i)^T} \left[\left\{ ^{t+\Delta t}\mathrm{R} \right\} - \left\{ ^{t+\Delta t}\mathrm{F} \right\}^{(i-1)} \right] \le \varepsilon_E \left[\left(\{\Delta\hat{u}\}^{(i)^T} \left(\left\{ ^{t+\Delta t}\mathrm{R} \right\} - \left\{ ^{t}\mathrm{F} \right\}^{(i-1)} \right) \right) \right]. \tag{4.47}$$

This convergence criterion is most attractive in the termination measure since it contains both displacements and forces.

4.3.2 Dynamic analysis

In nonlinear dynamic analysis, a numerical integration scheme is basically formulated based on an iterative method as mentioned in Section 4.3.1.1. In addition to that, we have to construct a numerical scheme in such a way that it contains both iterative and numerical time integration procedures that can march a solution forward in time.

4.3.2.1 Implicit Integration

All implicit time integration schemes for linear dynamic analysis can also be employed in nonlinear dynamic response calculations. One of the effective numerical techniques generally used is the trapezoidal method.

In order to construct an iterative procedure, we use the modified Newton-Raphson method to enforce equilibrium of a system at time $t+\Delta t$ as mentioned in Section 4.3.1.1. The governing equilibrium equations (neglecting the effects of the damping matrix) become

$$[M]\left\{{}^{t+\Delta t}\ddot{u}\right\}^{(i)} + \left[{}^{t}K\right]\left\{\Delta\hat{u}\right\}^{(i)} = \left\{{}^{t+\Delta t}R\right\} - \left\{{}^{t+\Delta t}F\right\}^{(i-1)}, \tag{4.48}$$

$$\left\{{}^{t+\Delta t}\ddot{u}\right\}^{(i)} = \left\{{}^{t+\Delta t}\ddot{u}\right\}^{(i-1)} + \left\{{}^{t+\Delta t}\Delta\ddot{u}\right\}^{(i)}. \tag{4.49}$$

Using the trapezoid method, the following assumptions are employed:

$$\left\{{}^{t+\Delta t}\hat{u}\right\} = \left\{{}^{t}\hat{u}\right\} + \frac{\Delta t}{2}\left(\left\{{}^{t}\dot{u}\right\} + \left\{{}^{t+\Delta t}\dot{u}\right\}\right), \tag{4.50}$$

$$\left\{{}^{t+\Delta t}\dot{u}\right\} = \left\{{}^{t}\dot{u}\right\} + \frac{\Delta t}{2}\left(\left\{{}^{t}\ddot{u}\right\} + \left\{{}^{t+\Delta t}\ddot{u}\right\}\right). \tag{4.51}$$

Manipulating the relations in equations (4.49) to (4.51) results in

$$\left\{{}^{t+\Delta t}\ddot{u}\right\}^{(i)} = \frac{4}{\Delta t^2}\left(\left\{{}^{t+\Delta t}\hat{u}\right\}^{(i-1)} - \left\{{}^{t}\hat{u}\right\} + \left\{\Delta\hat{u}\right\}^{(i)}\right) - \frac{4}{\Delta t}\left\{{}^{t}\dot{u}\right\} - \left\{{}^{t}\ddot{u}\right\}, \tag{4.52}$$

and substituting it into equation (4.48) yields

$$\left[{}^{t}\hat{K} \right]\{\Delta\hat{u}\}^{(i)} = \{ {}^{t+\Delta t}R \} - \{ {}^{t+\Delta t}F \}^{(i-1)}$$
$$-[M]\left(\frac{4}{\Delta t^2}\left(\{ {}^{t+\Delta t}\hat{u} \}^{(i-1)} - \{ {}^{t}\hat{u} \} \right) - \frac{4}{\Delta t}\{ {}^{t}\dot{\hat{u}} \} - \{ {}^{t}\ddot{u} \} \right), \tag{4.53}$$

where

$$\left[{}^{t}\hat{K} \right] = \left[{}^{t}K \right] + \frac{4}{\Delta t^2}[M]. \tag{4.54}$$

We now notice that the iterative equations in dynamic nonlinear analysis using implicit time integration are of the same form as the equations that we considered in static nonlinear analysis, but both the coefficient matrix and the nodal point force vector contain contributions from inertia of the system. Therefore, all iterative solution strategies for static analysis are also directly applicable to the solution of equation (4.53). Since the inertia of the system renders its dynamic response, this results in faster convergence rate than in a pure static response because of the contribution of the mass matrix to the coefficient matrix. The convergence of dynamic analysis is always achieved by providing Δt to be sufficiently small. Additionally, the solution approach is effective if a diagonal mass matrix is employed. This mass matrix is obtained by using the lumped mass method.

The convergence tolerances discussed in Section 4.3.1.3 are also employed in this analysis, but included the effect of inertia. The convergence is reached when the following conditions are satisfied:

$$\frac{\left\| {}^{t+\Delta t}R - {}^{t+\Delta t}F^{(i-1)} - M {}^{t+\Delta t}\ddot{u}^{(i-1)} \right\|_2}{RNORM} \leq RTOL, \tag{4.55}$$

$$\frac{\{\Delta\hat{u}\}^{(i)^T}\left(\{ {}^{t+\Delta t}R \} - \{ {}^{t+\Delta t}F \}^{(i-1)} - [M]\{ {}^{t+\Delta t}\ddot{u} \}^{(i-1)} \right)}{\{\Delta\hat{u}\}^{(1)^T}\left(\{ {}^{t+\Delta t}R \} - \{ {}^{t}F \} - [M]\{ {}^{t}\ddot{u} \} \right)} \leq ETOL, \tag{4.56}$$

where $RTOL$ is a force tolerance and $ETOL$ is an energy tolerance. Iteration with sufficiently tight convergence is required. Energy is lost if the convergence tolerance is not tight enough, but depending on problem being considered the

predicted response may also blow up if iteration is not used. In practice, it is frequently found that only a few iterations per time step are required to obtain a stable condition.

4.3.2.2 Explicit Integration

The most common explicit time integration method used in nonlinear dynamic analysis is the central difference method. As in linear analysis, the equilibrium of the finite element system is considered at time, t, in order to calculate the displacements at time, $t+\Delta t$. Neglecting the effect of the damping matrix, we operate for each discrete time step solution on the equations as

$$[M]\{^{t}\ddot{u}\} = \{^{t}R\} - \{^{t}F\}. \tag{4.57}$$

Using the central difference of time integration, the following assumptions are employed

$$\{^{t}\ddot{u}\} = \frac{1}{\Delta t^{2}}\left(\{^{t-\Delta t}\hat{u}\} - 2\{^{t}\hat{u}\} + \{^{t+\Delta t}\hat{u}\}\right), \tag{4.58}$$

$$\{^{t}\dot{u}\} = \frac{1}{2\Delta t}\left(\{^{t+\Delta t}\hat{u}\} - \{^{t-\Delta t}\hat{u}\}\right). \tag{4.59}$$

Substituting the relations for equations (4.58) and (4.59) into (4.57) yields

$$\frac{1}{\Delta t^{2}}[M]\{^{t+\Delta t}\hat{u}\} = \{^{t}R\} - \{^{t}F\} + \frac{1}{\Delta t^{2}}[M]\left(2\{^{t}\hat{u}\} - \{^{t-\Delta t}\hat{u}\}\right), \tag{4.60}$$

from which we can solve for $^{t+\Delta t}\hat{u}$. The solution are therefore simply corresponds to a forward marching in time. The main advantage of the method is that with a diagonal matrix, M, the solution of $^{t+\Delta t}\hat{u}$ does not involve a triangular factorization of a coefficient matrix.

The disadvantage of using the central difference method lies in the severe time step restriction. For stability, the time step size, Δt, must be smaller than a critical time step Δt_{cr}, which is equal to T_n/π, where T_n is the smallest period in the

finite element system. This time step restriction was derived considering a linear system, but the result is also applicable to nonlinear analysis. Since for each time step the nonlinear response calculation may be thought of as a linear analysis. However, whereas in a linear analysis the stiffness properties remain constant, in a nonlinear analysis these properties change during the response calculations. These changes in the material and/or geometric conditions enter into the evaluations of the force vector, ^{t}F. Since the value of T_n is not constant during the calculation, the time step, Δt, needs to be decreased if the system stiffens, and this time step adjustment must be performed in a conservative manner, so that with certainty the condition, $T_n/\pi \geq \Delta t$, is satisfied at all times.

4.3.3 Rezoning the mesh

The Lagrangian formulation is used to generate the finite element equations in the ABAQUS program (2001). The mesh is attached to the material and deformed with the material. In large deformation analysis, elements may become so severely distorted during the analysis that they no longer provide a good discretization of the problem. Therefore, it is necessary to rezone the mesh by mapping the solution from a deformed mesh to a new mesh so that the analysis can continue.

The rezoning procedure consists of an interpolation technique that extrapolates the solution at integration points of the old mesh to nodes of each element and then averaging these values over all elements. Next, the location of each integration point in the new mesh is obtained with respect to the old mesh. Finally, the solution at the nodes of the old mesh is interpolated to integrating points of the new element. After rezoning, it can be expected that there will be some discontinuity in the solution because of the change in the mesh. Therefore, if the discontinuity is significant, ABAQUS will provide a message that the meshes

are too coarse or that the rezoning should be done at an earlier stage before too severe distortion occurred. This verification process helps to improve the accuracy of the rezoning scheme.

4.3.4 Quasi-static analysis using an explicit dynamic formulation

Applying the explicit dynamic procedure to a quasi-static problem requires some special considerations. Since a static solution is, by definition, a long-time solution, it is often computationally impractical to analyze the simulation in its natural time scale, which would require an excessive number of small time increments. To obtain an economical solution, the event must be accelerated in some way. However, the problem arises if as the event is accelerated, the state of static equilibrium evolves into a state of dynamic equilibrium in which inertia forces become more dominant. The goal is to model the process in a short time period in which inertial forces remain insignificant.

Let us consider an example shown in Figure 4.5. The Figure 4.5 shows two cases of an elevator full of passenger. In the slow case the door opens and a man walks in. To make room, the occupants adjacent to the door slowly push their neighbors, who push their neighbors, and so on. This disturbance passes through the elevator until the people next to the door cannot move. A series of waves pass through the elevator until everyone has reached a new equilibrium position. If you increase your speed slightly, you will shove your neighbors more forcefully than before, but in the end everyone will end up in the same position as in the slow case. In the fast case the door opens and a man runs into the elevator at high speed, permitting the occupants no time to rearrange themselves to accommodate him. He will injure the two people directly in front of the door, while the other occupants will be unaffected.

The same thing is true for a quasi-static analysis. The speed of the analysis is often can be increased substantially without severely degrading the quality of the quasi-static solution; the end result of the slow case and somewhat accelerated case are nearly the same. However, if the analysis speed is increased to a point at which inertial effects dominate, the solution tends to localize, and results are quite different from the quasi-static solution. In practice, the frequency of excitation applied to a system has to be less than roughly one-third of the lowest natural frequency of a system.
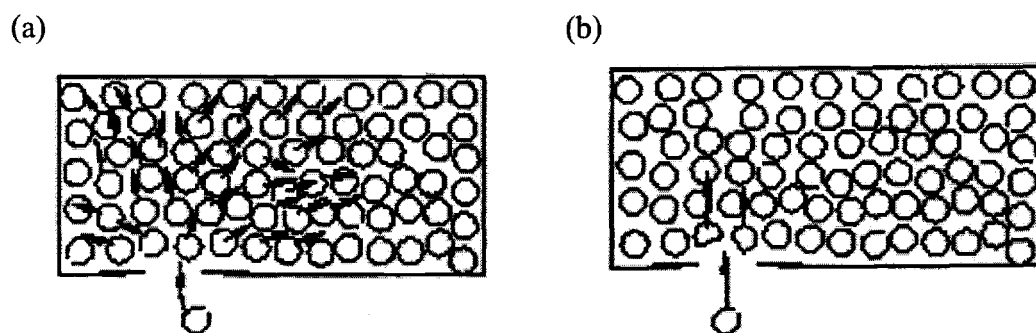
(a) (b)

Figure 4.5 Analogy on an effect of loading rates for (a) a slow case and (b) a fast loading case.

5. FEA RESULTS AND DISCUSSION

Cavitation instability in elastic-plastic solids subjected to spherically-symmetric and axisymmetric loadings was studied using the finite element nonlinear program, ABAQUS (2001). In this study, we focused our attention in both quasi-static and dynamic analyses.

To simulate cavitation instabilities using a finite body, one of the most important parameters affecting a finite element solution is model size, L/D, which is defined as the ratio of an outer radius of the spherical model (or a height of the cylindrical model) to the cavity radius as illustrated in Figures 5.1 and 5.10 respectively. In quasi-static analysis under axisymmetric loading, the effect of model sizes on FEA solutions was studied and discussed in Appendix C. Here, the variation of maximum principal stress and remote axial strain at the FEA prediction of failure for various model sizes are plotted as illustrated in Figure C.1-C.2. It was found that with a sufficiently large model size (i.e., $L/D = 15,000$), we have a cavitation instability similar to that of an infinite model size.

5.1 QUASI-STATIC ANALYSIS OF CAVITATION INSTABILITIES UNDER SPHERICALLY-SYMMETRIC LOADING

The objective of this study was to validate a finite element solution with an analytical solution presented in Chapter 3. A model of cavity expansion in a finite body subjected to remote spherically-symmetric loading was accomplished using the ABAQUS/Standard program. The finite element analysis providing an arc-length solver capability of handling limit points was used. Again, cavitation instability is assumed to occur when the slope between remote strain and cavity expansion becomes infinite as discussed in Section 3.1.1.

A single cavity in an infinite body was simulated using a quarter-symmetry model of a body with $L/D = 350$ as illustrated in Figure 5.1. The finite element mesh was constructed using an eight-node, axisymmetric, quadrilateral element. It consisted of 400 elements graded with a fine mesh near the cavity and a coarse mesh away from the cavity. This model size appears to be sufficiently large for representing a solution of a cavitation instability in an infinite body. The tensile load was applied in the radial direction along the outer boundary.
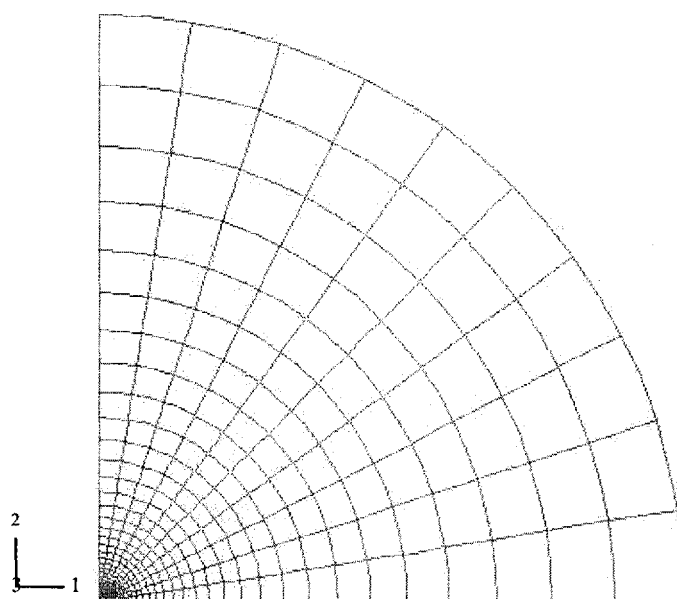
Figure 5.1 Finite element mesh for a spherical body.

5.1.1 Cavity instabilities in an infinite solid body with elastic/perfectly-plastic material

In this FEA simulation, the material is assumed to be elastic/perfectly-plastic where $E = 71$ GPa and $\varepsilon_y = 0.003$. Figure 5.2 illustrates the plot of cavity expansion versus load factor, σ_0/Y, for various Poisson's ratios. Figure 5.3

illustrates the plot of cavity expansion versus remote strain for various Poisson's ratios.

It was found that this FEA approach obtained an accurate solution in which the different between the FEA and analytical solutions (discussed in Section 3.1.1) is less than 1 percent. Furthermore, as ν increases, the remote stress for cavitation increases, while the remote strain decreases.
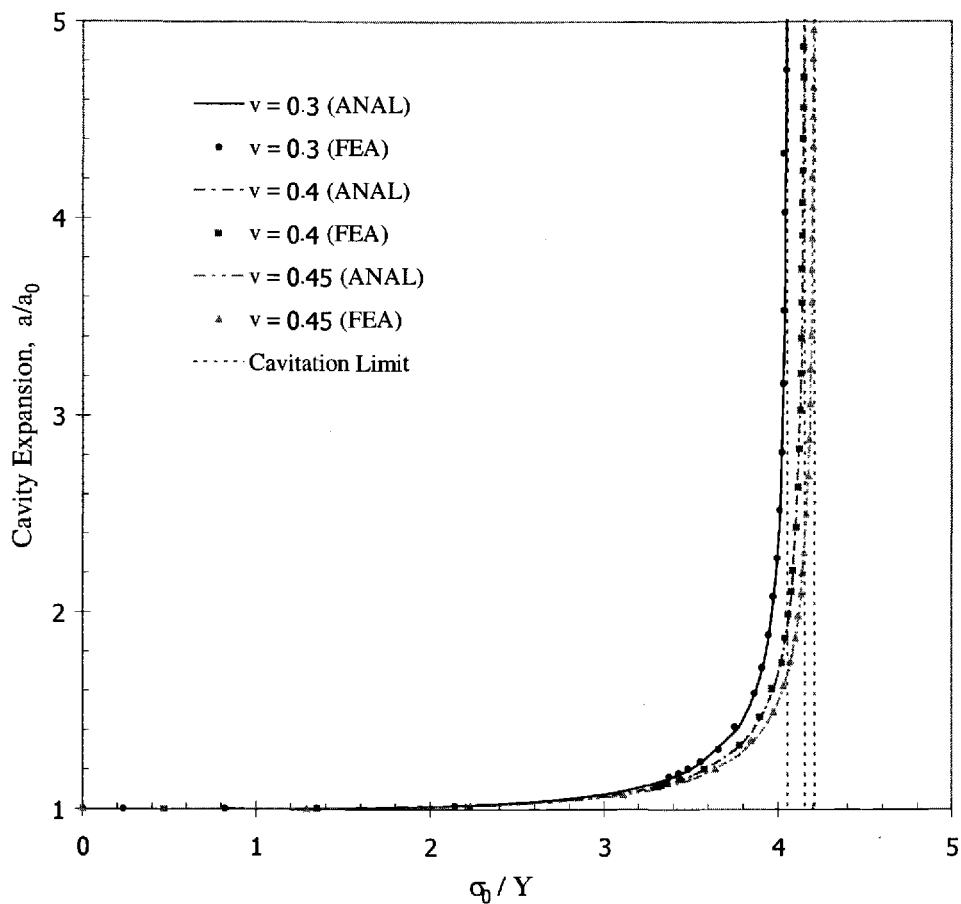

Figure 5.2 Cavity expansion vs. load factor, σ_0/Y, under spherically-symmetric loading with elastic/perfectly-plastic materials for various Poisson's ratios, ν. The analytical and finite element approaches are represented by ANAL and FEA respectively.
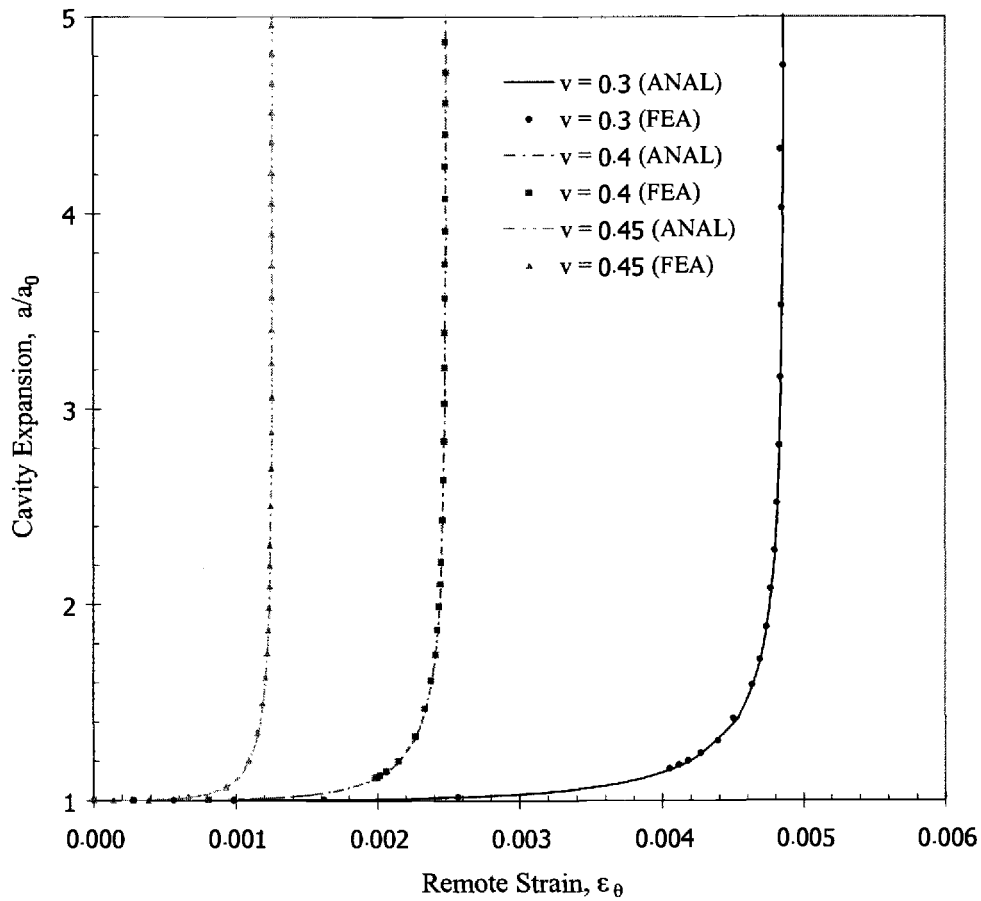
Figure 5.3 Cavity expansion vs. remote strain under spherically-symmetric loading with elastic/perfectly-plastic materials for various Poisson's ratios, v.

5.1.2 Cavity instabilities in an infinite solid body with linear hardening elastic-plastic material

In this FEA simulation, the material is assumed to be linear hardening elastic-plastic where $E = 71$ GPa, $\varepsilon_y = 0.003$, linear strain hardening coefficient, $m = 0.006$, and $\sigma = 213 + 428.57 \, \varepsilon^p$ MPa. Figure 5.4 illustrates the plot of true stress versus total strain. Figure 5.5 illustrates the plot of cavity expansion versus load

factor, σ_0/Y, for various Poisson's ratios. Figure 5.6 illustrates the plot of cavity expansion versus remote strain for various Poisson's ratios.

It was found that the FEA solution presented a saw-tooth pattern near the cavitation instability state for $v > 0.45$ which was an indication of numerical instabilities. Therefore, a FEA solution for $v > 0.45$ was not presented in these plots. Nonetheless, the cavitation limit stress obtained from the FEA approach (at $v = 0.45$) correlates well with the analytical solution obtained from equation (3.58) when $v = 0.5$ with the difference of 1.84 percent. Again, as v increases, σ_0 increases, while ε_θ decreases.
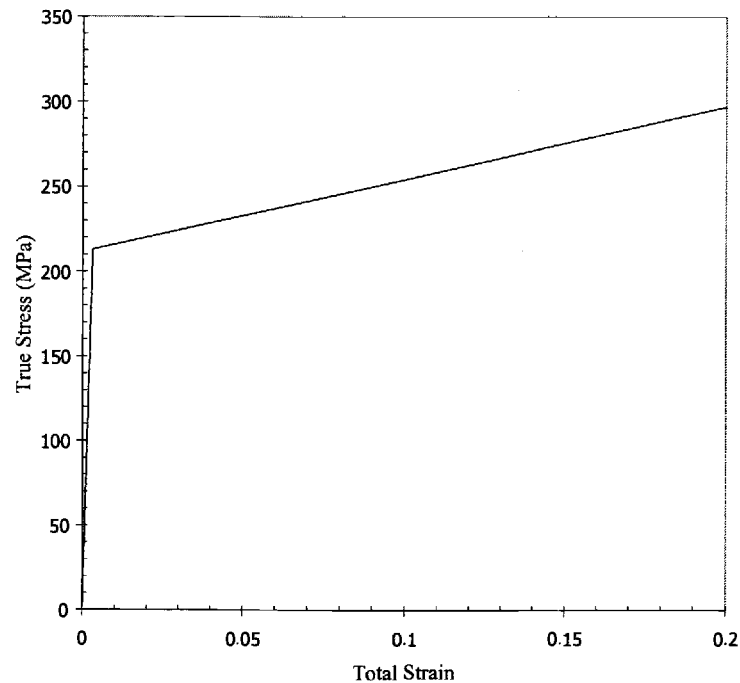

Figure 5.4 True stress vs. total strain for linear hardening elastic-plastic material: E = 71 GPa, ε_y = 0.003, and the linear strain-hardening coefficient, m = 0.006.
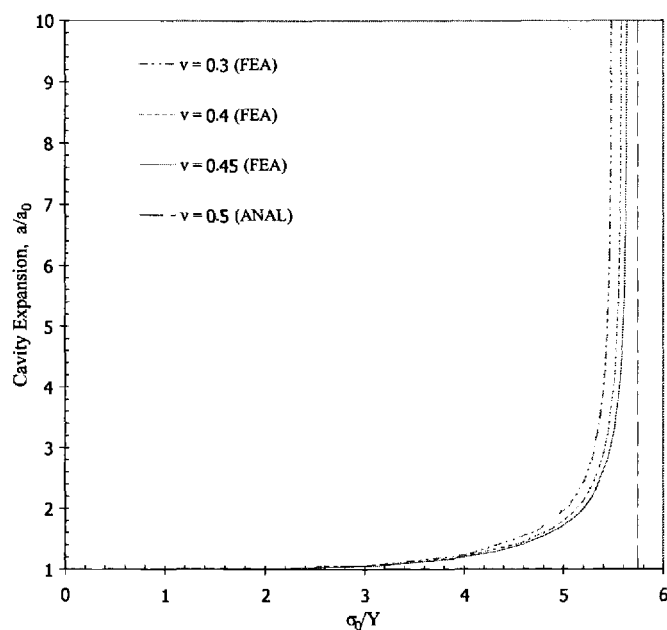
Figure 5.5 Cavity expansion vs. load factor, σ_0/Y, under spherically-symmetric loading with linear hardening elastic-plastic materials for various Poisson's ratios.
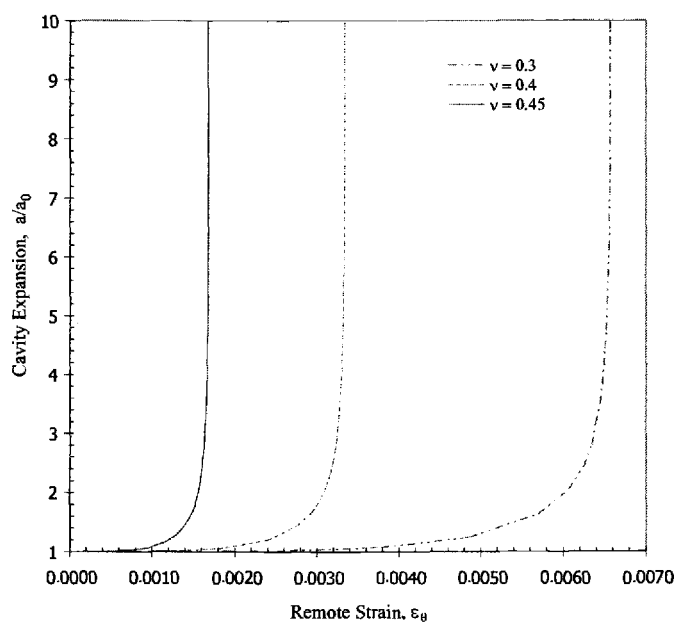

Figure 5.6 Cavity expansion vs. remote strain under spherically-symmetric loading with linear hardening elastic-plastic materials for various Poisson's ratios.

5.2 QUASI-STATIC ANALYSIS OF CAVITATION INSTABILITIES UNDER AXISYMMETRIC LOADING

A model of cavity expansion in a finite body subjected to remote axisymmetric loading was accomplished using the ABAQUS/Standard program. The finite element analysis provided both an arc-length solver and rezoning mesh capability. Here, the stress ratio, σ_2/σ_1, was keep fixed throughout a numerical analysis where σ_1 and σ_2 are the first and second principal stress respectively. Again, cavitation instability is assumed to occur when the slope between remote axial strain and cavity expansion becomes infinite as discussed in Section 3.1.1. The finite element mesh of a quarter-symmetry model was constructed using an eight-node, axisymmetric, quadrilateral element. Figure 5.10 illustrates a finite element mesh with $L/D = 15,000$.
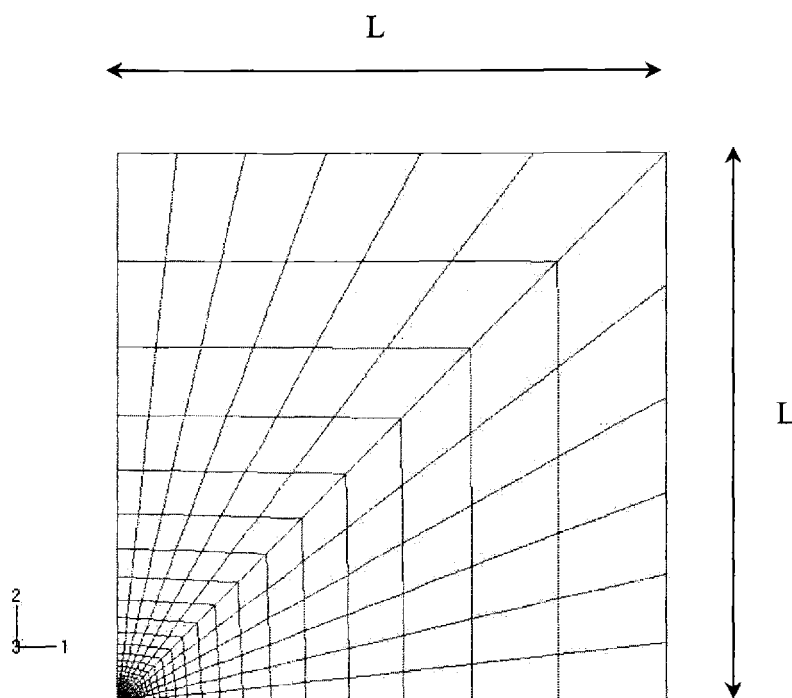

Figure 5.7 Finite element mesh for a cylindrical body.

5.2.1 Cavity instabilities in linear hardening elastic-plastic material

A single cavity in a finite body was simulated using a quarter-symmetry model of a body with $L/D = 15,000$ as illustrated in Figure 5.11. The finite element mesh consisted of 720 elements graded with a fine mesh near the cavity and a coarse mesh away from the cavity. However, the model size for the cases of σ_2/σ_1 = 1 and 0.9 was equal to 5,000. These model sizes appeared to be sufficiently large for representing a solution of a cavitation instability in an infinite body as discussed in Appendix C. The material is assumed to be linear hardening elastic-plastic solid: $E = 71$ GPa, $\varepsilon_y = 0.003$, and $v = 0.3$. The linear strain-hardening coefficients, m, are 0.1, 0.02, and 0.006, and $\sigma = 213 + 71 \times 10^3 \ [m/(1-m)] \ \varepsilon_p$ MPa.

Figure 5.8 illustrates true stress versus total strain for various the linear strain-hardening coefficients, m. Figure 5.9 illustrates cavity expansion versus remote axial strain at $\sigma_2/\sigma_1 = 1$ for various linear strain-hardening coefficients, m. Figure 5.10 illustrates cavity expansion versus remote axial stress at $\sigma_2/\sigma_1 = 1$ for various linear strain-hardening coefficients, m. Figure 5.11 illustrates cavity expansion versus remote axial strain at $m = 0.006$ for various stress ratios, σ_2/σ_1. Figure 5.12 illustrates cavity expansion versus remote axial at $m = 0.006$ for various stress ratios, σ_2/σ_1. Figure 5.13 illustrates the FEA predicted maximum principal stress for failure versus σ_2/σ_1 based on cavitation instabilities at $m = 0.006$. Figure 5.14 illustrates the FEA predicted cavity shapes a_0/a_{90} for failure versus σ_2/σ_1 based on cavitation instabilities at $m = 0.006$. Table 5.1 illustrates deformed meshes at the FEA predicted failure at $m = 0.006$ for $0.6 \leq \sigma_2/\sigma_1 \leq 1$.

It was found that as m increased, the remote axial strain and stress (at the FEA prediction of cavitation instability) increased. Furthermore, cavity expansion appeared to require large remote strain associated with instability when $\sigma_2/\sigma_1 < 0.8$, and the shape of cavity at instability depended on loading conditions (i.e., a value of stress ratio) as illustrated in Figure 5.14. For example, for $0.7 < \sigma_2/\sigma_1 < 0.8$, the shape of cavity was elliptic with the major axis along the 1-direction. There is

evidence (but inconclusive) of cavity instability occurring at $\sigma_2/\sigma_1 = 0.6$; however, the FEA simulation was found to be very difficult due to the warping of boundaries resulting from the large amount of plasticity in a remote field.
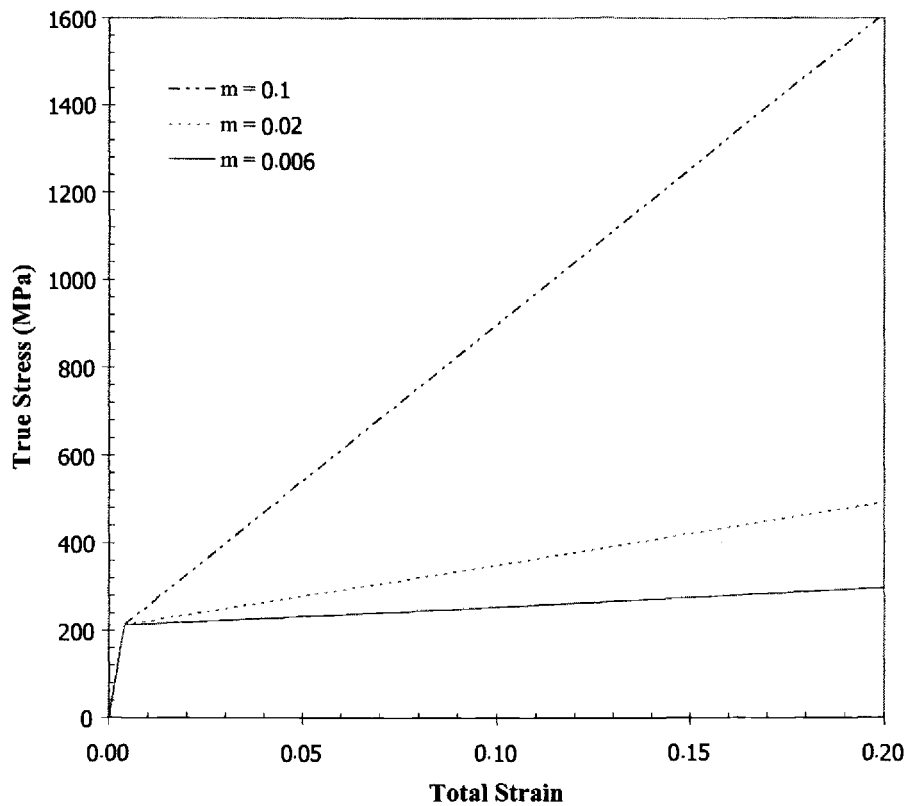

Figure 5.8 True stress vs. total strain for linear hardening elastic-plastic materials: $E = 71$ GPa, $\varepsilon_y = 0.003$, and $v = 0.3$. The linear strain-hardening coefficient is m and $m = 0.1$, 0.02, and 0.006 respectively.
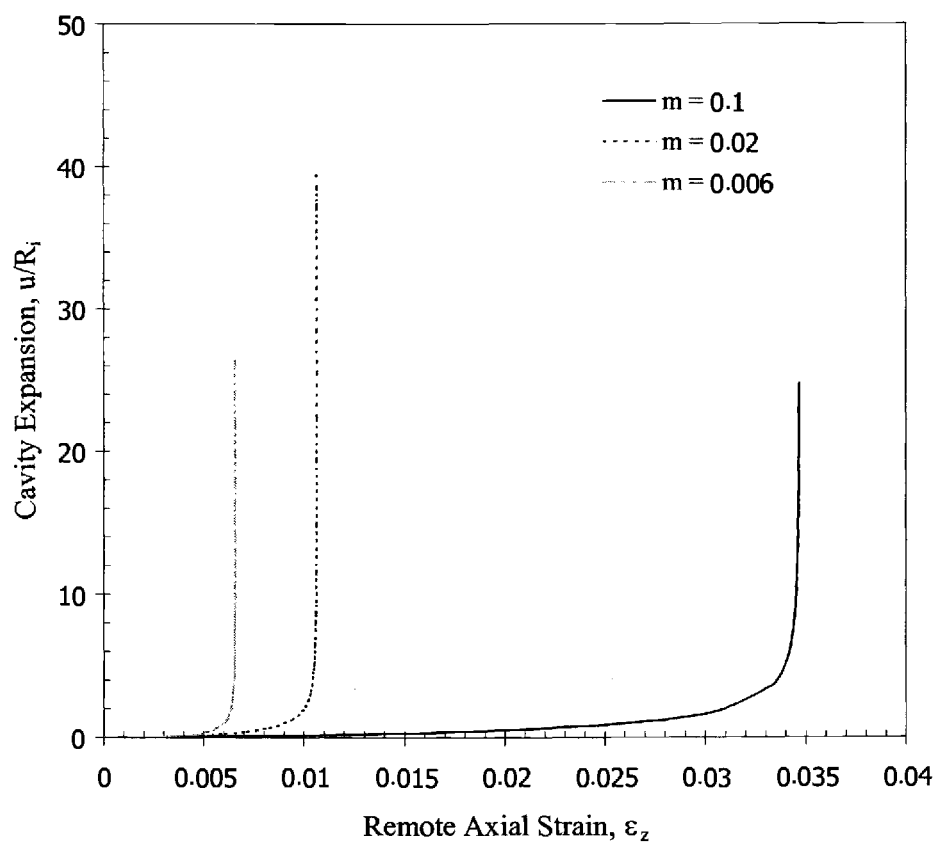
Figure 5.9 Cavity expansion vs. remote axial strain under axisymmetric loading at $\sigma_2/\sigma_1 = 1$ for various linear strain-hardening coefficients, $m = 0.1$, 0.02, and 0.006 respectively.
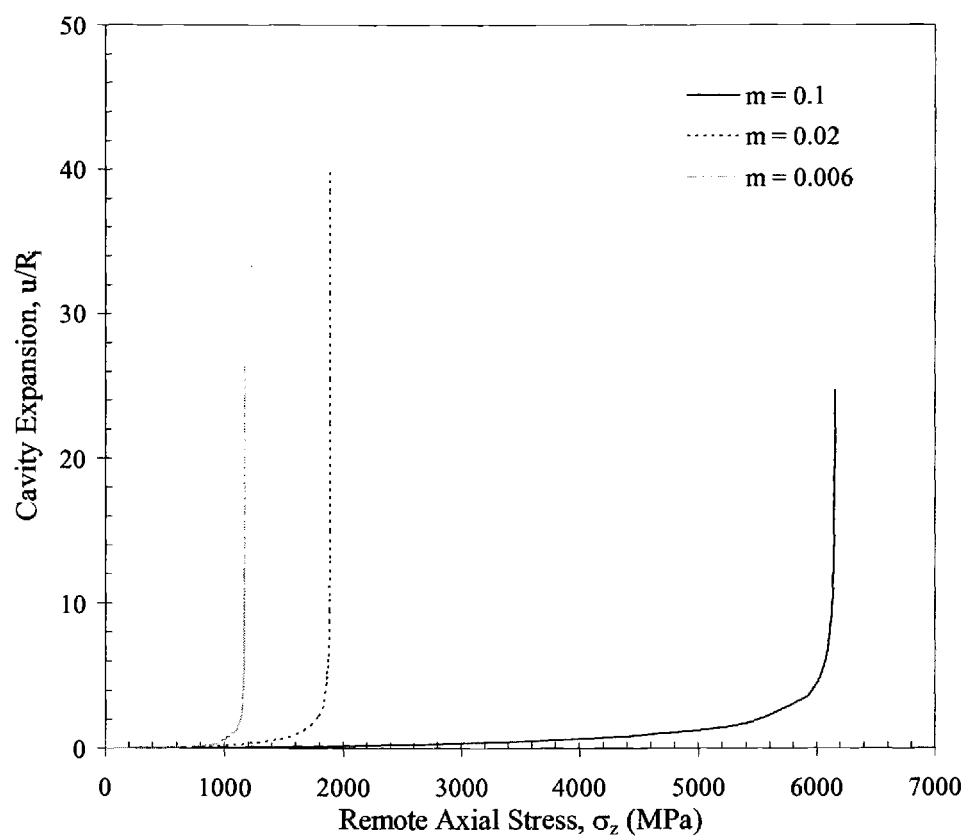
Figure 5.10 Cavity expansion vs. remote axial stress under axisymmetric loading at $\sigma_2/\sigma_1 = 1$ for various linear strain-hardening coefficients, $m = 0.1, 0.02,$ and 0.006 respectively

(a)
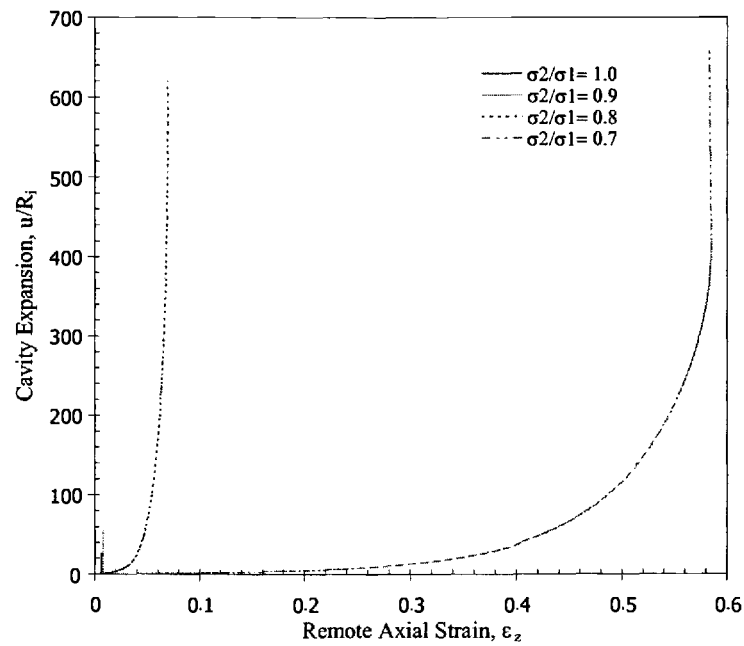

(b)

Figure 5.11 Cavity expansion vs. remote axial strain under axisymmetric loading at the linear strain-hardening coefficient, $m = 0.006$, for (a) $0.7 \leq \sigma_2/\sigma_1 \leq 1$ and (b) $\sigma_2/\sigma_1 = 0.65$ and 0.6.
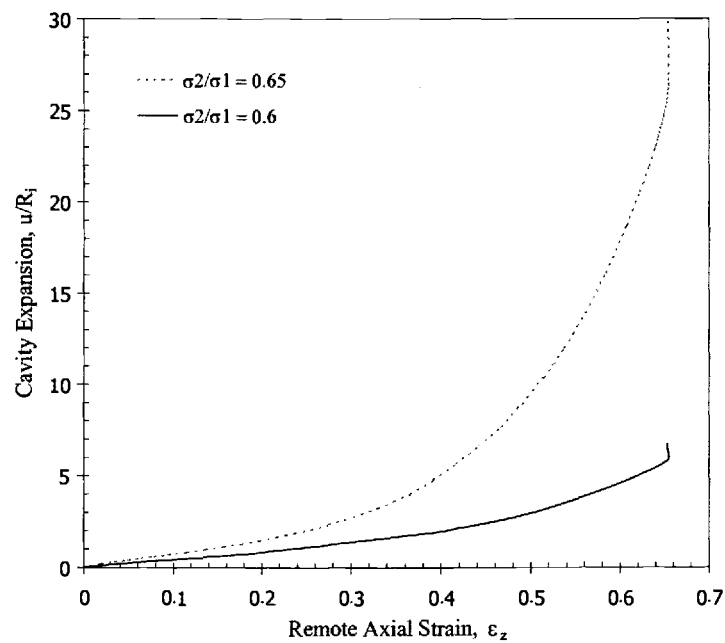
(a)

(b)

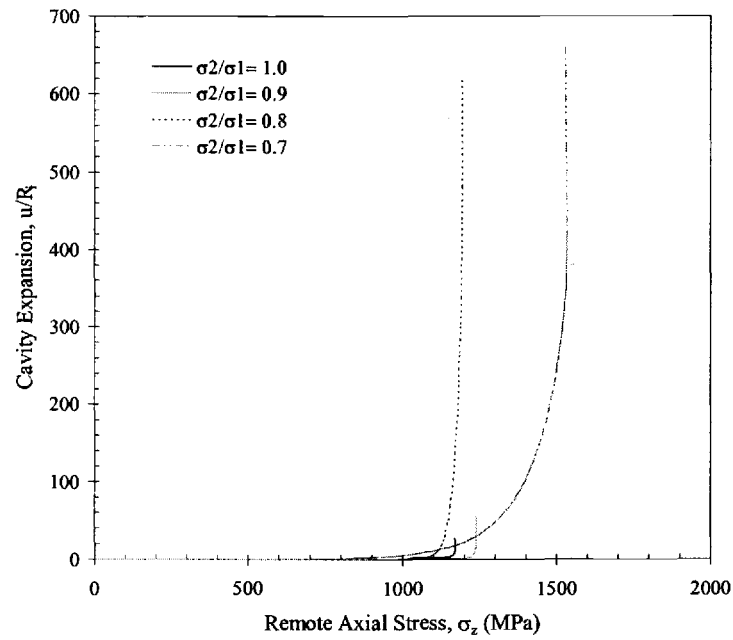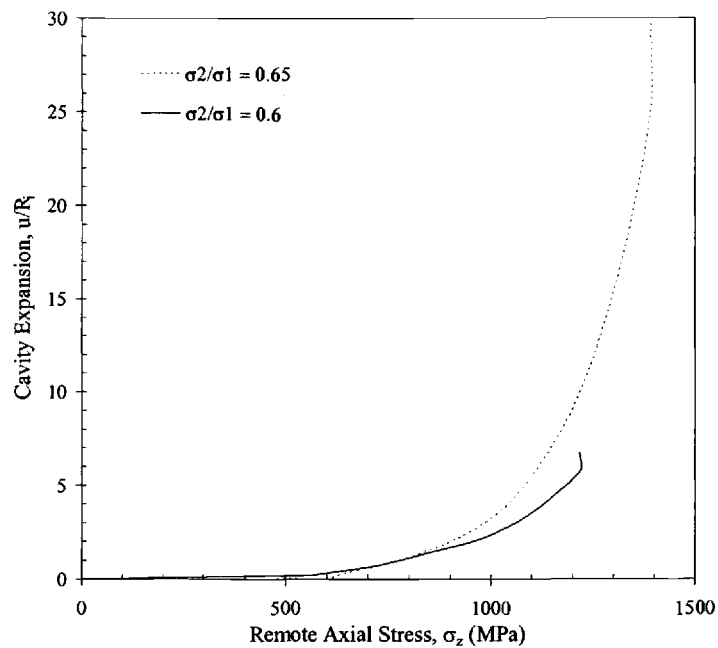Figure 5.12 Cavity expansion vs. remote axial stress under axisymmetric loading at the linear strain-hardening coefficient, m = 0.006, for (a) 0.7 $\leq \sigma_2/\sigma_1 \leq$ 1 and (b) σ_2/σ_1 = 0.65 and 0.6.
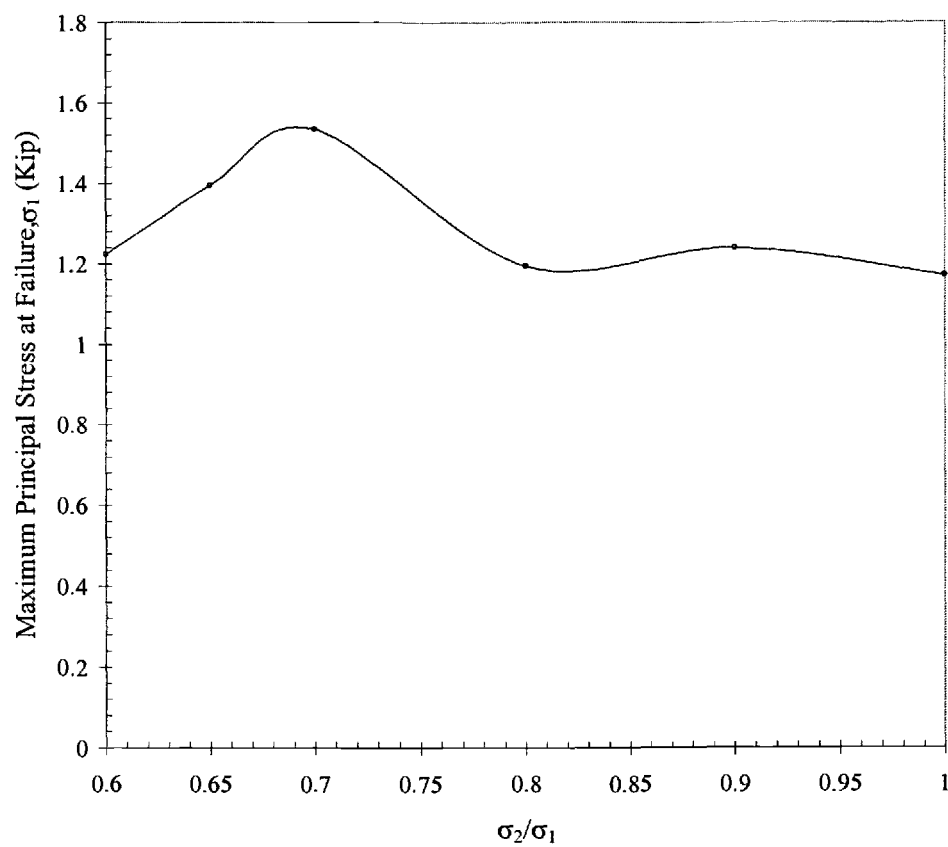
Figure 5.13 The FEA predicted maximum principal stress for failure vs. σ_2/σ_1 based on cavitation instabilities in linear hardening elastic-plastic material ($m = 0.006$).
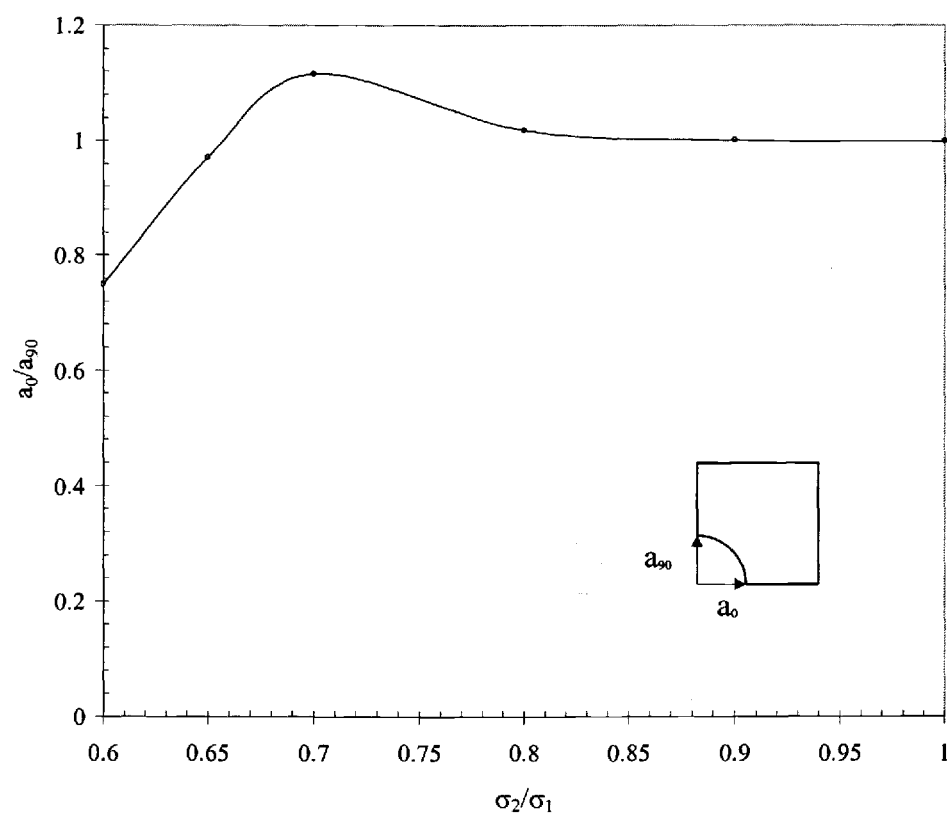
Figure 5.14 The FEA predicted cavity shapes a_0/a_{90} for failure vs. σ_2/σ_1 based on cavitation instabilities in linear hardening elastic-plastic material ($m = 0.006$).

Table 5.1 Deformed meshes at the FEA predicted failure on linear hardening elastic-plastic material ($m = 0.006$) for $0.6 \leq \sigma_2/\sigma_1 \leq 1$.
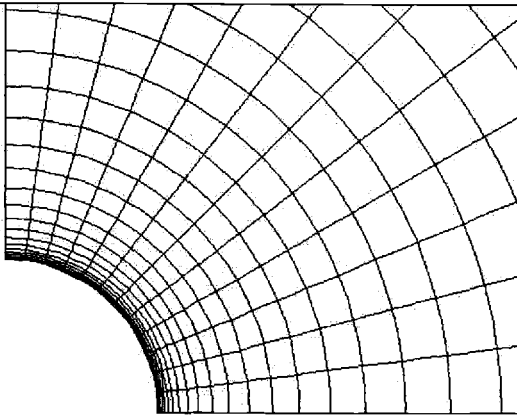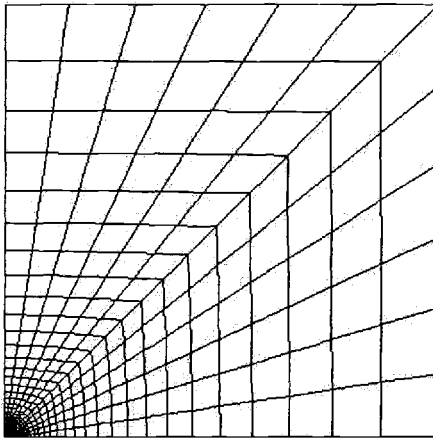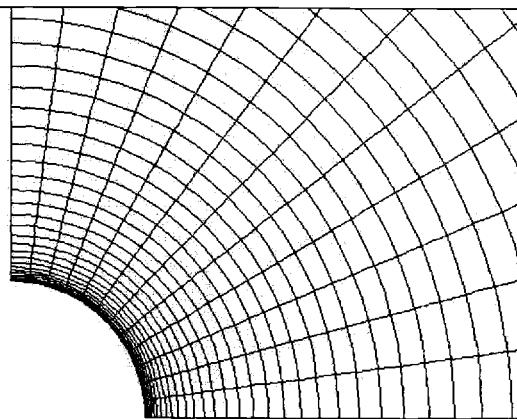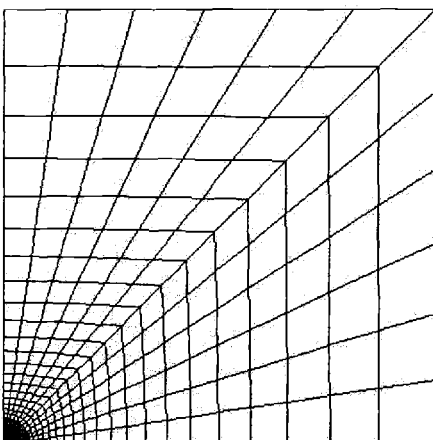
σ_2/σ_1	Cavity Shape	Deformed Body
1		
0.9		

Table 5.1 Deformed meshes at the FEA predicted failure on linear hardening elastic-plastic material ($m = 0.006$) for $0.6 \leq \sigma_2/\sigma_1 \leq 1$ (Continued).
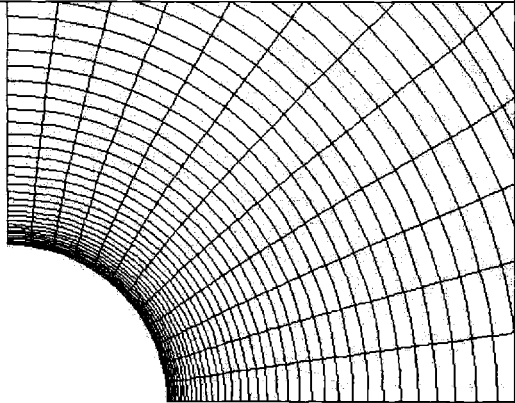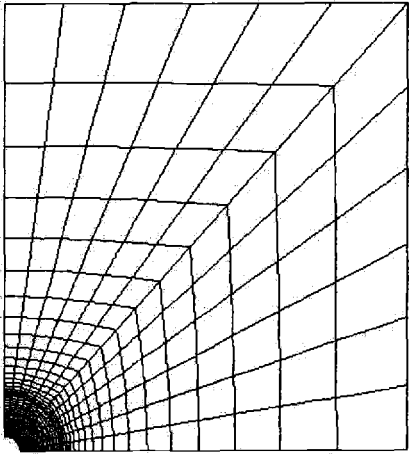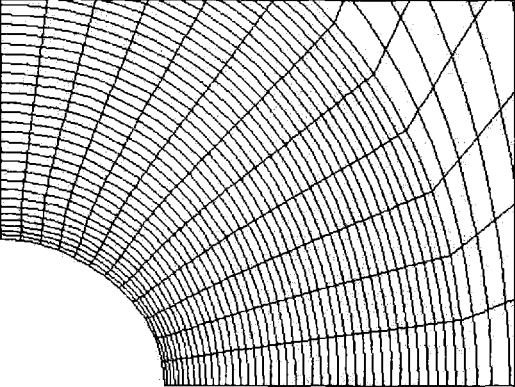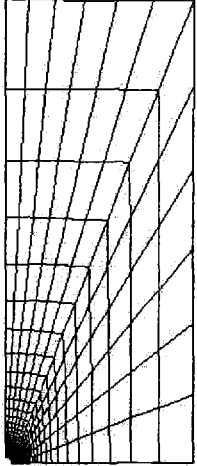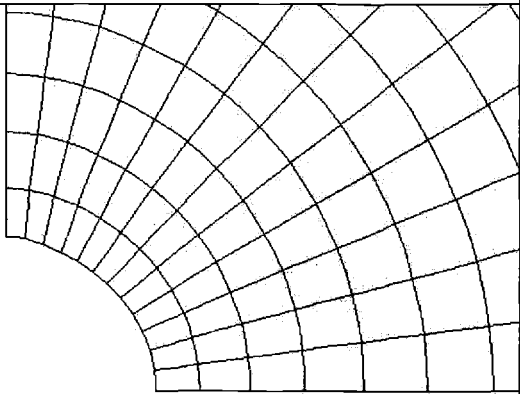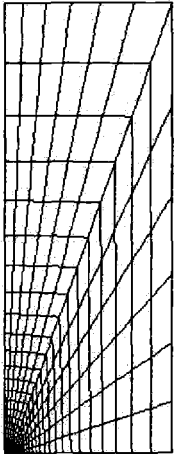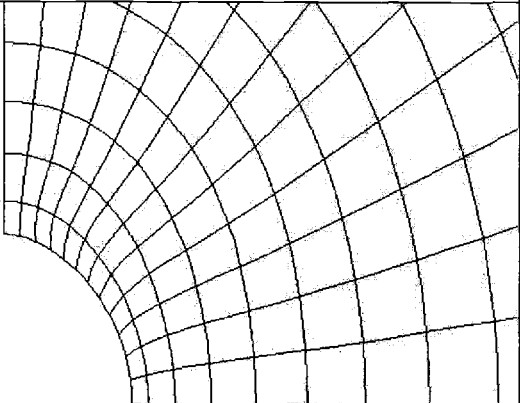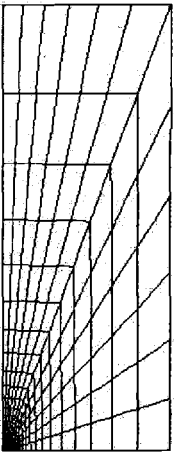
σ_2/σ_1	Cavity Shape	Deformed Body
0.8		
0.7		

Table 5.1 Deformed mesh at the FEA predicted failure on linear hardening
elastic-plastic material ($m = 0.006$) for $0.6 \leq \sigma_2/\sigma_1 \leq 1$ (Continued).

σ_2/σ_1	Cavity Shape	Deformed Body
0.65		
0.6		

5.2.2 Cavity instabilities in power hardening elastic-plastic material

A single cavity in a finite body was simulated using a quarter-symmetry, axisymmetric model of a body with the model size being equal to 15,000 as illustrated in Figure 5.10. The finite element mesh consisted of 720 elements

graded with a fine mesh near the cavity and a coarse mesh away from the cavity. However, the model size for $\sigma_2/\sigma_1 = 1$ and 0.9 was equal to 5,000. These model sizes appeared to be sufficiently large for representing a solution of a cavitation instability in an infinite body. The material is assumed to be power hardening elastic-plastic solid: $E = 71$ GPa, $\varepsilon_y = 0.003$, $v = 0.45$, strain-hardening exponent, $n = 0.25$, and $\sigma = \text{sign} (\varepsilon) \, 213 \times 10^6 (|\varepsilon|/0.003)^{0.25}$ when $|\varepsilon| > 0.003$.

Figure 5.15 illustrates true stress versus total strain for power strain-hardening material. Figure 5.16 illustrates cavity expansion versus remote axial strain for various stress ratios. Figure 5.17 illustrates cavity expansion versus remote axial stress for various stress ratios. Figure 5.18 illustrates a comparison of cavitation curves obtained from the FEA method with the approximate solution presented by Hou and Abeyartne (1992) for a case of an incompressible solid. Figure 5.19 illustrates the FEA predicted cavity shapes a_0/a_{90} for failure versus σ_2/σ_1 based on cavitation instabilities. Table 5.2 illustrates deformed meshes at the FEA predicted failure for $0.4 \leq \sigma_2/\sigma_1 \leq 1$.

It was found that a cavity expansion appeared to require large remote strain associated with instability when $\sigma_2/\sigma_1 < 0.8$, and the shape of cavity at instability depended on loading conditions as illustrated in Figure 5.19. There is evidence (but inconclusive) of cavitation instability occurring at $\sigma_2/\sigma_1 = 0.4$; however, FEA simulation was found to be very difficult due to the warping of boundaries resulting from the large amount of plasticity in the remote field. The FEA prediction of cavitation limit stresses for various stress ratios were compared with those of Hou and Abeyartne (1992) as illustrated in Figure 5.19. We found that both solutions correlated well only if the cavitation instability occurs before yielding of the remote field.
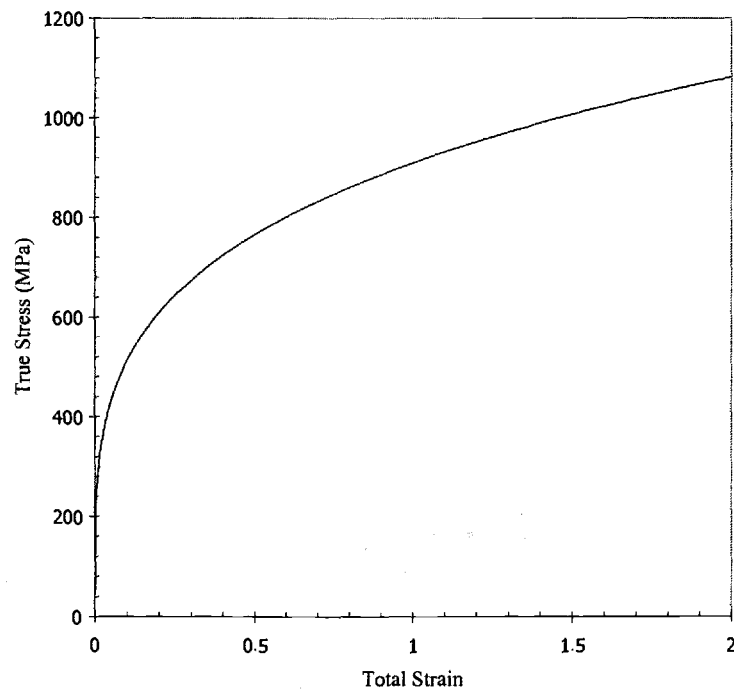
Figure 5.15 True stress vs. total strain for power hardening elastic-plastic material: $E = 71$ GPa, $\varepsilon_y = 0.003$, $v = 0.45$, and the strain-hardening exponent, $n = 0.25$.

(a)
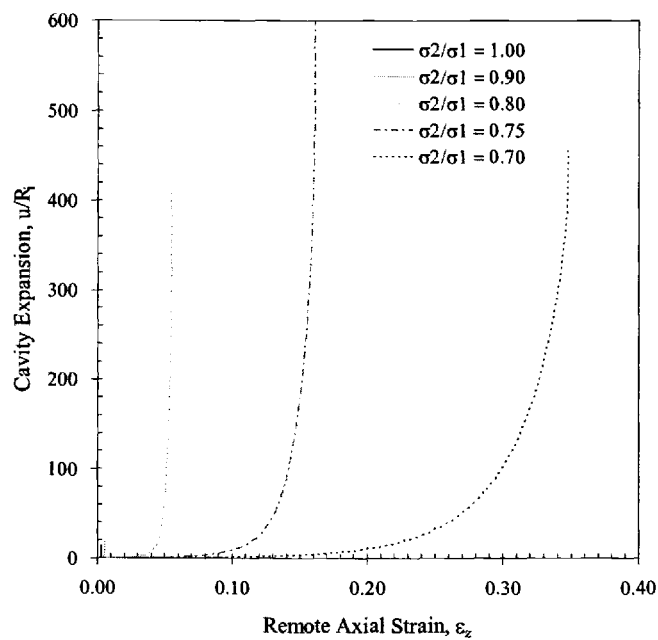
(b)
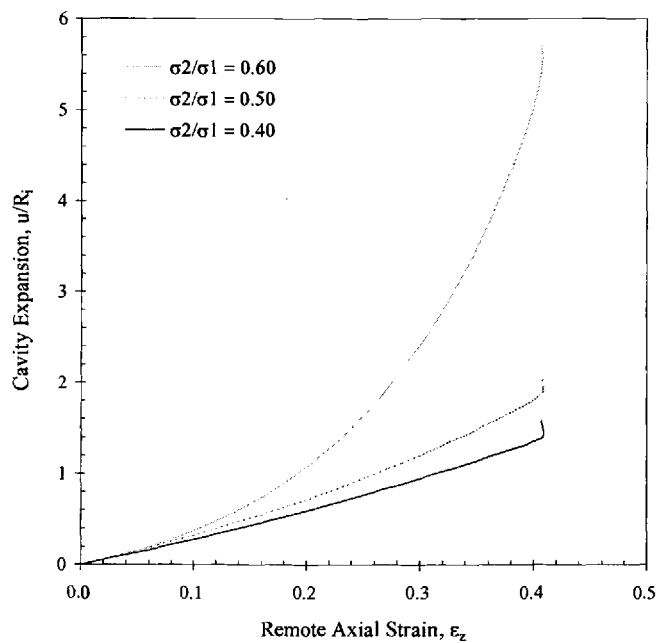
Figure 5.16 Cavity expansion vs. remote axial strain under axisymmetric loading at the stain hardening exponent, $n = 0.25$, for (a) $0.7 \leq \sigma_2/\sigma_1 \leq 1$ and (b) $0.4 \leq \sigma_2/\sigma_1 \leq 0.6$.

(a)
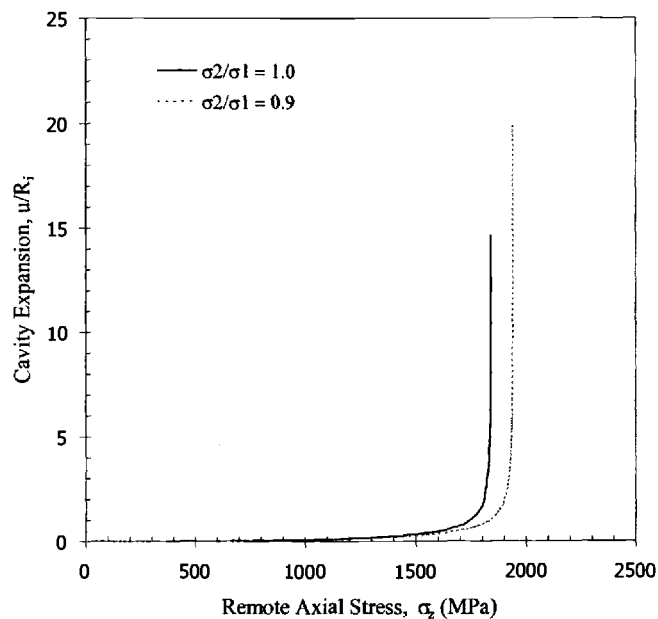
(b)
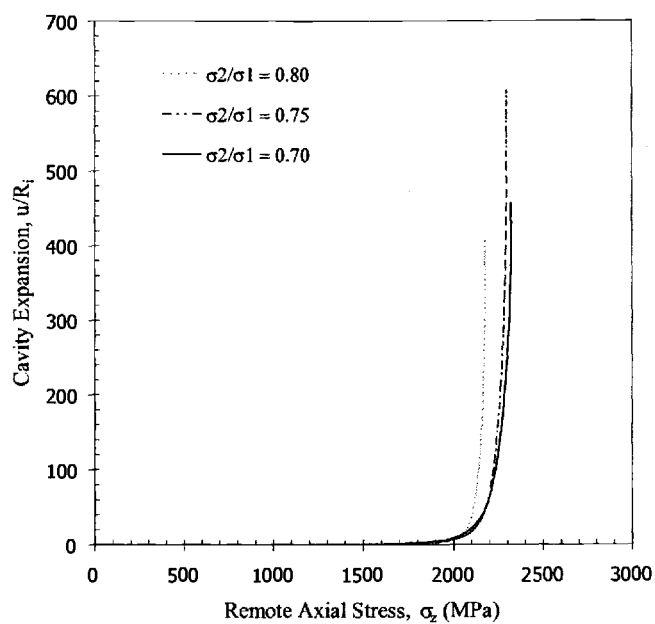
Figure 5.17 Cavity expansion vs. remote axial stress under axisymmetric loading at the strain-hardening exponent, $n = 0.25$, for (a) $0.9 \leq \sigma_2/\sigma_1 \leq 1$ and (b) $0.7 \leq \sigma_2/\sigma_1 \leq 0.8$
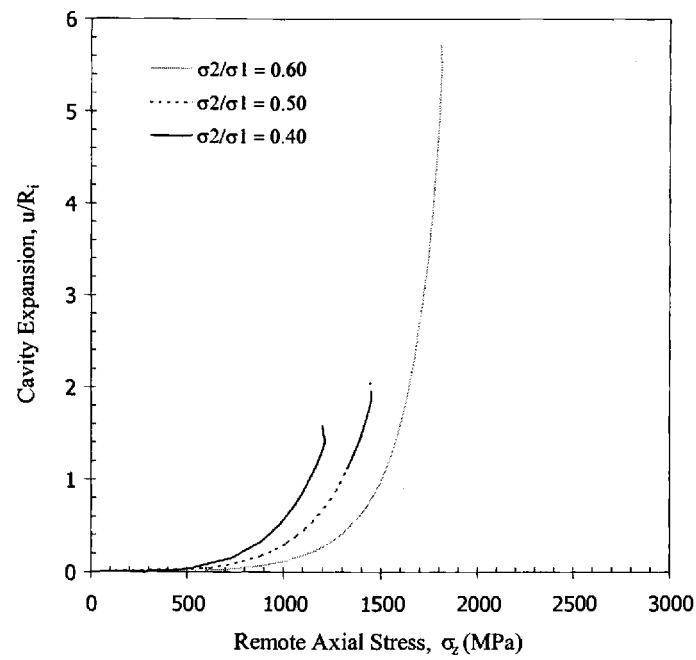
Figure 5.17c Cavity expansion vs. remote axial stress under axisymmetric loading at the strain-hardening exponent, $n = 0.25$, for $0.4 \leq \sigma_2/\sigma_1 \leq 0.6$.
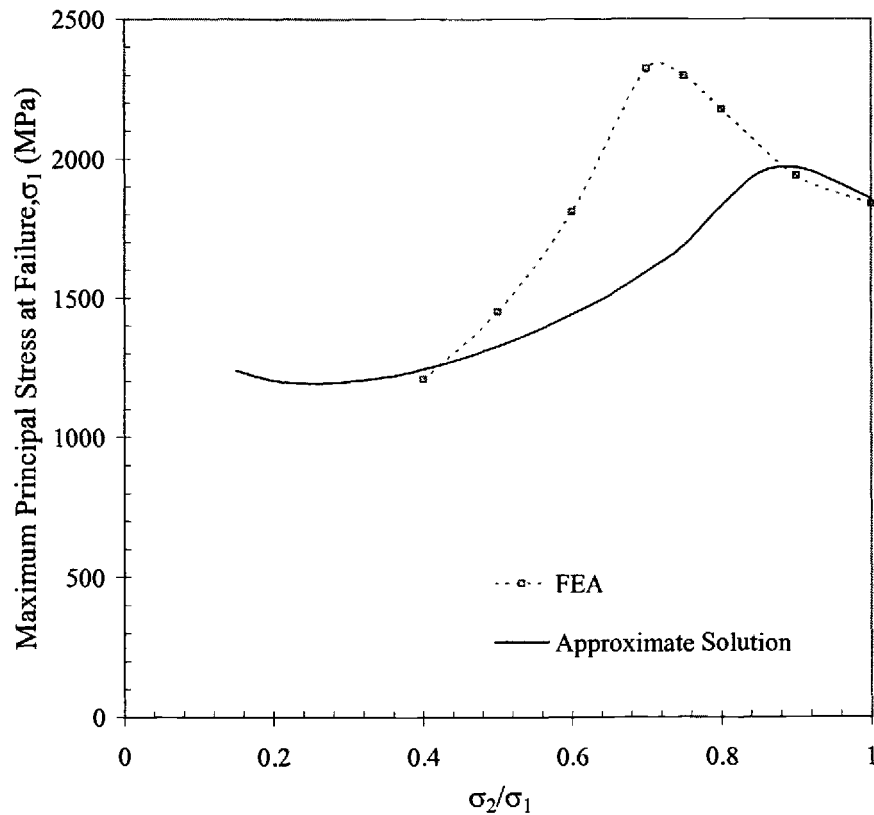
Figure 5.18 Comparison of cavitation curves obtained from FEA with the approximate solution (Hou and Abeyartne, 1992) for the case of an incompressible solid. The FEA predicted maximum principal stress for failure vs. σ_2/σ_1 based on cavitation instabilities in power hardening elastic-plastic material ($\varepsilon_y = 0.003$ and $n = 0.25$).
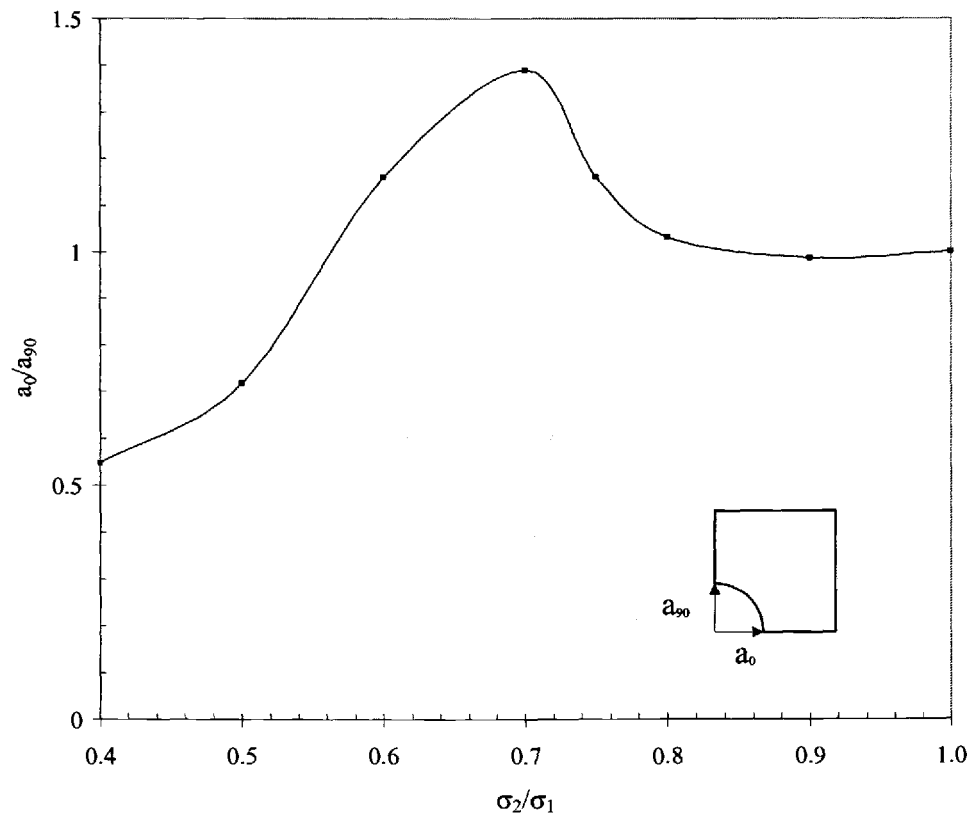
Figure 5.19 The FEA predicted cavity shapes a_0/a_{90} for failure vs. σ_2/σ_1 based on cavitation instabilities in power hardening elastic-plastic material ($\varepsilon_y = 0.003$ and $n = 0.25$).

Table 5.2 Deformed meshes at the FEA predicted failure on power strain-hardening material ($\varepsilon_y = 0.003$ and $n = 0.25$) for $0.4 \leq \sigma_2/\sigma_1 \leq 1$.
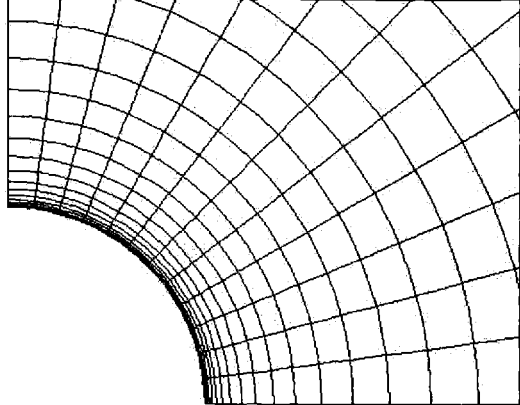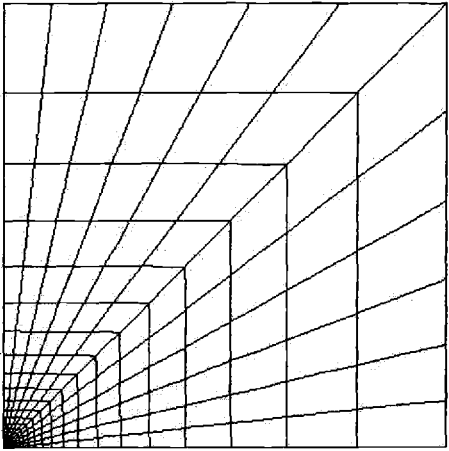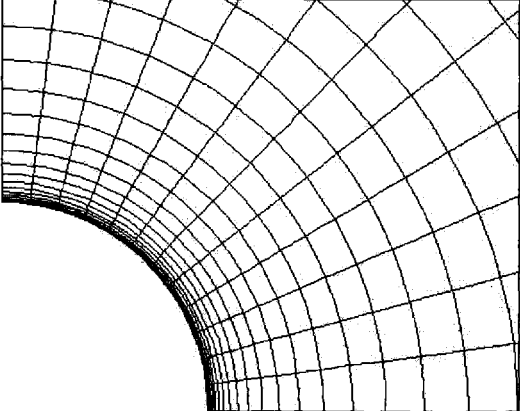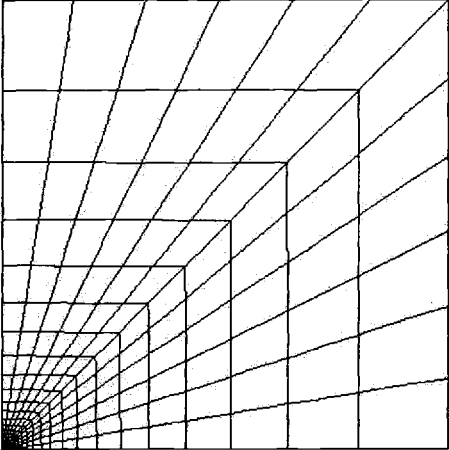
σ_2/σ_1	Cavity Shape	Deformed Body
1		
0.9		

Table 5.2 Deformed meshes at the FEA predicted failure on power strain-hardening material ($\varepsilon_y = 0.003$ and $n = 0.25$) for $0.4 \leq \sigma_2/\sigma_1 \leq 1$ (Continued)
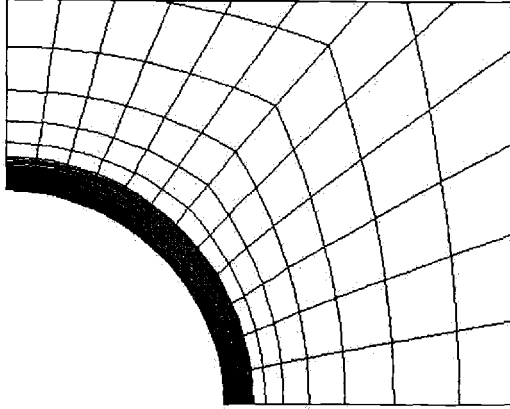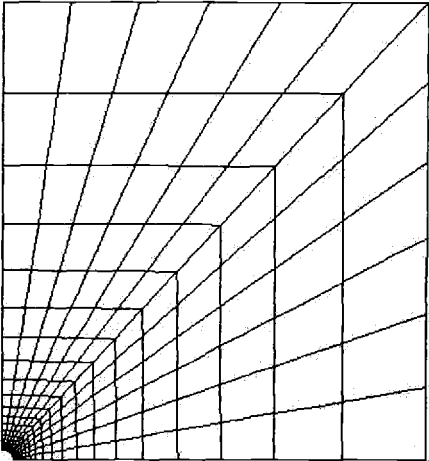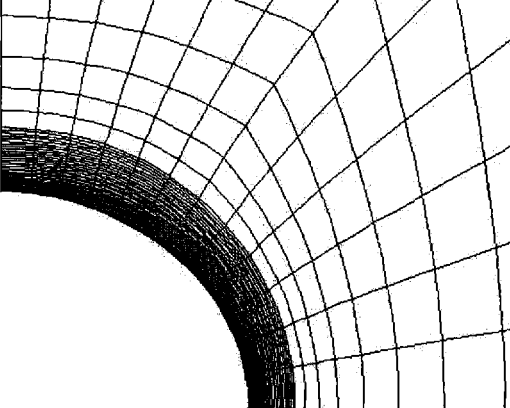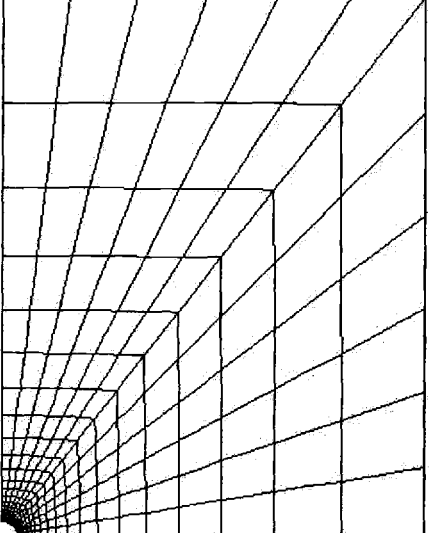
σ_2/σ_1	Cavity Shape	Deformed Body
0.8		
0.75		

Table 5.2 Deformed meshes at the FEA predicted failure on power strain-hardening material ($\varepsilon_y = 0.003$ and $n = 0.25$) for $0.4 \leq \sigma_2/\sigma_1 \leq 1$ (Continued)
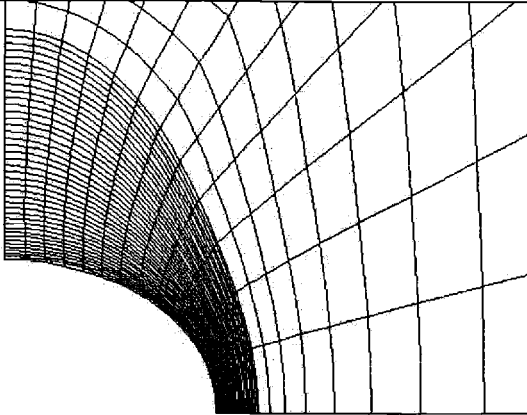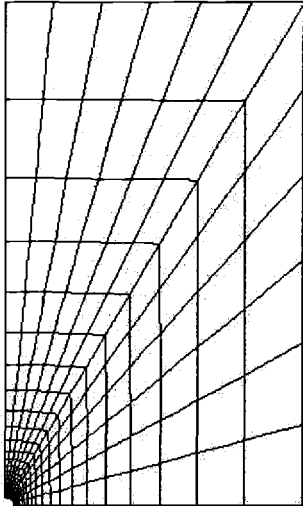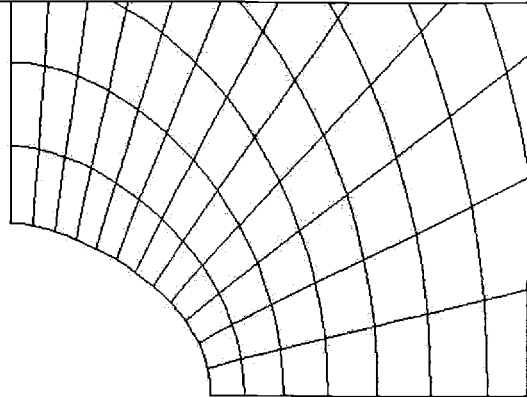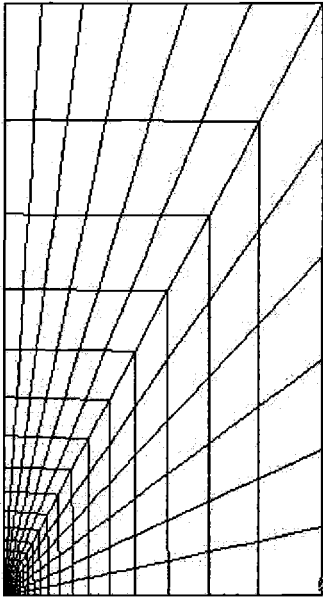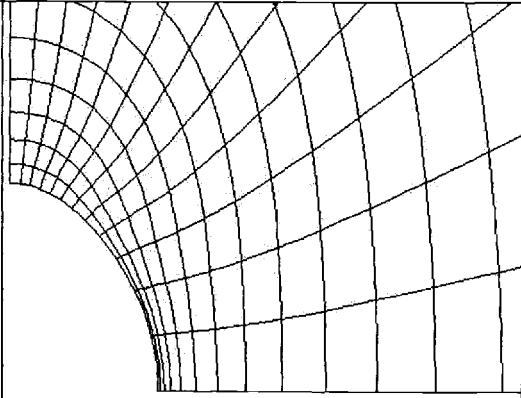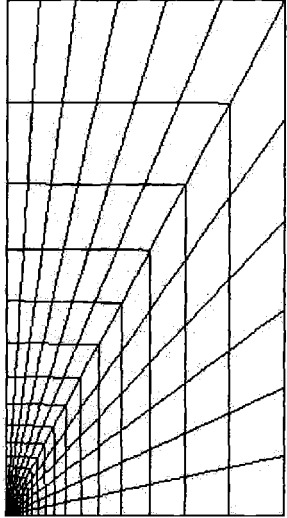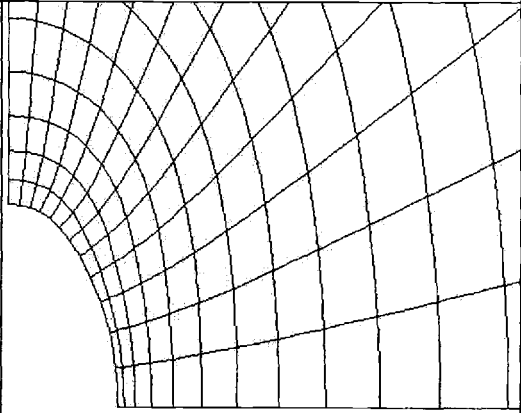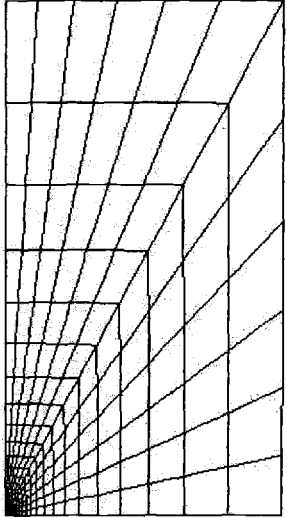
σ_2/σ_1	Cavity Shape	Deformed Body
0.7		
0.6		

Table 5.2 Deformed meshes at the FEA predicted failure on power strain-hardening material ($\varepsilon_y = 0.003$ and $n = 0.25$) for $0.4 \leq \sigma_2/\sigma_1 \leq 1$ (Continued).

σ_2/σ_1	Cavity Shape	Deformed Body
0.5		
0.4		

5.2.3 Cavity instabilities in constrained thin silver films

A single cavity in a finite body was simulated using a quarter-symmetric model. In each loading case, the model size was obtained from the FEA solutions presented in Appendix C in such a way that it could represent a solution of a cavitation instability in an infinite body. The material was constrained silver: $E = 71$ GPa, $Y = 49.7$ MPa, and $v = 0.37$.

Figure 5.20 illustrates true stress versus total strain of constrained silver. Figure 5.21 illustrates cavity expansion versus remote axial strain for various stress ratios. Figure 5.22 illustrates cavity expansion versus remote axial stress for various stress ratios. Figure 5.23 illustrates the FEA predicted maximum principal stress for failure versus σ_2/σ_1 based on cavitation instabilities. Figure 5.24 illustrates the FEA predicted cavity shapes a_0/a_{90} for failure versus σ_2/σ_1 based on cavitation instabilities. Table 5.3 illustrates deformed meshes at the FEA predicted failure for $0.5 \leq \sigma_2/\sigma_1 \leq 1$.

It was found that cavity expansion appeared to require large remote strains associated with instability when $\sigma_2/\sigma_1 < 0.75$, and the shape of cavity at instability depended on the loading condition as illustrated in Figure 5.24. There is evidence (but inconclusive) of cavitation instability occurring at $\sigma_2/\sigma_1 = 0.5$; however, again, the FEA simulation was found to be very difficult due to the warping of boundaries resulting from the large amount of plasticity in the remote field. Values of caviation limit stress obtained from the finite element analysis were compared with those from experiments result by Kansser et al. (1998). We found that both results correlated well except at $\sigma_2/\sigma_1 = 0.76$.
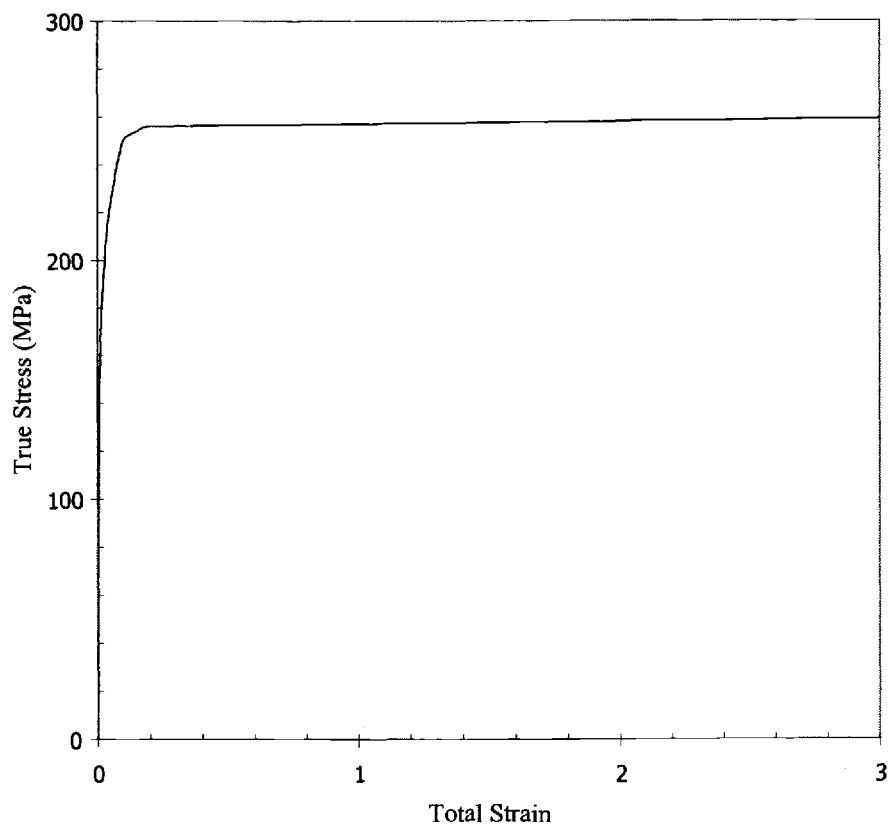
Figure 5.20 True stress vs. total strain of constrained silver: $E = 71$ GPa, $Y = 49.7$ MPa, and $v = 0.37$.

(a)
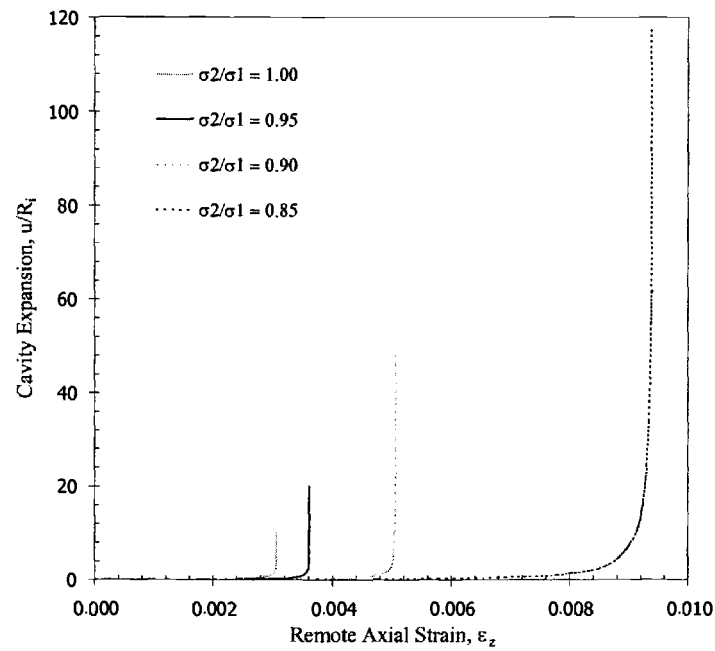
(b)
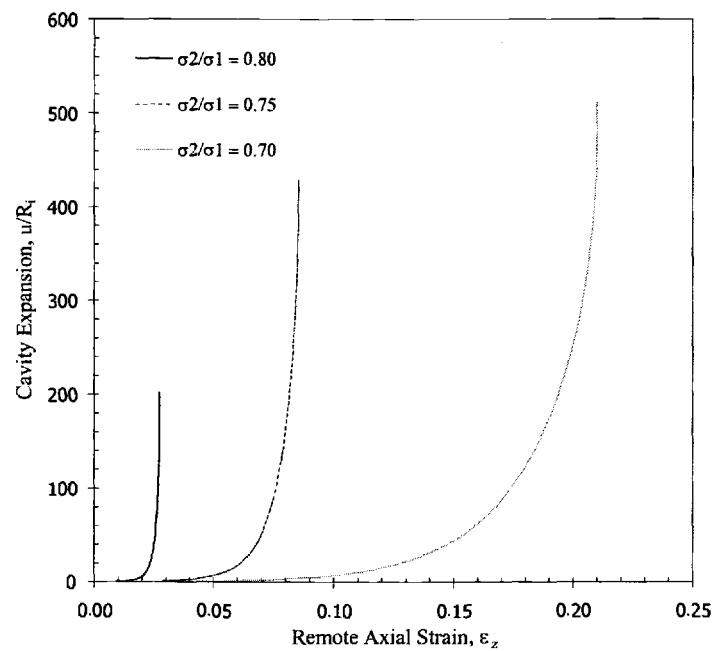
Figure 5.21 Cavity expansion vs. remote axial strain under axisymmetric loading with constrained silver for (a) $0.85 \leq \sigma_2/\sigma_1 \leq 1$ and (b) $0.7 \leq \sigma_2/\sigma_1 \leq 0.8$.
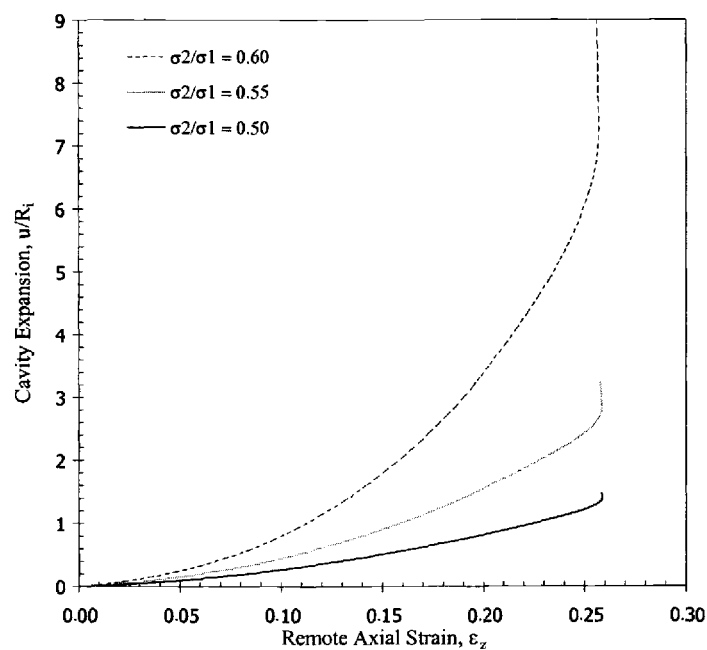
Figure 5.21c Cavity expansion vs. remote axial strain under axisymmetric loading with constrained silver for $0.5 \leq \sigma_2/\sigma_1 \leq 0.6$.

(a)
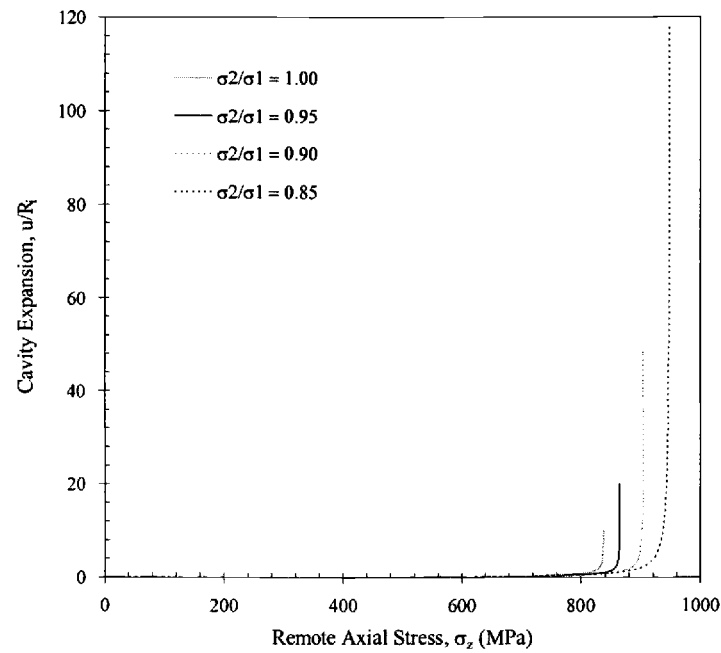
(b)
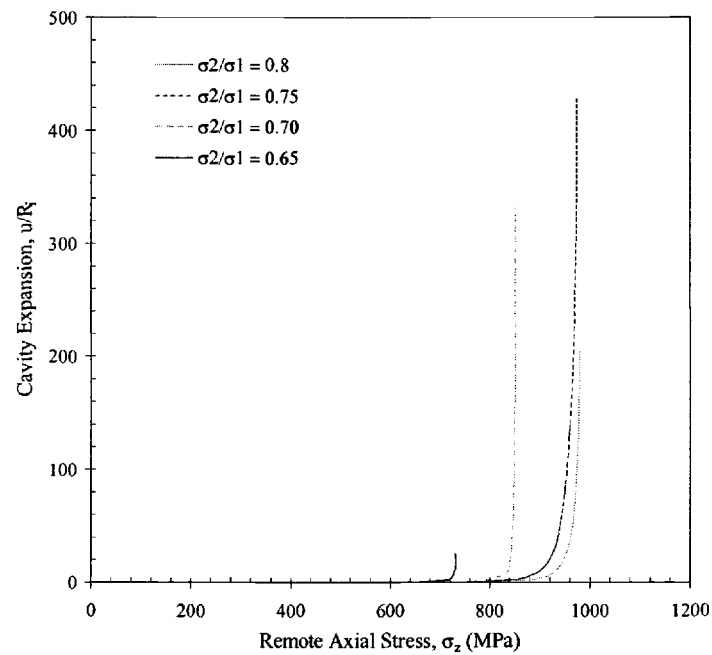
Figure 5.22 Cavity expansion vs. remote axial stress under axisymmetric loading with constrained silver for (a) $0.85 \leq \sigma_2/\sigma_1 \leq 1$ and (b) $0.8 \leq \sigma_2/\sigma_1 \leq 0.65$.
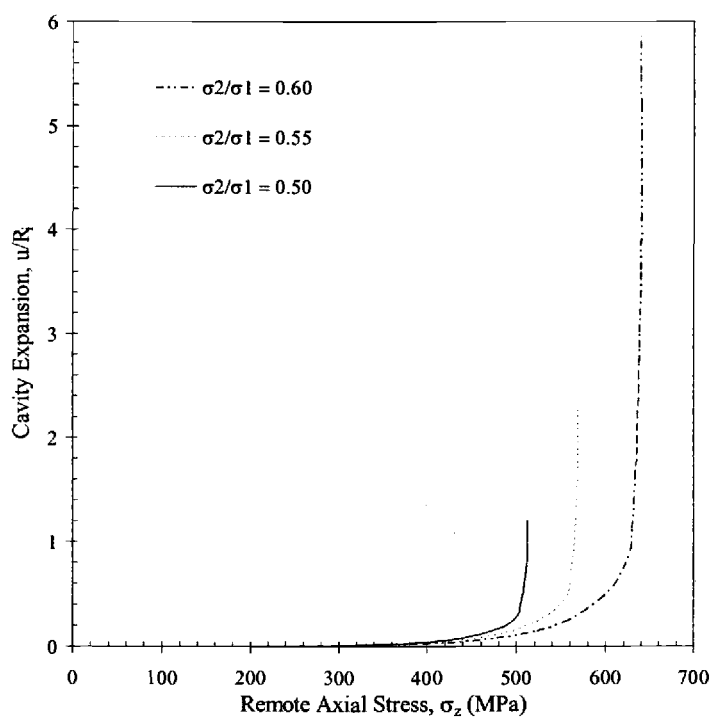
Figure 5.22c Cavity expansion vs. remote axial stress under axisymmetric loading with constrained silver for $0.5 \leq \sigma_2/\sigma_1 \leq 0.6$.
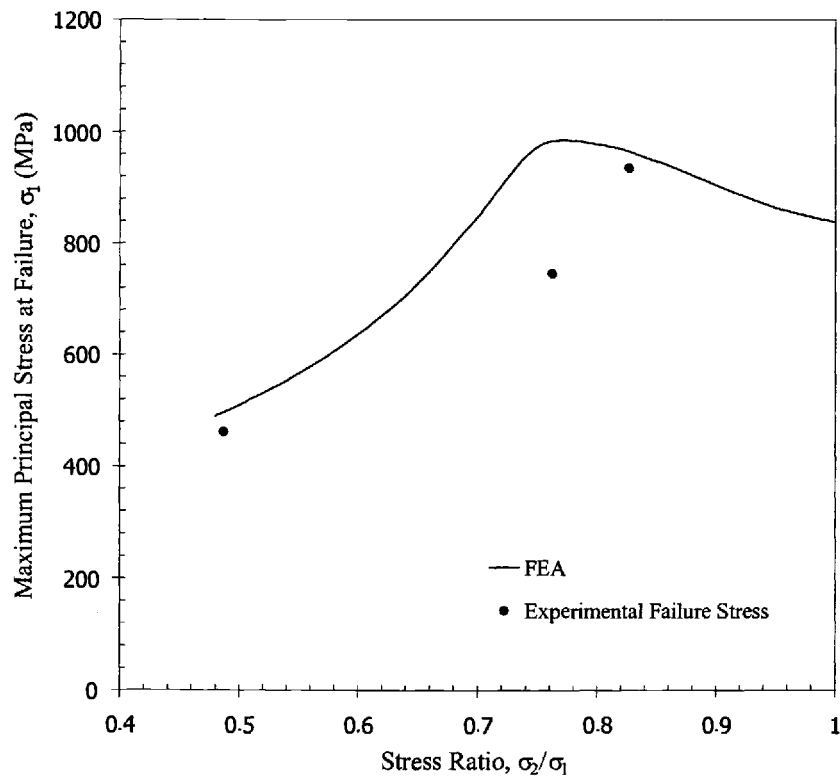
Figure 5.23 The FEA predicted maximum principal stress for failure vs. σ_2/σ_1 based on cavitation instabilities in constrained silver.
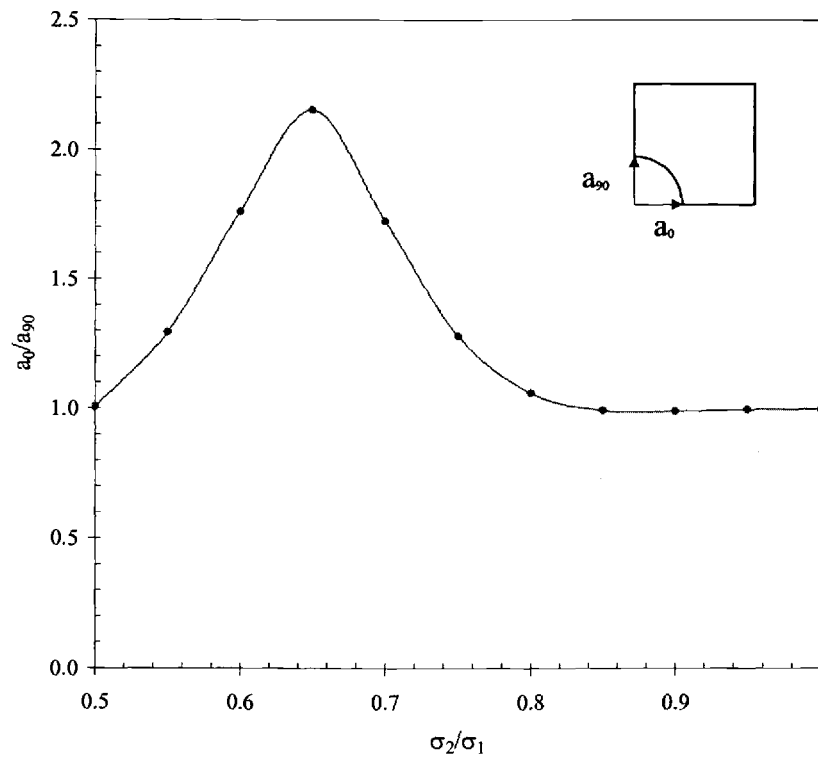
Figure 5.24 The FEA predicted cavity shapes a_0/a_{90} for failure vs. σ_2/σ_1 based on cavitation instabilities in constrained silver.

Table 5.3 Deformed meshes at the FEA predicted failure on constrained silver
for $0.5 \leq \sigma_2/\sigma_1 \leq 1$.
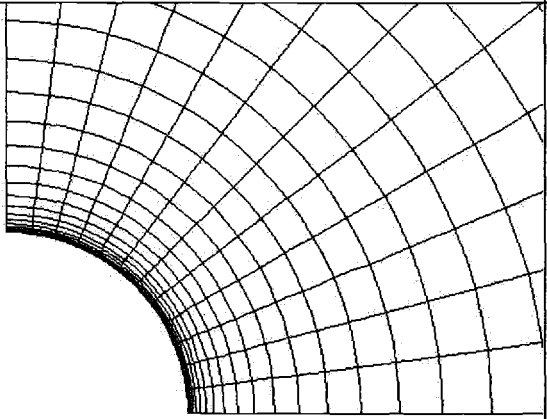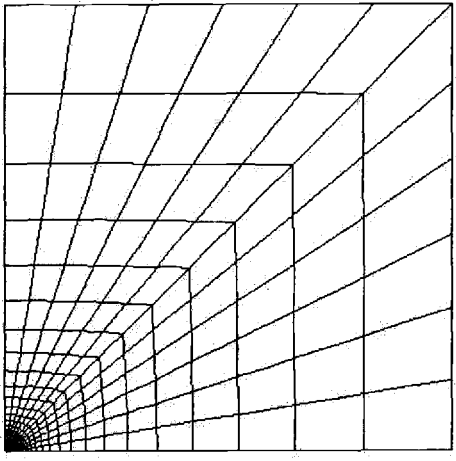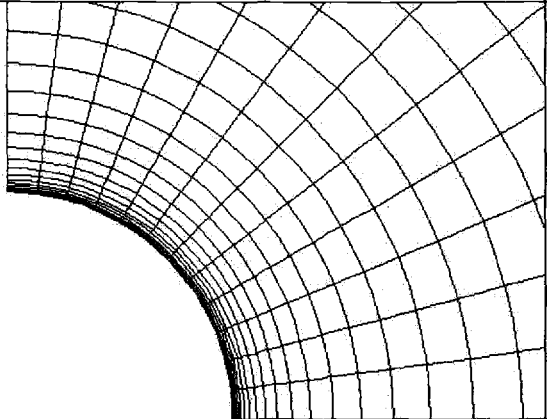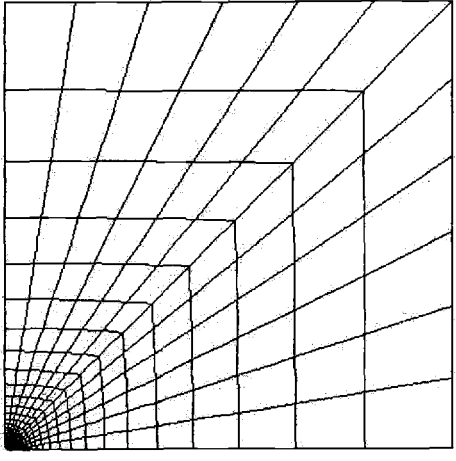
σ_2/σ_1	Cavity Shape	Deformed Body
1		
0.95		

Table 5.3 Deformed meshes at the FEA predicted failure on constrained silver
for $0.5 \le \sigma_2/\sigma_1 \le 1$ (Continued).
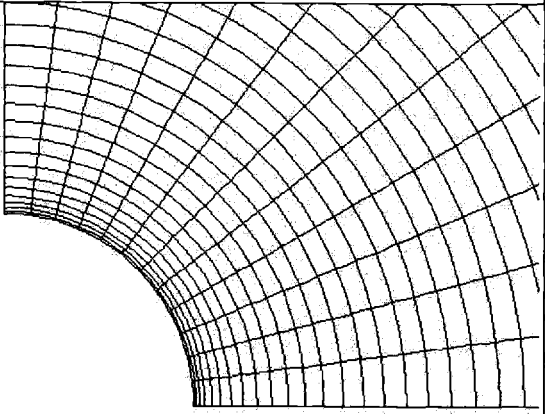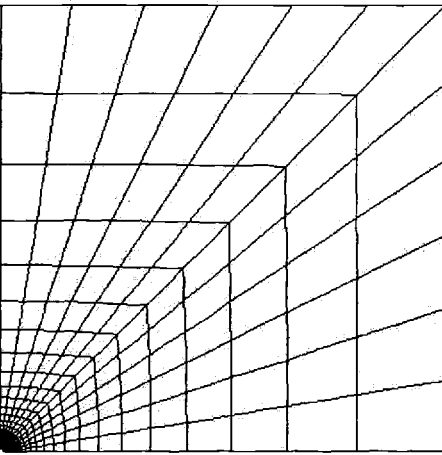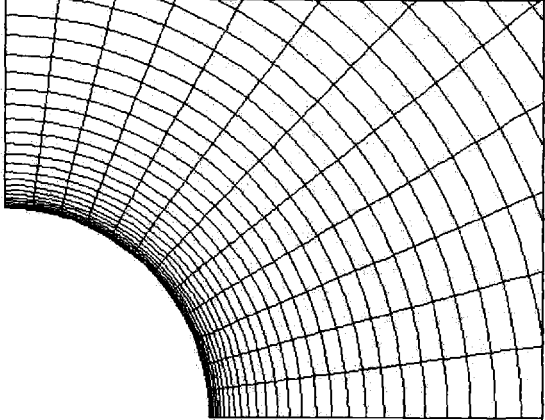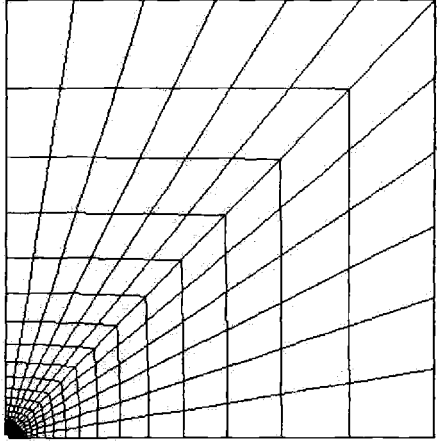
σ_2/σ_1	Cavity Shape	Deformed Body
0.9		
0.85		

Table 5.3 Deformed meshes at the FEA predicted failure on constrained silver for $0.5 \leq \sigma_2/\sigma_1 \leq 1$ (Continued).
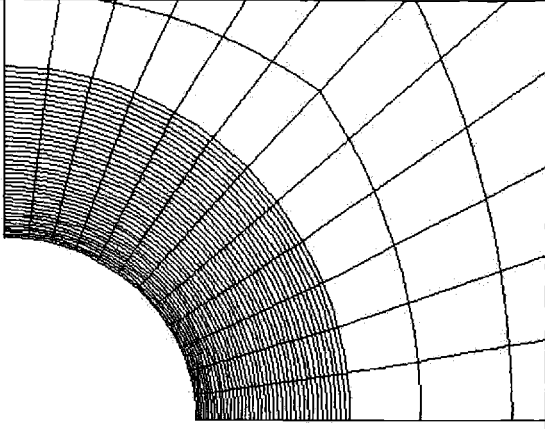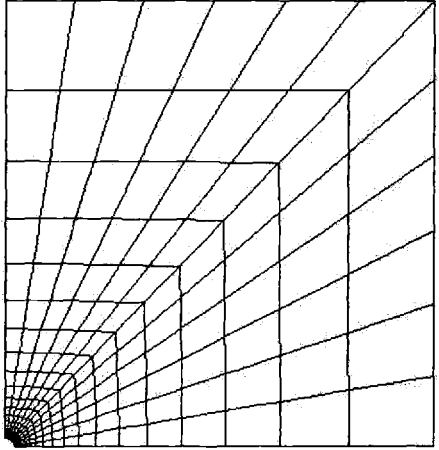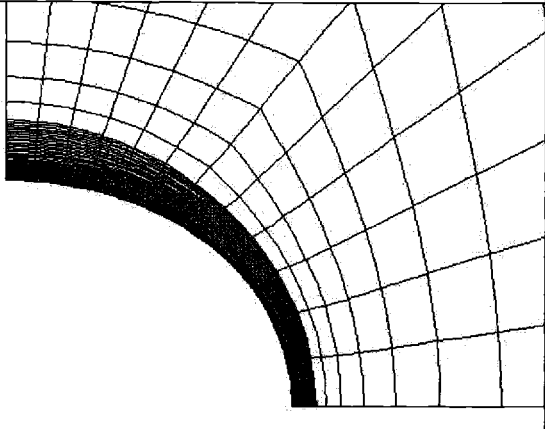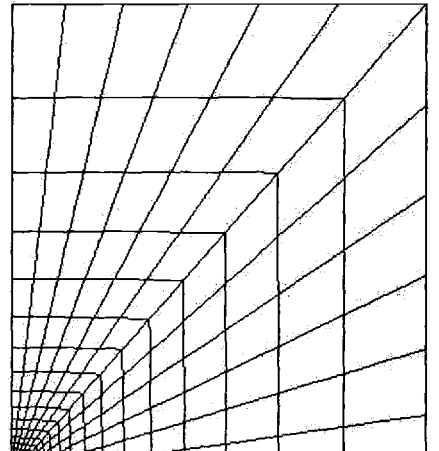
σ_2/σ_1	Cavity Shape	Deformed Body
0.8		
0.75		

Table 5.3 Deformed meshes at the FEA predicted failure on constrained silver for 0.5 $\leq \sigma_2/\sigma_1 \leq 1$ (Continued).
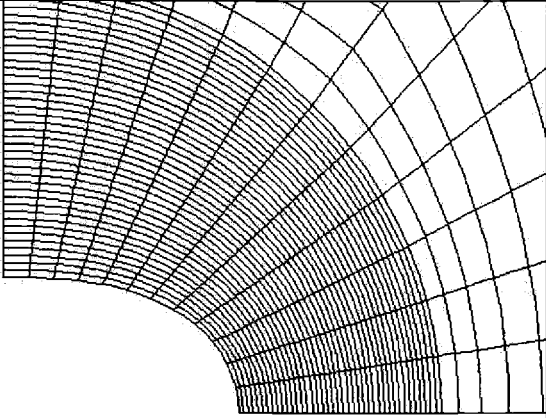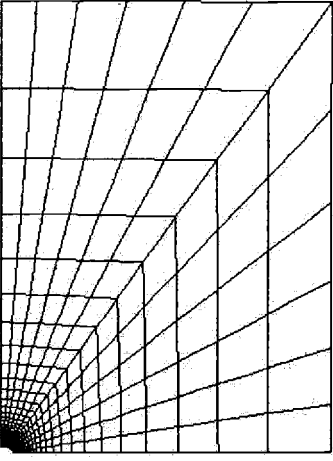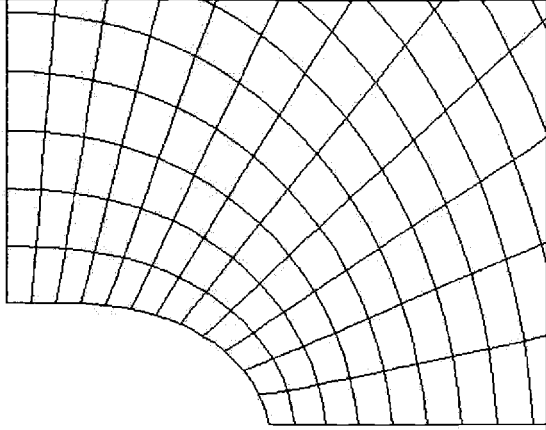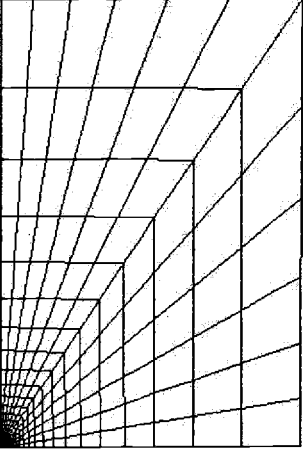
σ_2/σ_1	Cavity Shape	Deformed Body
0.7		
0.65		

Table 5.3 Deformed meshes at the FEA predicted failure on constrained silver for $0.5 \leq \sigma_2/\sigma_1 \leq 1$ (Continued).
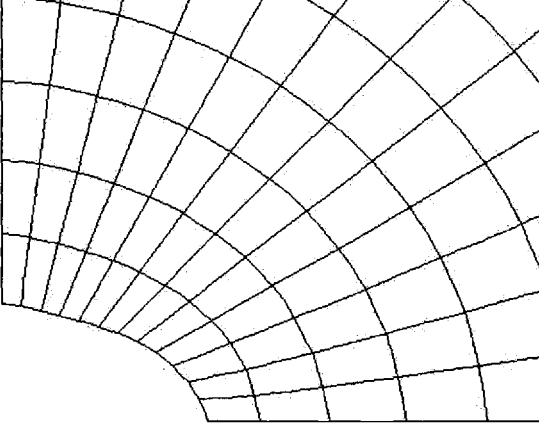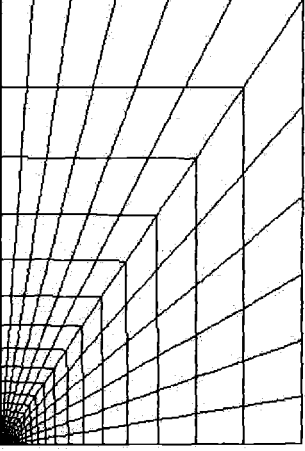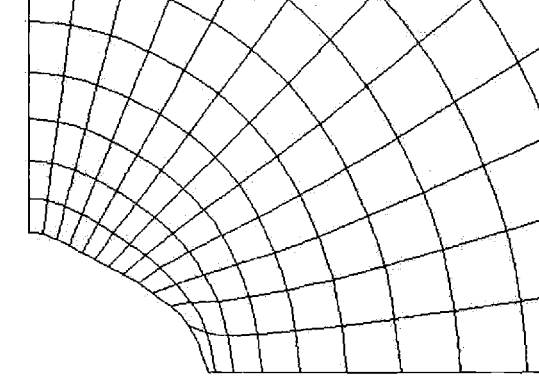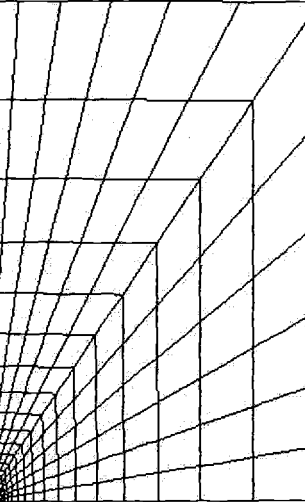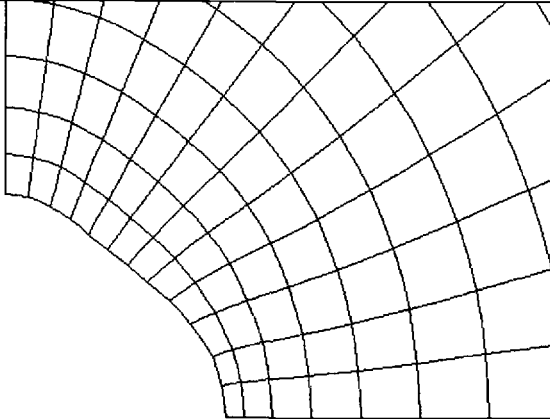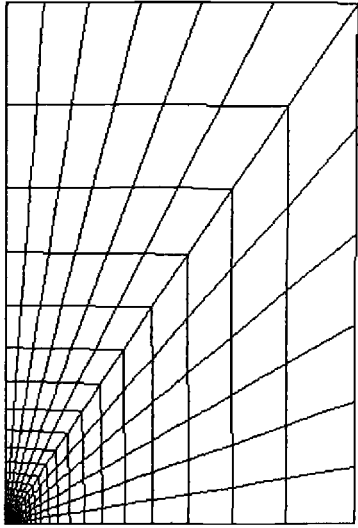
σ_2/σ_1	Cavity Shape	Deformed Body
0.6		
0.55		

Table 5.3 Deformed meshes at the FEA predicted failure on constrained silver for $0.5 \leq \sigma_2/\sigma_1 \leq 1$ (Continued).

σ_2/σ_1	Cavity Shape	Deformed Body
0.5		

5.3 DYNAMIC ANALYSIS OF CAVITATION INSTABILITIES UNDER SPHERICALLY-SYMMETRIC LOADING

The objective of this study was to validate a finite element solution with an analytical solution presented in Chapter 3. A model of cavity expansion in a finite body subjected to sudden remote spherically-symmetric loading was accomplished using the ABAQUS/Explicit program (for analyses with inertia effects) and ABAQUS/Standard program (for analyses without inertia effects) respectively. In case of an analysis with inertia effects, a finite element analysis provided both an explicit solver and adaptive mesh capability. Since the adaptive mesh procedure required us to use only a linear element, a quarter symmetric mesh was constructed using four-node, axisymmetric, quadrilateral elements. In the later case, a finite element analysis provided the Newton-Raphson solver, and a mesh was constructed using eight-node, axisymmetric, quadrilateral elements.

5.3.1 Cavitation instabilities in an infinite solid body with combined strain-rate hardening and inertia effects

A finite element mesh consisted of 600 elements graded with a fine mesh near the cavity and a coarse mesh away from the cavity. To eliminate reflected waves from boundaries, infinite elements were attached to all elements along the outer boundaries. Then, a quarter symmetry mesh was sliced into a small piece in order to accelerate the computational time. Figure 5.25 illustrates a finite element mesh at $L/D = 600$. This finite element mesh was obtained from the extensive numerical testing needed to sufficiently represent an infinite body. The material is assumed to be an incompressible and elastic/perfectly-plastic solid with linear strain-rate hardening effects: $E = 10$ Mpsi, $\varepsilon_y = 0.004$, $\rho = 0.000259$ lb-sec^2/in^4, the linear strain-rate hardening coefficients, $C = 0.005, 0.01, 0.05,$ and 0.1 sec, and $Y = 25,000\ (1 + C\dot{\varepsilon}_p)$ psi. The quasi-static cavitation stress, S_{cr}, was found to be 163.093 Ksi as presented in Section 3.2.3.
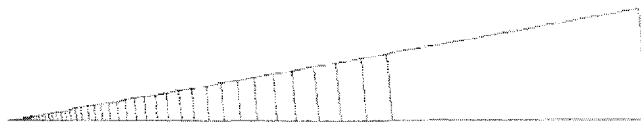
Figure 5.25 Finite element mesh for a spherical body using an infinite element on the outer surface

Figures 5.26 and 5.27 illustrate comparison between a FEA and analytical solution under step loading. However, for preventing numerical difficulties in the finite element analysis, this load was applied over a rise time of 4.5×10^{-6} sec and then held constant. This rise time is less than the time required for the material

around the cavity to reach the yield point. Figure 5.26 illustrates cavity expansion (in 1-direction at $C = 0.1$ sec) under a remote stress with magnitude of 2 percent above and 2 percent below the quasi-static cavitation stress, S_{cr}. Figure 5.27 illustrates cavity expansion (in the 1-direction) under a remote stress, $S = 163.094$ Ksi (slightly above S_{cr}), for various values of C.

It was found that the remote stress below the quasi-static cavitation stress (i.e., $S = 0.98 \ S_{cr}$) failed to cause a cavitation instability while the value above it did. As C increases, the rate of cavity expansion decreases. Moreover, we found a good agreement between FEA and analytical solutions in all cases.
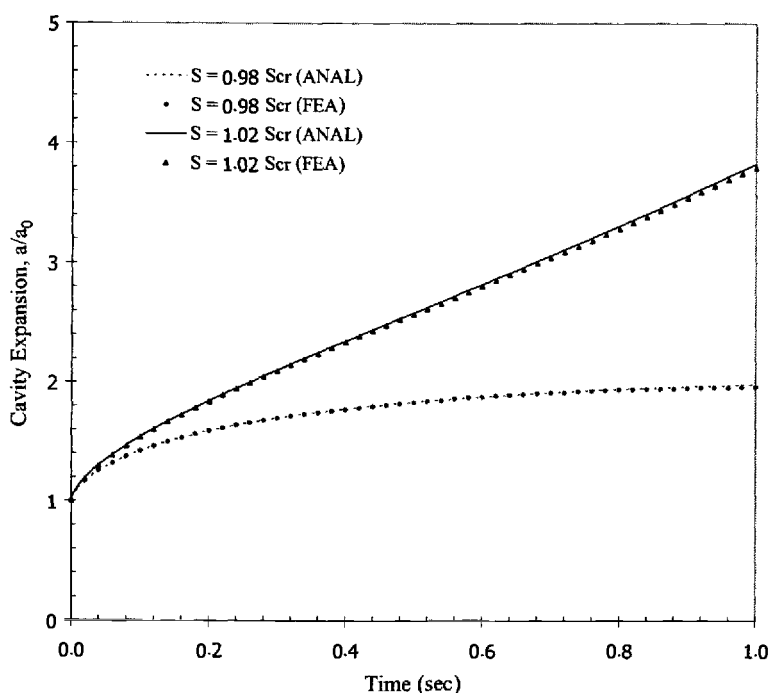
Figure 5.26 Cavity expansion vs. time for dynamic responses (with combined linear strain-rate hardening and inertia effects at $C = 0.1$ sec) under spherically-symmetric loading by the analytical approach (ANAL) and the finite element approach (FEA).
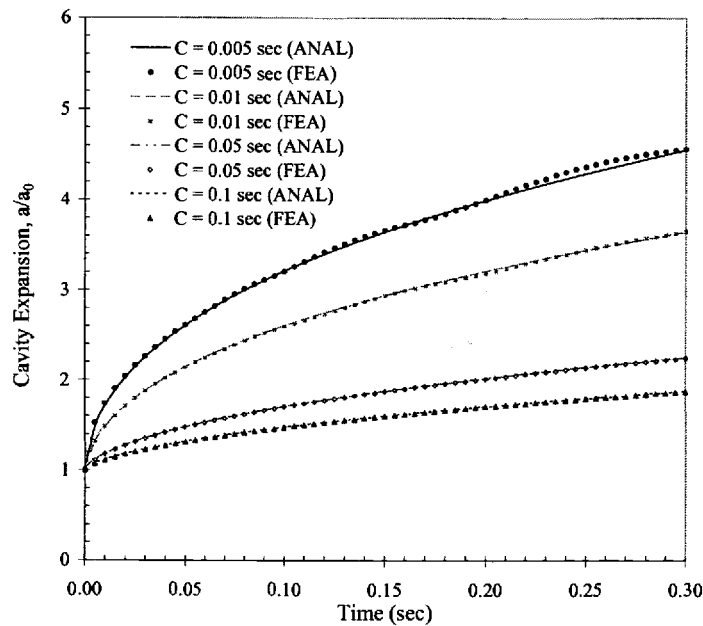
Figure 5.27 Cavity expansion vs. time for dynamic responses (with combine strain-rate hardening and inertia effects) under spherically-symmetric loading (at $S = 163.094$ Ksi) for various linear strain-hardening coefficients, $0.1 \leq C \leq 0.005$ sec. The analytical and finite element approaches are represented by ANAL and FEA respectively.

5.3.2 Cavitation instabilities in an infinite solid body with only inertia effects

A quarter symmetry mesh consisted of 1000 elements graded with a fine mesh near the cavity and a coarse mesh away from the cavity where $L/D = 100$ (for a case of $S = 158$ Ksi) and $L/D = 300$ (for a case of $S = 163.094$ Ksi). Again, this finite element mesh was obtained from extensive numerical testing needed to sufficiently represent an infinite body. The material is assumed to be incompressible and elastic/perfectly-plastic solid: $E = 10$ Mpsi, $\varepsilon_y = 0.004$, $\rho = 0.000259$ lb-sec^2/in^4.

Figures 5.28 and 5.29 illustrate a comparison between the FEA and analytical solution for cavity expansion (in 1-direction) in a spherical body

subjected to step loadings with magnitude of 158 Ksi and 163.094 Ksi below

and above S_{cr}. Again, for preventing numerical difficulties in the finite element

analysis, this load was applied over a rise time of 4.5×10^{-6} sec and then held

constant.

It is found that there is good agreement between FEA and analytical

solutions in both cases. In case of a remote stress below the quasi-static cavitation

stress (i.e., $S = 158$ Ksi), a cavitation instability failed to occur while the value

above it did.
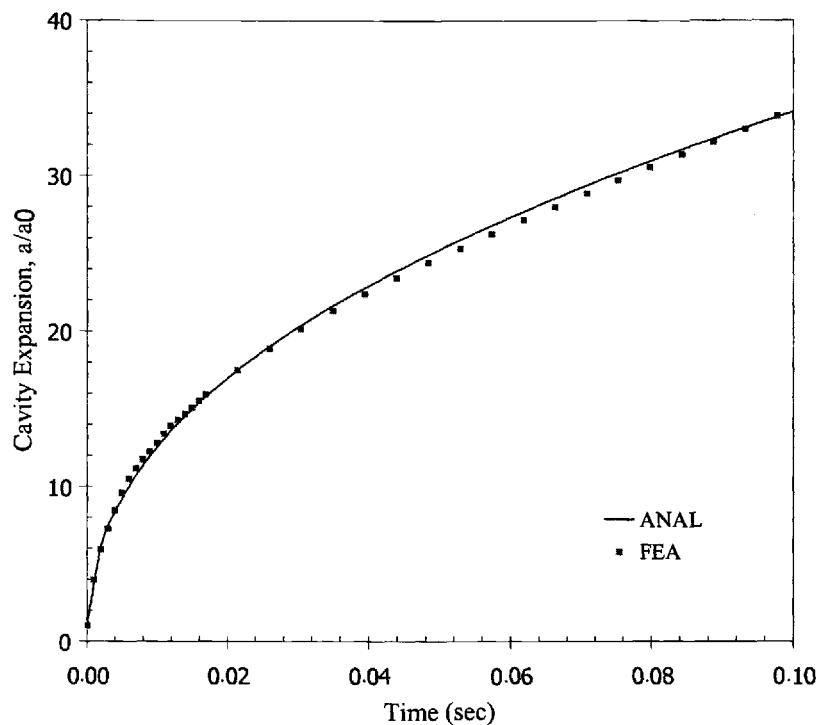
Figure 5.28 Cavity expansion vs. time for dynamic responses (only inertia effects) under spherically-symmetric loading (at $S = 163.094$ Ksi) by the analytical approach (ANAL) and the finite element approach (FEA).
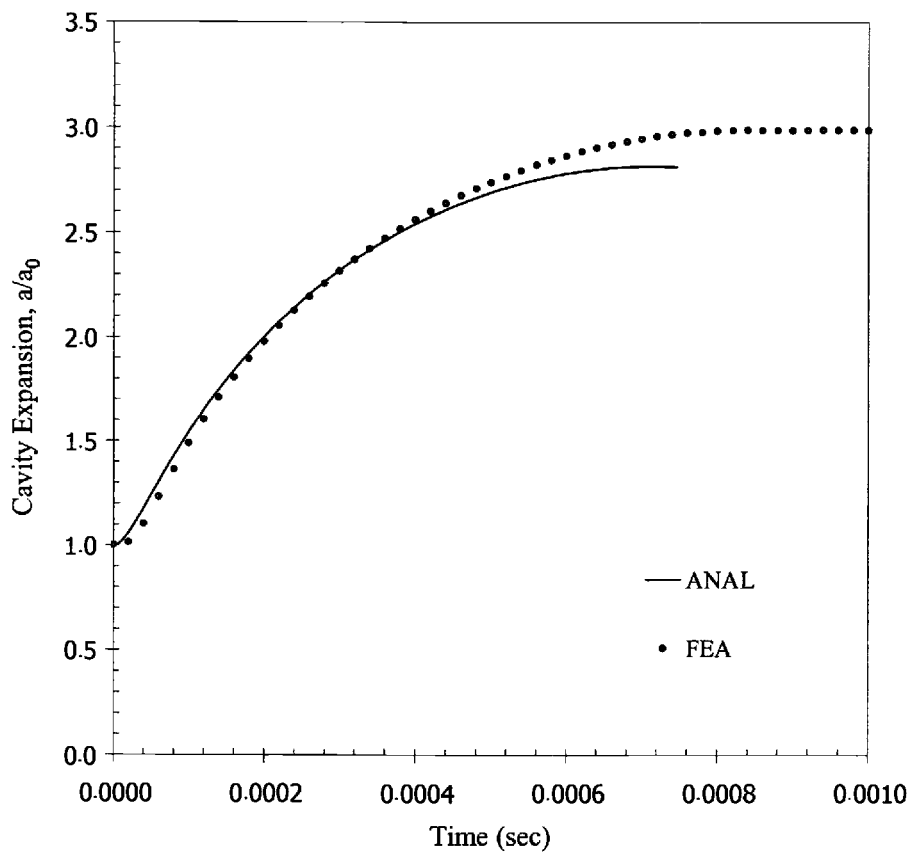
Figure 5.29 Cavity expansion vs. time for dynamic responses (only inertia effects) under spherically-symmetric loading (at $S = 158$ Ksi) by the analytical approach (ANAL) and the finite element approach (FEA).

5.3.3 Cavitation instabilities in an infinite solid body with only strain-rate hardening effects

A quarter symmetry mesh consisted of 720 elements graded with a fine mesh near the cavity and a coarse mesh away from the cavity with $L/D = 10,000$. Again, this finite element mesh was obtained from extensive numerical testing as described in Appendix C. The material is assumed to be incompressible and elastic/perfectly-plastic solid with linear strain-rate hardening effects: $E = 10$ Mpsi,

$\varepsilon_y = 0.004$, $\rho = 0.000259$ lb-sec^2/in^4, and the linear strain-rate hardening

coefficients, $C = 0.1$ and 0.05 sec.

Figure 5.30 illustrates a comparison between the FEA and analytical

solution for cavity expansion (in 1-direction) in a spherical body subjected to step

loadings with magnitude of 163.094 Ksi for $C = 0.1$ and 0.05 sec respectively. It

was found that the agreement between the FEA and analytical solution is good for

$C \geq 0.05$ sec. However, for $C < 0.05$ sec, a FEA solution was blow up after a short

time period.
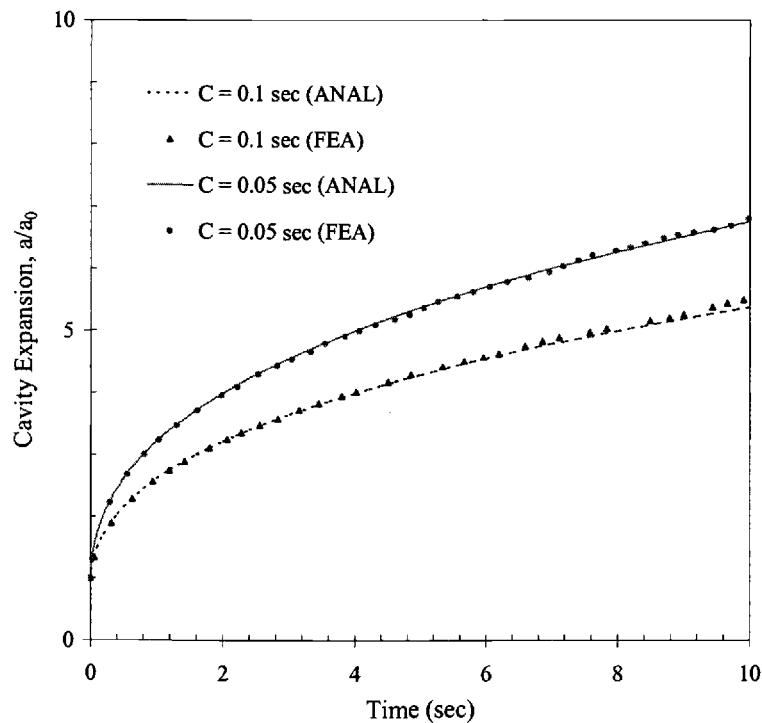
Figure 5.30 Cavity expansion vs. time for dynamic responses (with only strain-rate effects) under spherically-symmetric loading ($S = 163.094$ Ksi) for the linear strain-rate hardening coefficients, $C = 0.1$ and 0.05 sec. The analytical and finite element approach are represented by ANAL and FEA respectively.

5.4 DYNAMIC ANALYSIS OF CAVITATION INSTABILITIES UNDER AXISYMMETRIC LOADING

A model of cavity expansion in a finite body subjected to suddenly remote axisymmetric loading was accomplished using the ABAQUS/Explicit program (for a case when $\rho \neq 0$) and ABAQUS/Standard program (for a case when $\rho = 0$). The material is assumed to be incompressible and elastic/perfectly-plastic solids with power strain-rate hardening effects as illustrated in Figure 3.31 where $E = 10$ Mpsi, $\varepsilon_y = 0.004$, $\rho = 0.000259$ lb-sec^2/in^4, $C = 0.1$ sec, $n = 0.3$, and $Y = 25,000$ (1 + $0.1 \dot{\varepsilon}_p^{0.3}$). However, for the case when $\rho = 0$, the material is assumed to be compressible ($v = 0.45$) to prevent numerical difficulties in determining a quasi-static cavitation stress, S_{cr}. Again, the ramp loading was applied over a rise time of 4.5×10^{-6} sec and then held constant. In each case, load was applied to a body with magnitude of 2 percent above and 2 percent below the quasi-static cavitation stress. Values of quasi-static cavitation stress (or maximum principal stress) were obtained from a finite element analysis where $S_{cr} = 160.179$ Kpsi at $\sigma_2/\sigma_1 = 1$, $S_{cr} = 170.065$ Ksi at $\sigma_2/\sigma_1 = 0.9$, and $S_{cr} = 175.272$ Ksi at $\sigma_2/\sigma_1 = 0.8$ respectively.

For the case with only inertia effects, a finite element analysis provided both an explicit solver and adaptive mesh capability. A quarter symmetric mesh was constructed using four-node, axisymmetric, quadrilateral elements. For the later case, a finite element analysis provided the Newton-Raphson solver. The mesh was constructed using eight-node, axisymmetric, quadrilateral elements.
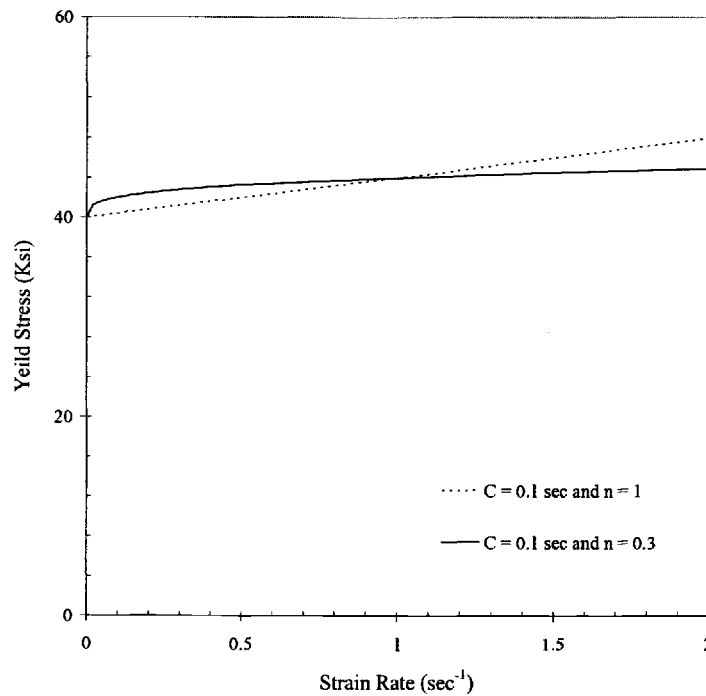
Figure 5.31 Yield stress vs. strain rate of incompressible and elastic/perfectly plastic material with power strain-rate hardening effects: $E = 10$ Mpsi, $\varepsilon_y = 0.004$, $\rho = 0.000259$ lb-sec^2/in^4, $C = 0.1$ sec, and $n = 0.3$.

5.4.1 Cavitation instabilities in an infinite solid body with only inertia effects

A quarter symmetry mesh consisted of 1000 elements graded with a fine mesh near the cavity and a coarse mesh away from the cavity with $L/D = 300$ (for a case of $S = 1.02\ S_{cr}$) and $L/D = 100$ (for a case of $S = 0.98\ S_{cr}$) where S is defined as a maximum principal stress.

Figures 5.32-5.34 illustrate the cavity expansion in the 1-direction as a function of time for $\sigma_2/\sigma_1 = 1, 0.9$, and 0.8, respectively. In each case, remote stress values below the quasi-static cavitation limit failed to cause a cavitation instability, while values above it did. For those cases, when cavitation did occur, the cavity expanded rapidly at first and then settled in a relatively uniform growth rate.

(a)
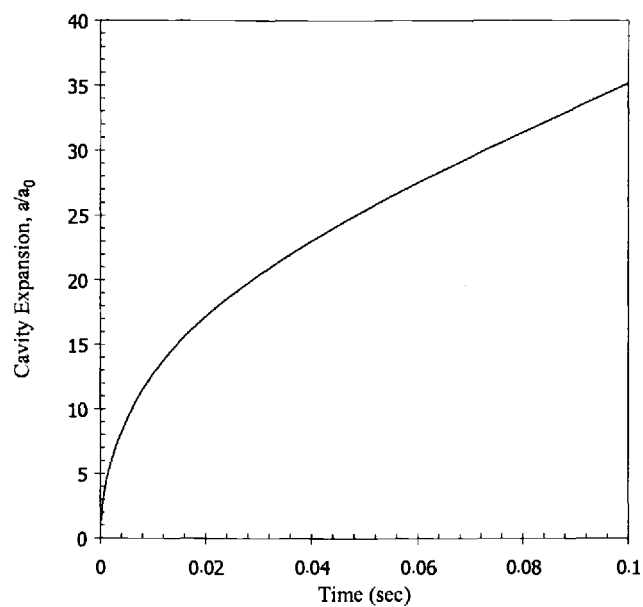
(b)
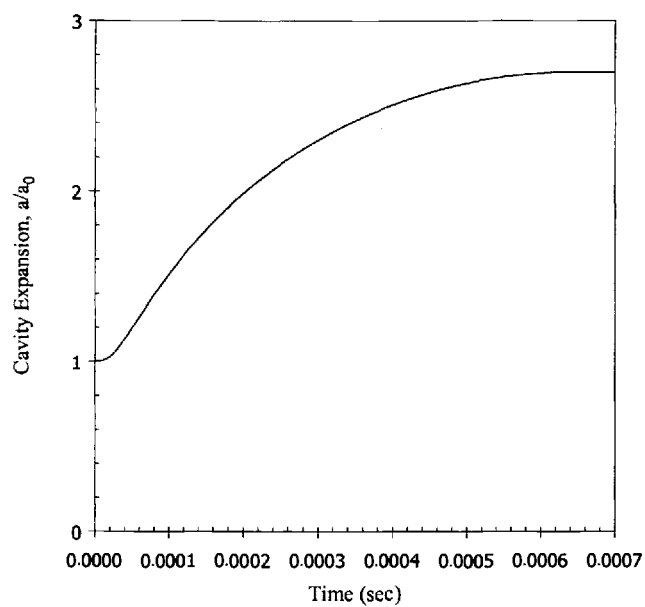
Figure 5.32 Cavity expansion vs. time for dynamic responses (only inertia effects) under axisymmetric loading at $\sigma_2/\sigma_1 = 1$ for (a) $S = 1.02\ S_{cr}$ and (b) $S = 0.98\ S_{cr}$.

(a)
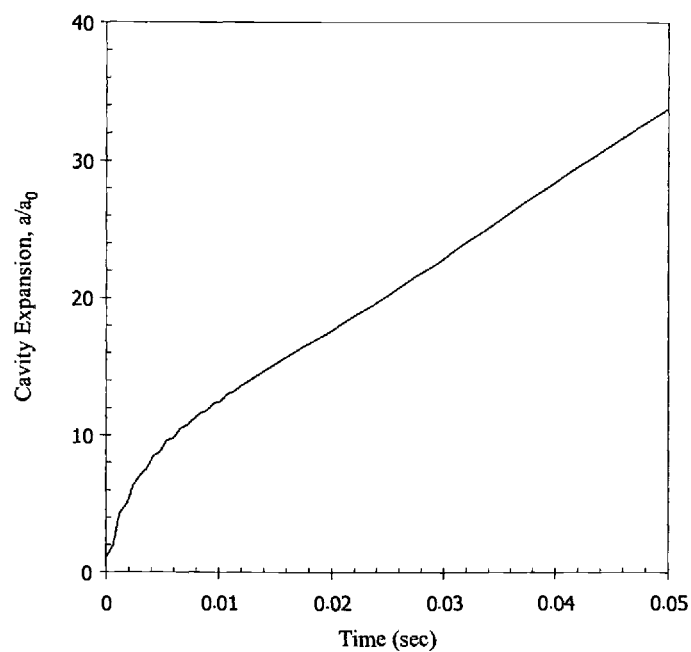
(b)
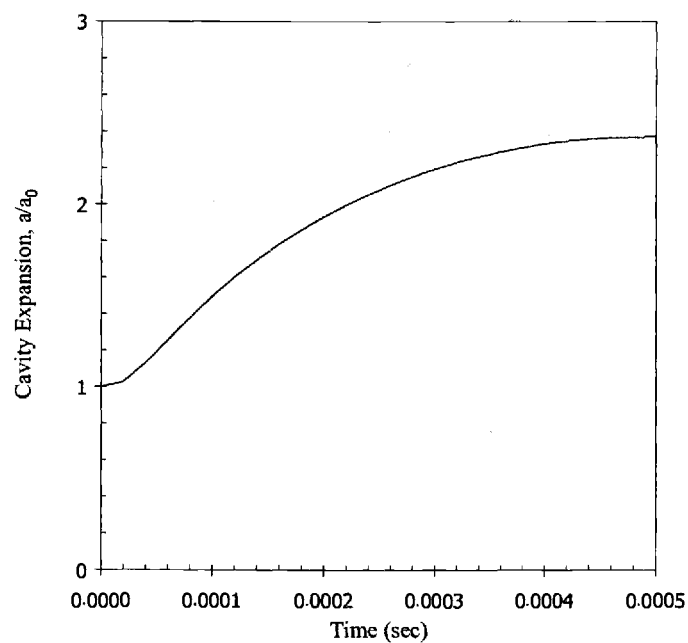
Figure 5.33 Cavity expansion vs. time for dynamic responses (only inertia effects) under axisymmetric loading at $\sigma_2/\sigma_1 = 0.9$ for (a) $S = 1.02\ S_{cr}$, and (b) $S = 0.98\ S_{cr}$.

(a)
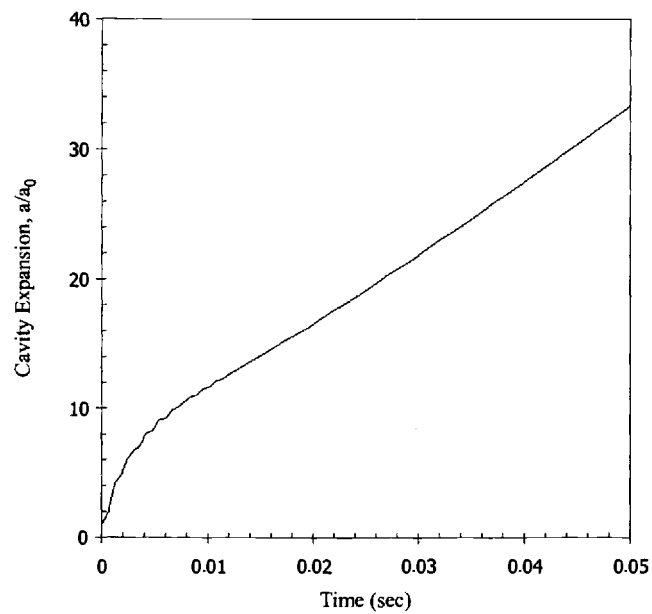
(b)
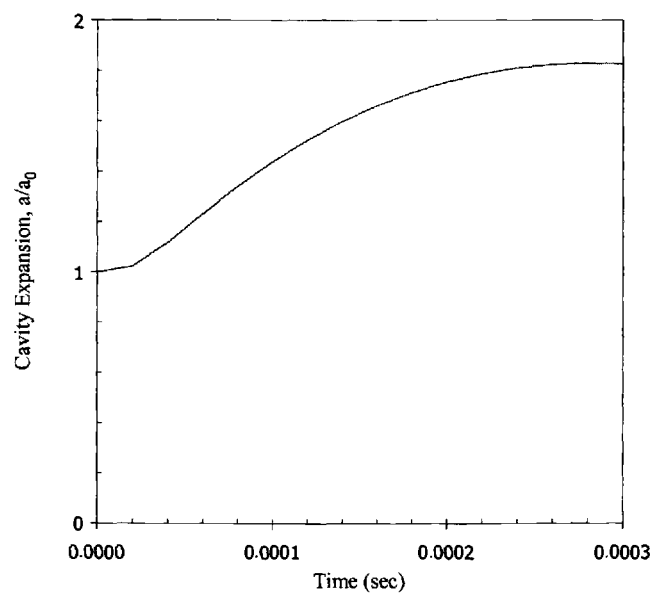
Figure 5.34 Cavity expansion vs. time for dynamic responses under axisymmetric loading at $\sigma_2/\sigma_1 = 0.8$ for (a) $S = 1.02\ S_{cr}$ and (b) $S = 0.98\ S_{cr}$.

5.4.2 Cavitation instabilities in an infinite solid body with only strain-rate hardening effects

A quarter symmetry mesh of a cylindrical model consisted of 720 elements graded with a fine mesh near the cavity and a coarse mesh away from the cavity with $L/D = 10,000$.

Figures 5.35-5.37 illustrate the cavity expansion in the 1-direction as a function of time for $\sigma_2/\sigma_1 = 1$, 0.9, and 0.8, respectively. Again, the remote stress values below the quasi-static cavitation limit failed to cause a cavitation instability, while values above it did. When cavitation occurs, the cavity expands rapidly and then settles into a uniform growth rate.
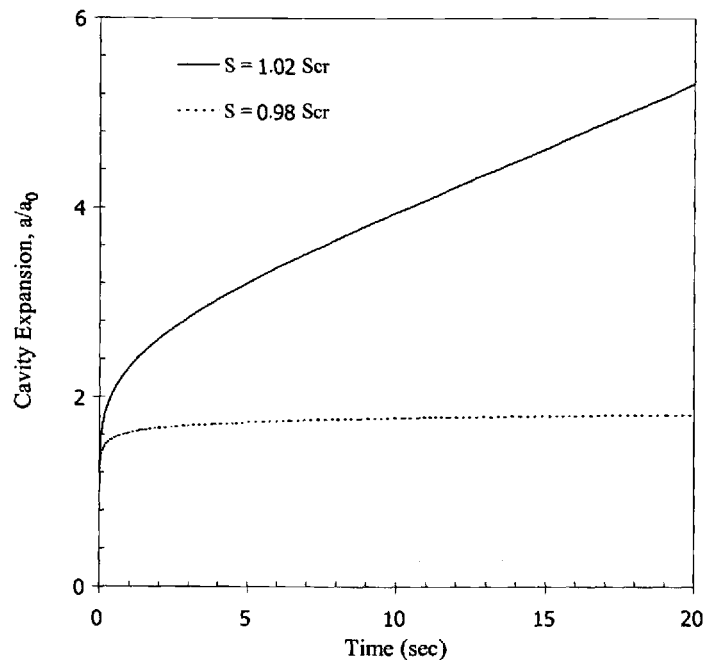
Figure 5.35 Cavity expansion vs. time for dynamic responses (with only strain-rate effects) under axisymmetric loading at $\sigma_2/\sigma_1 = 1$ for $S = 1.02 \ S_{cr}$ and 0.98 S_{cr} respectively.
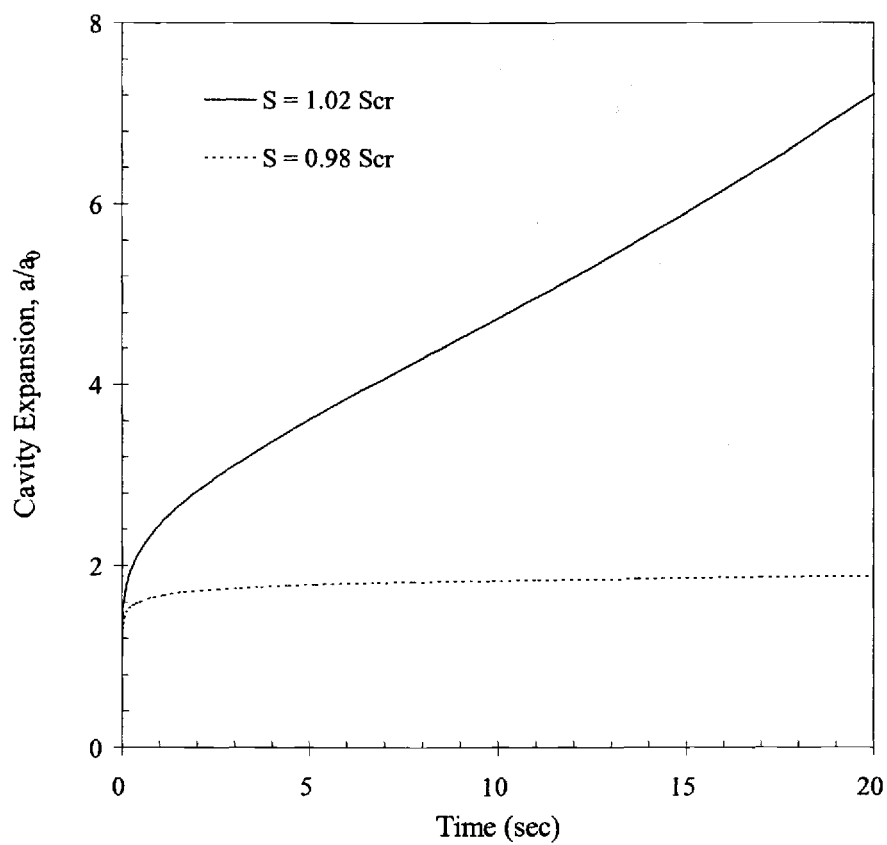
Figure 5.36 Cavity expansion vs. time for dynamic responses (with only strain-rate effects) under axisymmetric loading at $\sigma_2/\sigma_1 = 0.9$ for $S = 1.02\ S_{cr}$ and $0.98\ S_{cr}$ respectively.
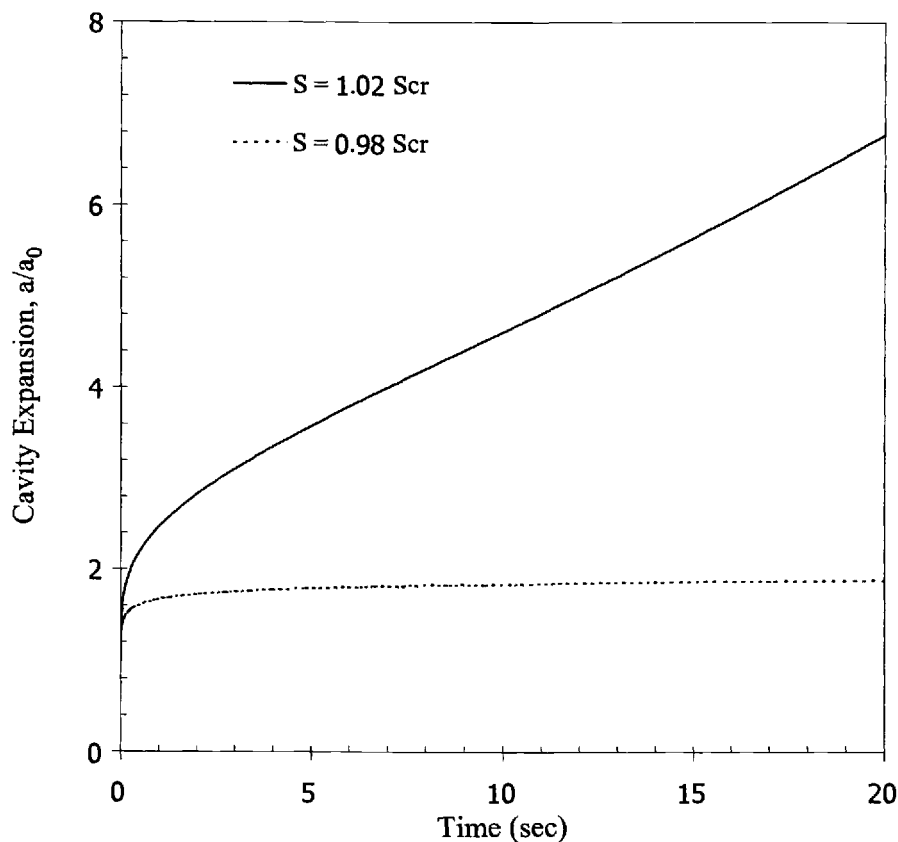
Figure 5.37 Cavity expansion vs. time for dynamic responses (with only strain-rate effects) under axisymmetric loading at $\sigma_2/\sigma_1 = 0.8$ for $S = 1.02$ S_{cr} and 0.98 S_{cr} respectively.

5.5 QUASI-STATIC ANALYSIS USING ABAQUS EXPLICIT

An explicit finite element analysis has been known for its computational efficiency over an implicit finite element analysis (Lindgren and Edberg, 1990; Robelo et al., 1992). In this study, a quasi-static response of a cavitation instability in constrained silver (as discussed in Section 5.2.3) was simulated using an explicit dynamic code, ABAQUS/Explicit. The FEA predicted quasi-static stresses at failure, S_{cr}, were equal to 838 and 904 MPa for $\sigma_2/\sigma_1 = 1$ and 0.9 respectively.

A quarter symmetry mesh consisted of 1,000 elements graded with a fine mesh near the cavity and a coarse mesh away from the cavity with $L/D = 300$. In each case, a ramp loading was applied to a body with magnitude of 838 MPa (for a case when $\sigma_2/\sigma_1 = 1$) and 902 MPa (for a case when $\sigma_2/\sigma_1 = 0.9$) over a rise time of 10 seconds and then held constant. These loading parameters were chosen after extensive numerical testing to minimize dynamic effects from a finite element solution. When remote stress is less than S_{cr}, a cavitation instability failed to occur, while a value above S_{cr} resulted in larger remote strain at instability. The CPU times required to execute these cases were 29 minutes and 35 seconds (for a case when $\sigma_2/\sigma_1 = 1$ comparing with 45 seconds in the static approach) and 27 minutes and 17 seconds (for a case when $\sigma_2/\sigma_1 = 0.9$ comparing with 54 seconds in the static approach) on HP J6000s server: 550MHz (dual processors) and 4GB RAM.

Figure 5.38 illustrates a comparison between solutions obtained from a static and dynamic approach. It was found that the agreement between these approaches is good when a remote field remains elastic (i.e., the case when $\sigma_2/\sigma_1 = 1$). However, this dynamic approach is an inefficient way to deal with this problem since the computational time was more than 30 times longer than a static approach. Moreover, simulating of a cavitation instability when yielding occurs in a remote field requires a large model size (i.e., $L/D > 5,000$) resulting in an increase of a number of elements in a mesh which increases computation time a considerable amount.
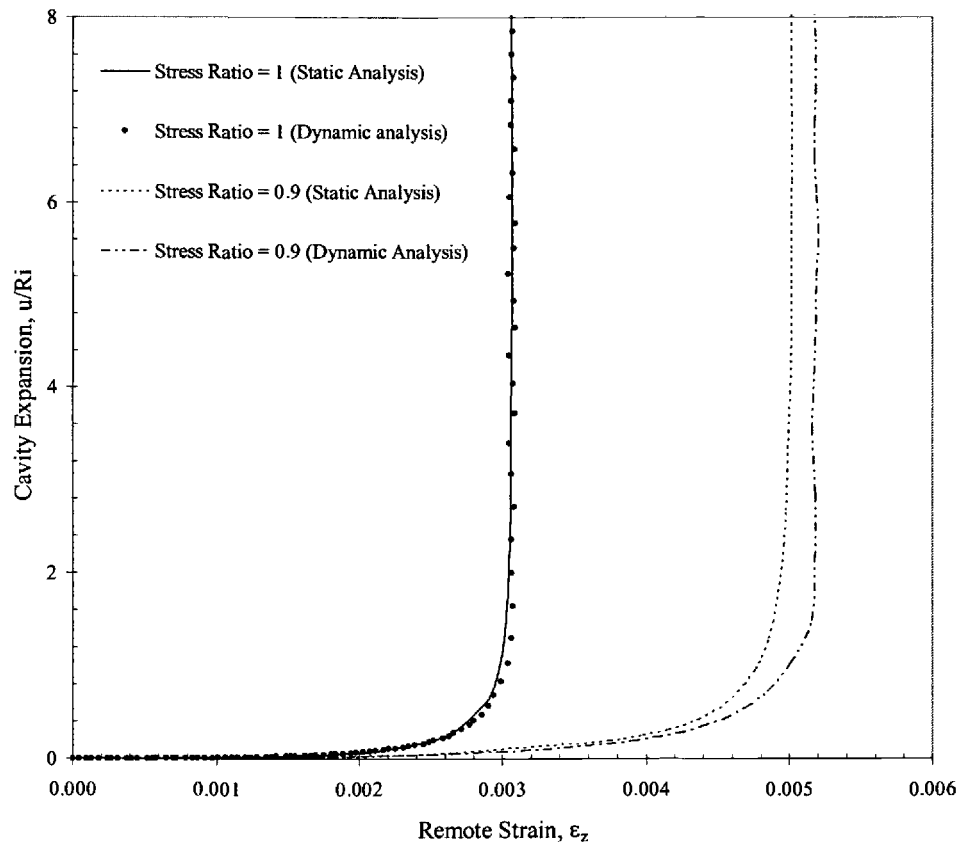
Figure 5.38 Comparison between the static and dynamic analysis at $\sigma_2/\sigma_1 = 1$ and 0.9 using the ABAQUS/Standard and ABAQUS/Explicit programs respectively. In the dynamic analysis, a body was subjected to the ramp loading over the rise time being sufficiently long to minimize inertia effects.

6. CONCLUSIONS

In this study, cavitation instabilities in elastic-plastic solids under spherically-symmetric and axisymmetric loadings were investigated. Both quasi-static and dynamic analyses were used to solve these problems.

In the quasi-static analyses, we investigated a cavitation instability in elastic/perfectly-plastic, linear hardening elastic-plastic, power hardening elastic-plastic, and constrained silver materials. The feasibility of this finite element method was examined by comparing its solution to analytical solutions developed for a case of spherically-symmetric loading as discussed in Chapter 3. It was found that the agreement between these methods was good (less than 1 percent error). Furthermore, in the case of an axisymmetric loading, a cavitation instability was observed in all cases under no change in remote stresses and strains during the cavitation instability state. In the case of power hardening elastic-plastic material ($\varepsilon_y = 0.003$ and $n = 0.25$), the FEA solution was compared with the approximate solution (Hou and Abeyaretne, 1992). We found good agreement between these solutions only when the remote field remained elastic, i.e. $\sigma_2/\sigma_1 > 0.9$. In the case of constrained silver, we found good agreement between our FEA solution and experimental results (Kassner et al., 1998) except at $\sigma_2/\sigma_1 = 0.76$. Moreover, a cavitation instability was found for stress ratios beyond the range presented by Kassner et al. (i.e., as low as $\sigma_2/\sigma_1 = 0.5$). However, in our study, the values of cavitation stresses and remote strains appeared to be larger than those reported in their finite element analysis. This is simply because, with our sufficiently large model size, the effects of interactions between the cavity and remote boundaries can be minimized. As the stress ratio decreases, the remote strain increases substantially as the cavitation instability state is approached. Unfortunately, when the stress ratio was small (i.e., $\sigma_2/\sigma_1 < 0.6$ for the case of constrained silver), FEA simulations appeared to have difficulty determining the exact cavitation instability

state since the mesh along the boundaries deteriorated very fast during the onset of instability. In the case of a quasi-static analysis using an explicit finite element analysis, this approach was found to be an inefficient way to deal with a quasi-static problem since the computational time required is much longer than that of a static approach.

In the dynamic analysis, we investigated cavity expansion in incompressible and elastic/perfectly-plastic materials. Both inertia and strain-rate effects were considered. Again, the feasibility of this finite element method was examined by comparing its solution to the analytical solutions developed for a case of sudden remote spherically-symmetric loading as discussed in Chapter 3. It was found that the agreement between these methods was good. For dynamic loads below the critical load required for cavitation in the quasi-static case, the cavity expanded rapidly initially but eventually decelerated and stopped at a finite value. For dynamic loads above this critical value, the cavity expanded rapidly initially and then decelerated and settled into expansion at a constant rate. This observation held for both spherically-symmetric and axisymmetric loading

BIBLIOGRAPHY

1. ABAQUS, 2001, "Theoretical Manual," Hibbitt, Karlsson & Sorensen, Rhode Island.

2. Bathe, K., 1996, "Finite Element Procedures," Prentice Hall, New Jersey.

3. Bishop, R. F., Hill, R., and Mott, N. F., 1945, "The Theory of Indentation and Hardness Test.," Proc. Phys. Soc., Vol. 57, pp. 147-159.

4. Chadwick, P., 1957, "The Quasi-Static Expansion of a Spherical Cavity in Metals and Ideal Soils," J. Mech. Appl. Math, Vol. 12, pp. 52-71.

5. Cook et al., 2001, "Concepts and Applications of Finite Element Analysis," 4 ed., John Wiley & Sons.

6. Crisfield, M. A., 1981, "A Fast Incremental/Iterative Solution Procedure that Handles Snap-Through," in: Computers & Structures, Vol. 13, pp. 55-62.

7. Forrestal, M. J. and Luk, V. K., 1988, "Dynamic Spherical Cavity Expansion in a Compressible Elastic-Plastic Solid," J. Appl. Mech, Vol. 55, pp. 275-279.

8. Gent, A. N. and Lindsey, G. H., 1967, "Internal Rupture of Bonded Rubber Cylinders in Tension," Proceeding of the Royal Society of London," Vol. A249, pp. 195-205.

9. Haung, Y., Hutchinson, J. W., and Tvergaard, V., 1991, "Cavitation Instabilities in Elastic-Plastic Solids," J. Mech. Phys. Solids, Vol. 39, pp. 223-241.

10. Hill, R., 1948, "Unpublished Report (Ministry of Supply, United Kingdom)".

11. Hill, R., 1950, "The Solution of Plastic-Elastic Problem II," in: The Mathematical Theory of Plasticity," Oxford University Press, London, pp. 97-106.

12. Hoffman, J. D., 1992, "The Secant Method," Numerical Methods for Engineers and Scientists, McGraw-Hill, New York, pp. 101-104.

13. Hopkins, H. G., 1960, "Dynamic Expansion of Spherical Cavities in Metals," in: Progress in Solid Mechanics," Vol. 1, North-Holland Publishing Company, New York, pp. 85-164.

14. Kassner, M. E., Kennedy, T. C., and Schrems, K. K., 1998, "The Mechanism of Ductile Fracture in Constrained Thin Silver Films," Acta mater., Vol. 46, pp. 6445-6457.

15. Kennedy, T. C., Puttapitukporn, T., Kassner, M. E., 2003, " Dynamic Effects on Cavitation Instabilities in Solids," to be submitted to Acta Mechanica.

16. Koplik, J. and Needleman, A., 1998, "Void Growth and Coalescence in Porous Plastic Solids," Int. J. Solids Struct., Vol. 8, pp. 835-853.

17. Lindgren, L. and Edberg, J., 1990, "Explicit Versus Implicit Finite Element Formulation in Simulation of Rolling," Journal of Materials Processing Technology, Vol. 24, pp. 85-94.

18. Luk, V. K., Forrestal, M. J., and Amos, D. E., 1991, "Dynamic Spherical Cavity Expansion of Strain-Hardening Materials," J. Appl. Mech., Vol. 58, pp. 1-6.

19. McClintock, F. A., 1968, "A Criterion for Ductile Fracture by the Growth of Holes," J. Appl. Mech., Vol. 2, pp. 363-371.

20. Mendelson, A., 1968, "Elastoplastic Problems of Spheres and Cylinders," in: Plasticity: Theory and Application, Krieger Publishing Company, pp. 135-161.

21. Perzyna, P., 1966, "Fundamental Problems in Viscoplasticity," in: Advances in Applied Mechanics," Vol. 9, Academic Press., New York, pp. 243-368.

22. Ramm, E., 1981, "Strategies for Tracing Nonlinear Responses Near Limit Points," in: Nonlinear Finite Element Analysis in Structural Mechanics, Springer-Verlag, New York, pp. 63-69.

23. Rice, J. R. and Tracey, D. M., 1969, "On The Ductile Enlargement of Voids in Triaxial Stress Fields," J. Mech. Phys. Solids, Vol. 17, pp. 201-217.

24. Robelo, N., Nagtegaal, J. C., and Taylor, L. M., 1992, "Industrial Application of Implicit and Explicit Finite Element Methods to Forming Processes," ASME, Vol. 156, pp. 67-75.

25. Schrems, K. K., 1999, "Ductile Fracture of Metals under Triaxial States of Stress," Thesis, Oregon State University.

26. Timoshenko, S. P. and Goodier, J. N., "Axisymmetric Stress and Deformation in Solid of Revolution," in: Theory of Elasticity, 3 ed., McGraw-Hill, New York, pp. 380-402.

27. Tolle, M. C., 1994, "Ductile Fracture of Metals under High Triaxial Stress States," Thesis, Oregon State University.

28. Tvergaard, V., 1999, "Effects of Large Elastic Strains on Cavitation Instability Predictions for Elastic-Plastic Solids," International Journal of Solids and Structures, Vol. 36, pp. 5453-5466.

29. Tvergaard, V., Haung, Y., and Hutchinson, J. W., 1992, "Cavitation Instabilities in a Power Hardening Elastic-Plastic Solid," Eur. J. Appl. Mech., Vol. 11, pp. 215-231.

30. Whittaker, E. T. and Watson, G. N., 1935, "The Zeta Function of Riemann," in: A Course of Modern Analysis, 4 ed., Cambridge, pp.265-266.

31. Yerzley, F. L., 1939, "Adhesion of Neoprene to Metal," Ind. Eng. Chem., Vol. 31, pp. 950-956.

APPENDICES

APPENDIX A
THE ZET FUNCTION OF RIEMANN

A.1 DEFINITION OF THE ZETA-FUNCTION

Let $s = \sigma + it$ where s and t are real; then, if $d > 0$, the series

$$\varsigma(s) = \sum_{n=1}^{\infty} \frac{1}{n^s},$$

is a uniformly convergent series of analytic function in any domain in which ; and consequently the series is an analytic function of s in such a domain. The function is called the Zeta-function; although it was known to Euler, its most remarkable properties were not discovered before Riemann who discussed it in his memoir on prime numbers; it has since proved to be of fundamental importance, not only the Theory of Prime Numbers, but also in the higher theory of the Gamma-function and allied functions.

A.2 THE GENERALIZED ZETA-FUNCTION

Many of the properties possessed by the Zeta-function are particular cases of properties possessed by a more general function defined, when $\sigma \geq 1 + \delta$, by the equation

$$\varsigma(s,a) = \sum_{n=0}^{\infty} \frac{1}{(a+n)^s},$$

where a is a constant. For simplicity, it is assumed that $0 < a \leq 1$, and then taking $\arg(a + n) = 0$. It is evident that $\zeta(s, a) = \zeta(s)$.

A.3 THE EXPRESSION OF AN INFINITE INTEGRAL

Since $(a+n)^{-s}\Gamma(s) = \int_0^\infty x^{s-1}e^{-(n+a)x}dx$, when arg x = 0 (and a fortiori when σ

$\geq 1 + \delta$), we have $\sigma \geq 1 + \delta$,

$$\Gamma(s)\varsigma(s,a) = \lim_{N\to\infty}\sum_{n=0}^{N}\int_0^\infty x^{s-1}e^{-(n+a)x}dx,$$

$$= \lim_{N\to\infty}\left\{\int_0^\infty \frac{x^{s-1}e^{-ax}}{1-e^{-x}}dx - \int_0^\infty \frac{x^{s-1}}{1-e^{-x}}e^{-(N+1+a)x}dx\right\},$$

where $\Gamma(s)$ is the Gamma function.

Now, when $x \geq 0$, $e^x \geq 1+x$, and so the modulus of the second of these integrals does not exceed

$$\int_0^\infty x^{\sigma-2}e^{-(N+a)x}dx = (N+a)^{1-\sigma}\Gamma(\sigma-1),$$

which (when $\sigma \geq 1 + \delta$) tends to 0 as $N \to \infty$.

$$\varsigma(s,a) = \frac{1}{\Gamma(s)}\int_0^\infty \frac{x^{s-1}e^{-ax}}{1-e^{-x}}dx;$$

this formulas corresponds in some respects to Euler's integral for the Gamma function.

APPENDIX B
FORMULATIONS OF MATRICES IN FINITE ELEMENT NONLINEAR METHOD

The establishment of matrices used in the two-dimensional *UL* and *TL* formulations was presented by Bath (1991). In the numerical integration, these matrices are evaluated at the Gauss integration points.

B.1 TOTAL LARGRANGIAN FORMULATION

1. Linear Strain-Displacement Transformation Matrix

$$\,_0^t B_L = \,_0^t B_{L0} + \,_0^t B_{L1}.$$

$$\,_0^t B_{L0} = \begin{bmatrix} \,_0 h_{1,1} & 0 & \,_0 h_{2,1} & 0 & \cdots & \,_0 h_{N,1} & 0 \\ 0 & \,_0 h_{1,2} & 0 & \,_0 h_{2,2} & \cdots & 0 & \,_0 h_{N,2} \\ \,_0 h_{1,2} & \,_0 h_{1,1} & \,_0 h_{2,2} & \,_0 h_{2,1} & \cdots & \,_0 h_{N,2} & \,_0 h_{N,1} \\ \dfrac{h_1}{\,_0 \overline{x_1}} & 0 & \dfrac{h_2}{\,_0 \overline{x_1}} & 0 & \cdots & \dfrac{h_N}{\,_0 \overline{x_1}} & 0 \end{bmatrix},$$

and

$$\,_0^t B_{L1} = \begin{bmatrix} l_{11}\,_0 h_{1,1} & l_{21}\,_0 h_{1,1} & l_{11}\,_0 h_{2,1} \\ l_{12}\,_0 h_{1,2} & l_{22}\,_0 h_{1,2} & l_{12}\,_0 h_{2,2} \\ \left(l_{11}\,_0 h_{1,2} + l_{11}\,_0 h_{1,1} \right) & \left(l_{21}\,_0 h_{1,2} + l_{22}\,_0 h_{1,1} \right) & \left(l_{11}\,_0 h_{1,2} + l_{12}\,_0 h_{2,1} \right) \\ l_{33} \dfrac{h_1}{\,_0 \overline{x_1}} & 0 & l_{33} \dfrac{h_2}{\,_0 \overline{x_1}} \end{bmatrix}$$

$$\begin{bmatrix} l_{21}\,_0 h_{2,1} & \cdots & l_{11}\,_0 h_{N,1} & l_{21}\,_0 h_{N,1} \\ l_{22}\,_0 h_{2,2} & \cdots & l_{12}\,_0 h_{N,2} & l_{22}\,_0 h_{N,2} \\ \left(l_{21}\,_0 h_{2,2} + l_{22}\,_0 h_{2,1} \right) & \cdots & \left(l_{11}\,_0 h_{N,2} + l_{11}\,_0 h_{N,1} \right) & \left(l_{21}\,_0 h_{N,2} + l_{22}\,_0 h_{N,1} \right) \\ 0 & \cdots & l_{33} \dfrac{h_N}{\,_0 \overline{x_1}} & 0 \end{bmatrix},$$

where

$$_0h_{k,j} = \frac{\partial h_k}{\partial ^0x_j};$$

$$u_j^k = {}^{t+\Delta t}u_j^k - {}^tu_j^k;$$

$$^0\overline{x}_1 = \sum_{k=1}^{N} h_k \, {}^0x_1^k;$$

$$l_{11} = \sum_{k=1}^{N} {}_0h_{k,1} \, {}^tu_1^k;$$

$$l_{22} = \sum_{k=1}^{N} {}_0h_{k,2} \, {}^tu_2^k;$$

$$l_{21} = \sum_{k=1}^{N} {}_0h_{k,1} \, {}^tu_2^k;$$

$$l_{12} = \sum_{k=1}^{N} {}_0h_{k,2} \, {}^tu_1^k;$$

$$l_{33} = \frac{\displaystyle\sum_{k=1}^{N} h_k \, {}^tu_1^k}{{}^0\overline{x}_1};$$

N = number of nodes.

2. Nonlinear Strain-Displacement Transformation Matrix

$$_0^tB_{NL} = \begin{bmatrix} _0h_{1,1} & 0 & _0h_{2,1} & 0 & \cdots & _0h_{N,1} & 0 \\ _0h_{1,2} & 0 & _0h_{2,2} & 0 & \cdots & _0h_{N,2} & 0 \\ 0 & _0h_{1,1} & 0 & _0h_{2,1} & \cdots & 0 & _0h_{N,1} \\ 0 & _0h_{1,2} & 0 & _0h_{2,2} & \cdots & 0 & _0h_{N,2} \\ \dfrac{h_1}{{}^0\overline{x}_1} & 0 & \dfrac{h_2}{{}^0\overline{x}_1} & 0 & \cdots & \dfrac{h_N}{{}^0\overline{x}_1} & 0 \end{bmatrix}.$$

3 Second Pilola-Kirchhoff Stress Matrix and Vector

$$\left[{}_0^t S\right] = \begin{bmatrix} {}_0^t S_{11} & {}_0^t S_{12} & 0 & 0 & 0 \\ {}_0^t S_{21} & {}_0^t S_{22} & 0 & 0 & 0 \\ 0 & 0 & {}_0^t S_{11} & {}_0^t S_{12} & 0 \\ 0 & 0 & {}_0^t S_{21} & {}_0^t S_{22} & 0 \\ 0 & 0 & 0 & 0 & {}_0^t S_{33} \end{bmatrix},$$

$$\left\{{}_0^t S\right\} = \begin{Bmatrix} {}_0^t S_{11} \\ {}_0^t S_{22} \\ {}_0^t S_{12} \\ {}_0^t S_{33} \end{Bmatrix}.$$

B.2 UPDATED LAGRANGIAN FORMULATION

1. Linear Strain-Displacement Transformation Matrix

$$_t^t B_L = \begin{bmatrix} {}_t h_{1,1} & 0 & {}_t h_{2,1} & 0 & \cdots & {}_t h_{N,1} & 0 \\ 0 & {}_t h_{1,2} & 0 & {}_t h_{2,2} & \cdots & 0 & {}_t h_{N,2} \\ {}_t h_{1,2} & {}_t h_{1,1} & {}_t h_{2,2} & {}_t h_{2,1} & \cdots & {}_t h_{N,2} & {}_t h_{N,1} \\ \dfrac{h_1}{{}^t \overline{x}_1} & 0 & \dfrac{h_2}{{}^t \overline{x}_1} & 0 & \cdots & \dfrac{h_N}{{}^t \overline{x}_1} & 0 \end{bmatrix},$$

where

$$_t h_{k,j} = \frac{\partial h_k}{\partial {}^t x_j};$$

$$u_j^k = {}^{t+\Delta t} u_j^k - {}^t u_j^k;$$

$$^t \overline{x}_1 = \sum_{k=1}^{N} h_k \, {}^t x_1^k.$$

2. Nonlinear Strain-Displacement Transformation Matrix

$$
{}_0^t B_{NL} = \begin{bmatrix}
{}_t h_{1,1} & 0 & {}_t h_{2,1} & 0 & \cdots & {}_t h_{N,1} & 0 \\
{}_t h_{1,2} & 0 & {}_t h_{2,2} & 0 & \cdots & {}_t h_{N,2} & 0 \\
0 & {}_t h_{1,1} & 0 & {}_t h_{2,1} & \cdots & 0 & {}_t h_{N,1} \\
0 & {}_0 h_{1,2} & 0 & {}_t h_{2,2} & \cdots & 0 & {}_t h_{N,2} \\
\dfrac{h_1}{{}^t \overline{x_1}} & 0 & \dfrac{h_2}{{}^t \overline{x_1}} & 0 & \cdots & \dfrac{h_N}{{}^t \overline{x_1}} & 0
\end{bmatrix}
$$

3. Second Pilola-Kirchhoff Stress Matrix and Vector

$$
\left[{}^t \sigma \right] = \begin{bmatrix}
{}^t \sigma_{11} & {}^t \sigma_{12} & 0 & 0 & 0 \\
{}^t \sigma_{21} & {}^t \sigma_{22} & 0 & 0 & 0 \\
0 & 0 & {}^t \sigma_{11} & {}^t \sigma_{12} & 0 \\
0 & 0 & {}^t \sigma_{21} & {}^t \sigma_{22} & 0 \\
0 & 0 & 0 & 0 & {}^t \sigma_{33}
\end{bmatrix},
$$

$$
\left\{ {}^t \sigma \right\} = \begin{Bmatrix}
{}^t \sigma_{11} \\
{}^t \sigma_{22} \\
{}^t \sigma_{12} \\
{}^t \sigma_{33}
\end{Bmatrix}.
$$

APPENDIX C
EFFECTS OF MODEL SIZES ON A QUASI-STATIC ANALYSIS UNDER
AXISYMMTRIC LOADING

One of the most important parameters affecting the FEA simulation of a cavitation instability is model size, L/D, which is defined as the ratio of a height of the cylindrical model to the cavity radius as illustrated in Figures 5.10. Here, we studied an effect of model sizes on the FEA prediction of a cavitation instability in constrained silver under axisymmetric loading by using the ABAQUS/Standard program. It provided both an arc-length solver and rezoning mesh capability.

The finite element mesh consisted of two zones. The first zone is a spherical zone surrounding the cavity in which mesh density (number of elements per a unit volume) was kept fixed throughout FEA simulations for various model sizes (i.e., the outer radius of this zone is 350 cavity radii from the cavity center). The second zone is a zone far away from the cavity consisting of a coarse mesh. The material is constrained silver as mentioned in Section 4.3. Figure C.1 illustrates the maximum principal stress at failure for various model sizes. Figure C.2 illustrates the remote total strain at failure for various model sizes. It was found that with a sufficiently large model size (i.e., $L/D = 15,000$), we have a cavitation instability similar to that of an infinite model size. Unfortunately, for $\sigma_2/\sigma_1 < 0.5$ a simulation appeared to have difficulty determining the exact cavitation instability state because of rapid deterioration of the mesh along the boundaries during the onset of instability.

(a)
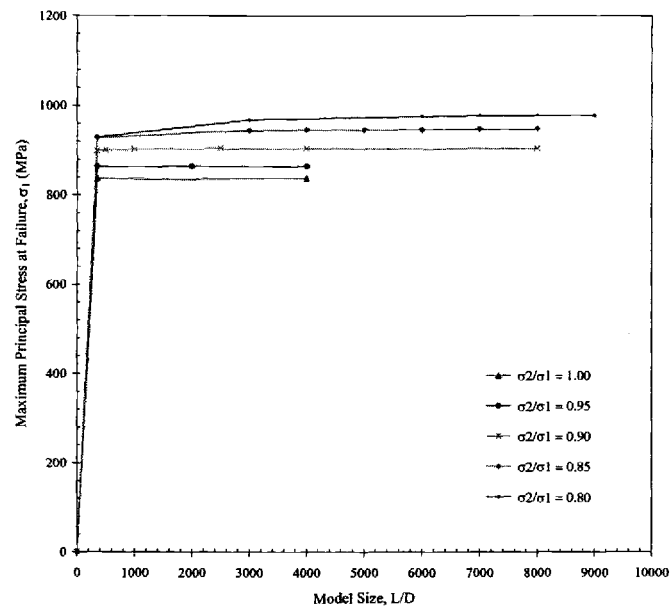
(b)
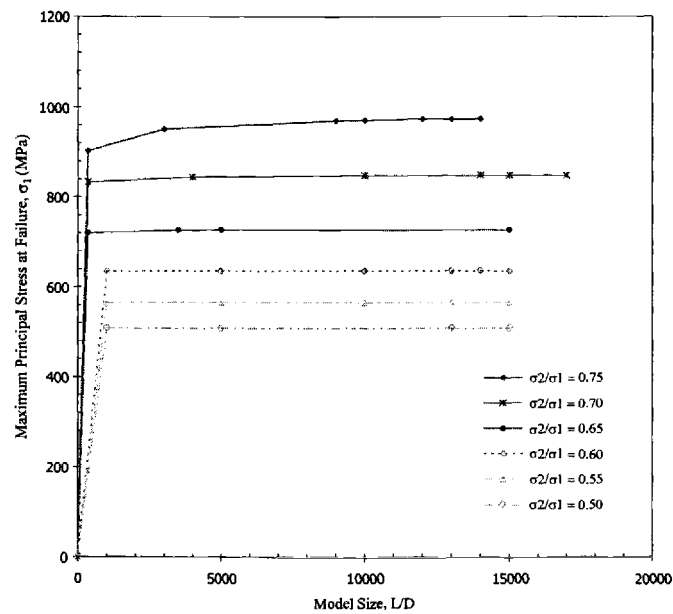
Figure C.1 The maximum principal stress at failure for various model sizes under axisymmetric loading with constrained silver for (a) $0.8 \leq \sigma_2/\sigma_1 \leq 1$ and (b) $0.5 \leq \sigma_2/\sigma_1 \leq 0.75$.

(a)
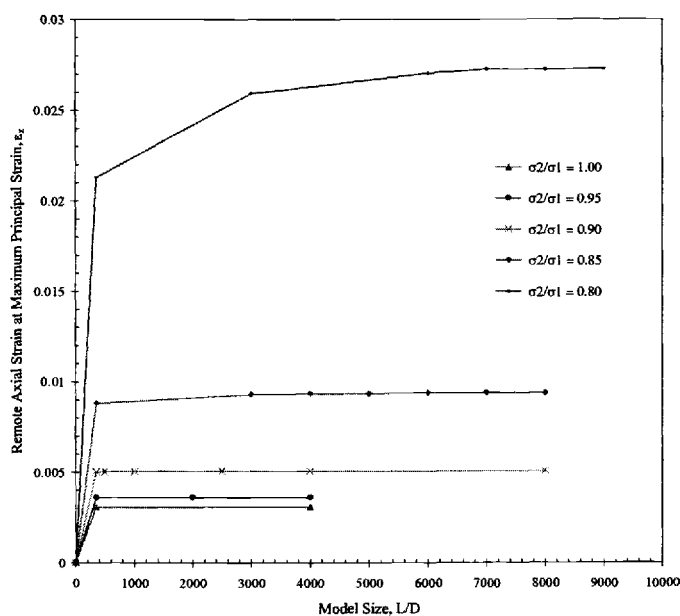
(b)
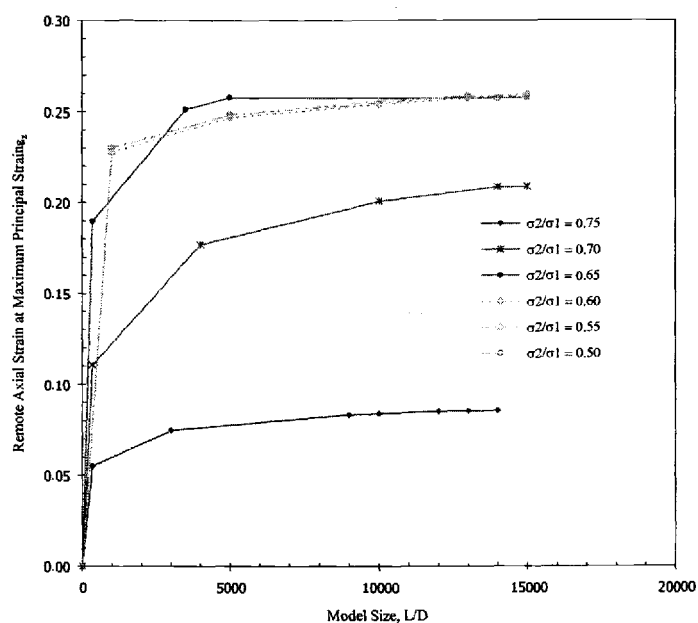
Figure C.2 The remote total strain at the at failure under axisymmetric loading for various model sizes with constrained silver for (a) $0.8 \leq \sigma_2/\sigma_1 \leq 1$ and (b) $0.5 \leq \sigma_2/\sigma_1 \leq 0.75$.

APPENDIX D
NUMERICAL SUBROUTINES USED FOR SOLUTIONS IN CHAPTERS 3
AND 5

This section contains Matlab input files used for solutions of quasi-static and dynamic analyses of a cavitation instability under spherically-symmetric loading as discussed in Chapter 3. These files are orderly printed and results are displayed according to figure numbers listed in Chapters 3.

D.1 INPUT FILE: fig0303.m

```
%% Figure 3.3 (fig0303.m)
clc
clear all
%%
%% Input Variables
%%
Et=10e6;  % Young's Modulus
Y=40e3;   % Yield Stress
nu=0.33;  % Poisson's Ratio
alpha=Y*(1+nu)/3/Et;
beta=2*(1-2*nu)*Y/Et;
S_cr=2/3*(1+log(1/(1-(1-beta)*(1-alpha)^3))/(1-beta))-.001;
point=100;
x=linspace(0,S_cr,point);
y=exp(-x./2+1/3).*(((exp((-1+beta)*(1.5*x-1))-1)/(1-beta)+(1-
alpha)^3*ones(1,point)).^(-1/3));
xlimit=[S_cr S_cr];
ylimit=[1 5];
plot(x,y,'-',xlimit,ylimit,'--')
xlabel('Load Factor, \sigma_\infty/Y','fontname','times','fontsize',12)
ylabel('Cavity Expansion, a/a_0','fontname','times','fontsize',12)
axis([0 4.5 1 5])
text(4,1.25,'S_c_r/Y','fontname','times','fontsize',12)
```

D.2. INPUT FILES: fig0306.m and file0306a.m

D.2.1 Input file: fig0306.m

```
%% Figure 3.6, 5.32, and 5.33
clear all
clc
%%
%% The numerical solution of a cavity expansion with combining inertia and
%% strain-rate effects under sudden spherically-symmetric loading.
%%
%% Input Parameters in U.S. units
%%
E=10e6;   % Young's Modulus (psi)
Yo=40e3;  % Yield Stress (psi)
p=2.59E-4; % Density (lb-sec^2/in^4)
%C=0.;     % Linear Strain Rate coefficient (sec)
S=163094; % Cavitation Stress (psi)
%Scr=(2*Yo/3*(1+log(2*E/3/Yo))); % S=1.02Scr; %S=0.98*Scr;
%%
%% Initial condition for figure 3.6
%%
par=[0 .2556019441824866E-5; 0.00001 .26018221312627E-5; 0.0001
.29905841698617E-5; 0.01 .129826237014004E-4];
%%
%% Initial condition for figure 5.33
%%
%par=[0 .2556019441824866E-5];
%t1=.13759506853707388E-4;% at c=0.1; S=163,094 psi
%t1=.136728406085636E-4;   % at c=0.05; S=163,094 psi
%t1=.129826237014004E-4;   % at c=0.01; S=163,094 psi
%t1=.121385467178408E-4;   % at c=0.005; S=163,094 psi
%t1=.29905841698617E-5;    % at c=0.0001; S=163,094 psi
%t1=.26018221312627E-5;    % at c=0.00001; S=163,094 psi
%%
%% Initial condition for figure 5.32
%%
%t1=.13759624347297987E-4; %at c=0.1; S=159,831.3572 psi (0.98xScr)
%t1=.13759571261500932E-4; %at c=0.1; S=166,355.0860 psi (1.02xScr)
%t1=.129838052453635874E-4;%at c=0.0; S=159,831.3572 psi (0.98xScr)
%t1=.129815055509798785E-4;%at c=0.01; S=166,355.0860 psi (1.02xScr)
tf=10; %Final time for numerical solution
```

```
solu=[];
for i=1:length(par)
    C=par(i,1);
    t1=par(i,2);
    a1=1+.75*S/E*(1-cos((4*E/3/p)^0.5*t1));
    a1dot=S*(3/4/E/p)^0.5*sin((4*E/3/p)^0.5*t1);
    %%
    %% Numerical Method Using ODE45
    %%
    options_1=odeset('RelTol',1E-8,'AbsTol',[1E-8 1E-8]);
    [t,a]=ode45('fig0306a',[t1,tf],[a1;a1dot],options_1,S,C,E,Yo,p);
    %C_m=C*ones(length(t),1)
    %solu=[solu; C_m t a]
    subplot(2,1,1)
    plot(t,a(:,1),'-')
    % Title('The Dynamic Analysis of Cavity Expansion in an Incompressible
Solid','fontsize',12)
    xlabel('Time (sec)','fontsize',11)
    ylabel('Cavity Expansion, a/a_0','fontsize',11)
    hold on
    subplot(2,1,2)
    plot(t,a(:,2),'-')
    axis([0 tf 0 200])
    xlabel('Time (sec)','fontsize',11)
    ylabel('Velocity of Cavity Expansion (in/sec)','fontsize',11)
    hold on
end
legend('C = 0 sec','C = 1x10^-5 sec','C = 1x10^-4 sec','C = 1x10^-2 sec')
Legend('boxoff')
% legend('C = 0.005 sec','C = 0.01 sec','C = 0.05 sec','C = 0.1 sec')
% save c:\data.txt solu -ascii -double -tabs
```

D.2.2 Input file: fig0306a.m

```
function out3=fig0306a(t,a,dummy,S,C,E,Yo,p)
% Define an ODE equation
%%
out3=[a(2);1/p/a(1)*(S-(2*Yo*E*(1-1/a(1)^3)/3/(E*(1-1/a(1)^3)-
(3*Yo*C*a(2)/a(1))))-(2*Yo/3)*(log(2/3/Yo*(E*(1-1/a(1)^3)-
(3*Yo*C*a(2)/a(1))))-(2*C*a(2)/a(1))*(3*Yo/(2*(E*(1-1/a(1)^3)-
(3*Yo*C*a(2)/a(1))))-1))-(1.5*p*a(2)^2))];
```

D.3 INPUT FILE: fig0307.m

```
%% Figure 3.7 (fig0307.m)
clear
clc
%%
%% The numerical solution of a cavity expansion with only strain effects
%%
%% Input Parameters
%%
E=10e6;    % Young's Modulus (psi)
Yo=40e3;  % Yield Stress (psi)
S=163094; % Cavitation Stress (psi)
C=0.05;      % Linear Strain Rate Coefficient (sec)
%%
%% Initial conditions
%%
ic=[0.01 1.01254010679 259.0043125698026; 0.05  1.0125402
51.7066490672265; 0.1 1.012541 25.75405576254178 ];
%%
%% Set numerical accuracy
%%
errx=1E-9;
erry=1E-9;
erryy=1000;
errxx=erryy;
Max_iter=1000;
for i=1:length(ic)
  C=ic(i,1);
  ao=ic(i,2);
  adot_o=ic(i,3);
  adot=[];
  solu=[0 0 ao adot_o];
  f=[];
  gdot=[];
  gdot(1)=0;
  t_step=0;
%%
%% Guess initial solution to start Secant Method
%%
  delta_t=1E-4;
  tf=1.;
  a=ao+delta_t*adot_o;
```

```matlab
    adot(1)=adot_o;
    adot(2)=adot_o-5;
    n=tf/delta_t;
    j=1;
%%
%% The Secant Method
%%
for i=1:n
    f(1)=(S-(2*Yo*E*(1-1/a^3)/3/(E*(1-1/a^3)-(3*Yo*C*adot(1)/a)))-
(2*Yo/3)*(log(2/3/Yo*(E*(1-1/a^3)-(3*Yo*C*adot(1)/a)))-
(2*C*adot(1)/a)*(3*Yo/(2*(E*(1-1/a^3)-(3*Yo*C*adot(1)/a)))-1)))*1E20;
    f(2)=(S-(2*Yo*E*(1-1/a^3)/3/(E*(1-1/a^3)-(3*Yo*C*adot(2)/a)))-
(2*Yo/3)*(log(2/3/Yo*(E*(1-1/a^3)-(3*Yo*C*adot(2)/a)))-
(2*C*adot(2)/a)*(3*Yo/(2*(E*(1-1/a^3)-(3*Yo*C*adot(2)/a)))-1))))*1E20;
    while abs(errxx) >= errx | abs(erryy) >= erry
            gdot(j+1)=(f(j+1)-f(j))/(adot(j+1)-adot(j))/1E20;
            adot(j+2)=adot(j+1)-f(j+1)/gdot(j+1)/1E20;
            f(j+2)=(S-(2*Yo*E*(1-1/a^3)/3/(E*(1-1/a^3)-(3*Yo*C*adot(j+2)/a)))-
(2*Yo/3)*(log(2/3/Yo*(E*(1-1/a^3)-(3*Yo*C*adot(j+2)/a)))-
(2*C*adot(j+2)/a)*(3*Yo/(2*(E*(1-1/a^3)-(3*Yo*C*adot(j+2)/a)))-1)))*1E20;
            erryy=(f(j+2)-f(j+1))/1E20;
            errxx=adot(j+2)-adot(j+1);
            adotf=adot(j+2);
            if j>=Max_iter
               break
            end
            j=j+1;
    end
    format long g
    t_step=i*delta_t;
    solu=[solu; j+1 t_step a adotf];
    a=a+delta_t*adotf;
    j=1;
    adot(1)=adotf+0.2;
    adot(2)=adotf-0.2;
    errxx=100;
    erryy=errxx;
end
subplot(2,1,1)
plot(solu(:,2),solu(:,3));
xlabel('Time (sec)','fontsize',11)
ylabel('Cavity Expansion, a/a_0','fontsize',11)
hold on
subplot(2,1,2)
```

```
plot(solu(:,2),solu(:,4));
axis([0 tf 0 50])
xlabel('Time (sec)','fontsize',11)
ylabel('Velocity of Cavity Expansion (in/sec)','fontsize',11)
hold on
end
legend('C = 0.01 sec','C = 0.05 sec', 'C = 0.1 sec','boxoff')
legend('boxoff')
```

D.4 INPUT FILES: fig0308.m and fig0308a.m

D.4.1 Input file: fig0308.m

```
%% Figure 3.8-3.10
clear all
clc
%%
%% The numerical solution of a cavity expansion without strain-rate effects under
%% sudden spherically-symmetric loading.
%%
%% Input Variables in U.S. units
%%
E=10e6;      % Young's Modulus (psi)
Yo=40e3;    % Yield Stress (psi)
p=2.59E-4;  % Density (lb-sec^2/in^4)
C=0.;        % Linear Strain Rate Coefficients (sec)
%S=158000; % Cavitation Stress (psi)
%S=(2*Yo/3*(1+log(2*E/3/Yo))); % Cavitation limit Stress (psi)
S=163094;
%%
%% Initial conditions at the onset of Yielding on the cavity surface
%%
t1=(0.75*p/E)^0.5*acos(1-(2*Yo/3/S));
a1=(1+Yo/2/E);
a1dot=(S*Yo/E/p*(1-Yo/3/S))^0.5;
%%
%% Numerical Method Using ODE45
%%
tf=0.01; % Final time of numerical solution
options_1=odeset('RelTol',1E-8,'AbsTol',[1E-8 1E-8]);
[t,a]=ode45('strn02',[t1,tf],[a1;a1dot],options_1,S,C,E,Yo,p);
```

```
z=num2str(S);
subplot(2,1,1)
plot(t,a(:,1),'-')
Title('The Dynamic Analysis of Cavitation Instabilities','fontsize',12)
xlabel('Time (sec)','fontsize',12)
ylabel('Cavity Expansion, a/a_0','fontname','times','fontsize',12)
hold on
subplot(2,1,2)
plot(t,a(:,2),'-')
axis([0 tf 0 10,000])
xlabel('Time (sec)','fontname','times','fontsize',12)
ylabel('Velocity of Cavity Expansion (in/sec)','fontname','times','fontsize',12)
hold on
data=[t,a];
n=size(data)
%save c:\data_c05s.txt data -ascii -double -tabs
```

D.5 INPUT FILES: fig0311.m and fig0311a.m

D.5.1 Input file: fig0311.m

```
%% Figure 3.11 (fig0311.m)
clear all
clc
%%
%% The response of the dynamic system in a finite solid body with strain-rate
%% effects. The structure is subjected to step loading at time t=0.
%%
%% Input Variables in U.S. units
%%
E=10e6;     % Young Modulus (psi)
Yo=40e3;    % Yield Stress (psi)
p=2.59E-4;  % Density (lb-sec^2/in^4)
C=0.;       % Linear Strain Rate Coefficient (sec)
S=163094;   % Cavitation Stress (psi)
size=[300 500 1000 10^16];
%%
%% Initial conditions at the onset of yielding on the cavity wall
%%
t1=(0.75*p/E)^0.5*acos(1-(2*Yo/3/S));
```

```
a1=(1+Yo/2/E);
a1dot=(S*Yo/E/p*(1-Yo/3/S))^0.5;
%%
%%Numerical Method Using ODE45
%%
tf=0.03; % Final time of numerical solution
for i=1:length(size)
    b=size(i);
    options_1=odeset('RelTol',1E-8,'AbsTol',[1E-8 1E-8]);
    [t,a]=ode45('fig0311a',[t1,tf],[a1;a1dot],options_1,S,C,E,Yo,p,b);
    plot(t,a(:,1),'-')
    xlabel('Time (sec)','fontsize',12)
    ylabel('Cavity Exp ansion, a/a_0')
    hold on
end
legend('L/D = 300','L/D = 500','L/D = 1000','L/D = \infty',2)
```

D.5.1 Input file: fig0311a.m

```
function out3=fig0311a(t,a,dummy,S,C,E,Yo,p,b)
% Define an ODE equation
%%
out3=[a(2);1/p/a(1)/(1-a(1)/b)*(S-(2*Yo/3)*(1+log(2/3/Yo*E*(1-1/a(1)^3))-
2/3*E/Yo/b^3*(a(1)^3-1))-(0.5*p*a(2)^2)*(3-4*a(1)/b+a(1)^4/b^4))];
```

APPENDIX E
ABAQUS INPUT FILES AND REZONING SUBROUTINES

This section contains ABAQUS input files and rezoning subroutines used in the finite element analyses presented in Chapter 5. These files are orderly printed and results are displayed according to figure numbers listed in Chapter 5. The other input files that are not shown in this section can be obtained directly from the author.

E.1 QUASI-STATIC ANALYSIS UNDER SPHERICALLY-SYMMETRIC LOADING

E.1.1 Input file: static1.inp

```
*HEADING
Cavitation Instabilities
**
**Figure 5.2 (nu = 0.3)
**
**NODAL COORDINATES
**
*NODE
1,1.,0.
21,0.,1.
8001,350.,0
8021,0.,350
10000,0.,0
*NGEN,LINE=C
1,21,1,10000
8001,8021,1,10000
*NSET,NSET=DOWNN,GENERATE
1,21,1
*NSET,NSET=UPP,GENERATE
8001,8021,1
```

```
*NFILL, BIAS=0.88, TWO STEP
DOWNN,UPP,80,100
*NSET,NSET=TOP,GENERATE
8001,8021,1
*NSET,NSET=BOTTOM,GENERATE
1,8001,100
*NSET,NSET=LEFT,GENERATE
21,8021,100
*NSET,NSET=NODEOUT
1,21
**
**ELEMENT CONNECTIVITY
**
*ELEMENT,TYPE=CAX8R
1,1,201,203,3,101,202,103,2
*ELGEN,ELSET=ALLE
1,40,200,1,10,2,40
*ELSET,ELSET=TOPE,GENERATE
40,400,40
*ELSET,ELSET=ELOUT
400
**
**MATERIAL PROPERTIES
**
*SOLID SECTION,MATERIAL=SILVER, ELSET=ALLE
*MATERIAL,NAME=SILVER
*ELASTIC,TYPE=ISOTROPIC
71.E3,0.3
*PLASTIC,HARDENING=ISOTROPIC
213,0.
**
**HISTORY DATA
**
*STEP,NLGEOM,INC=400
*STATIC,RIKS
0.005,1.,0.,0.1,4.,1,1,5.
**
**BOUNDARY CONDITIONS
**
*BOUNDARY
BOTTOM,YSYMM
LEFT,XSYMM
**
**LOADS
```

```
**
*DLOAD
TOPE,P2,-10000.
**
**OUTPUT REQUESTS
**
*RESTART,WRITE,FREQUENCY=400
*NODE PRINT,FREQUENCY=0
*EL PRINT,FREQUENCY=0
*MONITOR,NODE=1,DOF=1
*OUTPUT,FIELD,VARIABLE=PRESELECT
*OUTPUT,FIELD,OP=NEW
*NODE OUTPUT, NSET=UPP
COORD
*NODE OUTPUT, NSET=TOP
COORD
*OUTPUT, HISTORY,FREQ=1
*ELEMENT OUTPUT,ELSET=ELOUT
LE, S
*NODE OUTPUT, NSET=NODEOUT
U
*EL PRINT,ELSET=ELOUT
S,E
*END STEP
```

E.1.2 Input file: static1x.inp

```
*HEADING
Cavitation Instabilities
**
**Figure 5.5 (nu = 0.3)
**
**NODAL COORDINATES
**
*NODE
1,1.,0
21,0.,1.
8001,350.,0.
8021,0.,350.
10000,0.,0.
*NGEN,LINE=C
```

```
1,21,1,10000
8001,8021,1,10000
*NSET,NSET=DOWNN,GENERATE
1,21,1
*NSET,NSET=UPP,GENERATE
8001,8021,1
*NFILL, BIAS=0.88, TWO STEP
DOWNN,UPP,80,100
*NSET,NSET=TOP,GENERATE
8001,8021,1
*NSET,NSET=BOTTOM,GENERATE
1,8001,100
*NSET,NSET=LEFT,GENERATE
21,8021,100
*NSET,NSET=NODEOUT
1,21
**
**ELEMENT CONNECTIVITY
**
*ELEMENT,TYPE=CAX8R
1,1,201,203,3,101,202,103,2
*ELGEN,ELSET=ALLE
1,40,200,1,10,2,40
*ELSET,ELSET=TOPE,GENERATE
40,400,40
*ELSET,ELSET=ELOUT
400
**
**MATERIAL PROPERTIES
**
*SOLID SECTION,MATERIAL=SILVER, ELSET=ALLE
*MATERIAL,NAME=SILVER
*ELASTIC,TYPE=ISOTROPIC
71.E3,0.3
*PLASTIC,HARDENING=ISOTROPIC
213,0.
213213,497.
**
**HISTORY DATA
**
*STEP,NLGEOM,INC=1000
*STATIC,RIKS
0.005,1.,1E-5,0.01,4.,1,1,25.
**
```

```
**BOUNDARY CONDITIONS
**
*BOUNDARY
BOTTOM,YSYMM
LEFT,XSYMM
**
**LOADS
**
*DLOAD
TOPE,P1,-10000.
**
**OUTPUT REQUESTS
**
*RESTART,WRITE,FREQUENCY=400
*NODE PRINT,FREQUENCY=0
*EL PRINT,FREQUENCY=0
*MONITOR,NODE=1,DOF=1
*OUTPUT,FIELD,VARIABLE=PRESELECT
*OUTPUT,FIELD,OP=NEW
*NODE OUTPUT, NSET=UPP
COORD
*NODE OUTPUT, NSET=TOP
COORD
*OUTPUT, HISTORY,FREQ=1
*ELEMENT OUTPUT,ELSET=ELOUT
LE, S
*NODE OUTPUT, NSET=NODEOUT
U
*EL PRINT,ELSET=ELOUT
S,E
*END STEP
```

E.2 QUASI-STATIC ANALYSIS UNDER AXISYMMETRIC LOADING

E.2.1 Input file: test100y02.inp

```
*HEADING
CAVITATION INSTABILITIES
```

```
**
**Figure 5.9-5.14 (Stress ratio = 1 and m = 0.0006)
**
**NODAL COORDINATES
**
*NODE
1,1.,0.
25,0.,1.
8001,300.,0.
8025,0.,300.
12001,5000.,0.
12013,5000.,5000.
12025,0.,5000.
100000,0.,0.
*NGEN,LINE=C
1,25,1,100000
8001,8025,1,100000
**NGEN
**12013,12025,1
*NSET,NSET=N12001
12001
*NSET,NSET=N12013
12013
*NSET,NSET=N12025
12025
*NFILL,BIAS=.95,TWO STEP
N12001,N12013,12,1
*NFILL,BIAS=.95,TWO STEP
N12025,N12013,12,-1
*NSET,NSET=DOWNN,GENERATE
1,25,1
*NSET,NSET=UPP1,GENERATE
8001,8025,1
*NSET,NSET=UPP2,GENERATE
12001,12025,1
*NFILL, BIAS=0.9, TWO STEP
DOWNN,UPP1,80,100
*NFILL, BIAS=0.87, TWO STEP
UPP1,UPP2,40,100
*NSET,NSET=TOP,GENERATE
12013,12025,1
*NSET,NSET=BOTTOM,GENERATE
1,12001,100
*NSET,NSET=LEFT,GENERATE
```

```
25,12025,100
*NSET,NSET=UP,GENERATE
12001,12013,1
*NSET,NSET=UPP,GENERATE
8001,8025,1
12001,12025,1
*NSET,NSET=NODEOUT
1,25
*NSET,NSET=CONTR_UP,GENERATE
12001,12012,1
*NSET,NSET=CONTR_TOP,GENERATE
12014,12025,1
**
**ELEMENT CONNECTIVITY
**
*ELEMENT,TYPE=CAX8R
1,1,201,203,3,101,202,103,2
481,8001,8201,8203,8003,8101,8202,8103,8002
*ELGEN,ELSET=ALLE
1,40,200,1,12,2,40
481,20,200,1,12,2,20
*ELSET,ELSET=TOPE,GENERATE
620,720,20
*ELSET,ELSET=UPE,GENERATE
500,600,20
*ELSET,ELSET=ELOUT
620
**
**MATERIAL PROPERTIES
**
*SOLID SECTION,MATERIAL=SILVER, ELSET=ALLE
*MATERIAL,NAME=SILVER
*ELASTIC,TYPE=ISOTROPIC
71.E3,0.3
*PLASTIC,HARDENING=ISOTROPIC
213,0.
213213,497.
**
**HISTORY DATA
**
***EQUATION
**2
**CONTR_TOP,2,1.,12013,2,-1.
**2
```

```
**CONTR_UP,1,1.,12013,1,-1.
*STEP,NLGEOM,INC=1000
*STATIC,RIKS
0.005,1.,1E-5,0.01,4.,1,1,25.
*CONTROLS,PARAMETERS=FIELD
0.5E-4,,,,,,,,,
*CONTROLS,PARAMETERS=TIME INCREMENTATION
25,25,25,30,,16,,
**
**BOUNDARY CONDITIONS
**
*BOUNDARY
BOTTOM,YSYMM
LEFT,XSYMM
**
**LOADS
**
*DLOAD
UPE, P2,-10000.
TOPE,P2,-10000.
**
**OUTPUT REQUESTS
**
*RESTART,WRITE,FREQUENCY=1000
*NODE PRINT,FREQUENCY=0
*EL PRINT,FREQUENCY=0
*MONITOR,NODE=1,DOF=1
*OUTPUT,FIELD,VARIABLE=PRESELECT
*OUTPUT,FIELD,OP=NEW
*NODE OUTPUT, NSET=UPP
COORD
*NODE OUTPUT, NSET=DOWNN
COORD
*OUTPUT, HISTORY,FREQ=1
*ELEMENT OUTPUT,ELSET=ELOUT
LE, S
*NODE OUTPUT, NSET=NODEOUT
U
*EL PRINT,ELSET=ELOUT
S,E
*END STEP
```

E.2.2 Input file: tr100z03.inp

```
*HEADING
CAVITATION INSTABILITIES
**
**Figure 5.16-5.19 (Stress ratio = 1)
**
**NODAL COORDINATES
**
*NODE
1,1.,0.
25,0.,1.
8001,200.,0.
8025,0.,200.
12001,15000.,0.
12013,15000.,15000.
12025,0.,15000.
100000,0.,0.
*NGEN,LINE=C
1,25,1,100000
8001,8025,1,100000
**NGEN
**12013,12025,1
*NSET,NSET=N12001
12001
*NSET,NSET=N12013
12013
*NSET,NSET=N12025
12025
*NFILL,BIAS=0.85,TWO STEP
N12001,N12013,12,1
*NFILL,BIAS=.85,TWO STEP
N12025,N12013,12,-1
*NSET,NSET=DOWNN,GENERATE
1,25,1
*NSET,NSET=UPP1,GENERATE
8001,8025,1
*NSET,NSET=UPP2,GENERATE
12001,12025,1
*NFILL, BIAS=0.90, TWO STEP
DOWNN,UPP1,80,100
*NFILL, BIAS=0.8, TWO STEP
```

```
UPP1,UPP2,40,100
*NSET,NSET=TOP,GENERATE
12013,12025,1
*NSET,NSET=BOTTOM,GENERATE
1,12001,100
*NSET,NSET=LEFT,GENERATE
25,12025,100
*NSET,NSET=UP,GENERATE
12001,12013,1
*NSET,NSET=UPP,GENERATE
8001,8025,1
12001,12025,1
*NSET,NSET=NODEOUT
1,25
*NSET,NSET=CONTR_UP,GENERATE
12001,12012,1
*NSET,NSET=CONTR_TOP,GENERATE
12014,12025,1
**
**ELEMENT CONNECTIVITY
**
*ELEMENT,TYPE=CAX8R
1,1,201,203,3,101,202,103,2
481,8001,8201,8203,8003,8101,8202,8103,8002
*ELGEN,ELSET=ALLE
1,40,200,1,12,2,40
481,20,200,1,12,2,20
*ELSET,ELSET=TOPE,GENERATE
620,720,20
*ELSET,ELSET=UPE,GENERATE
500,600,20
*ELSET,ELSET=ELOUT
620
**
**MATERIAL PROPERTIES
**
*SOLID SECTION,MATERIAL=SILVER, ELSET=ALLE
*MATERIAL,NAME=SILVER
*ELASTIC,TYPE=ISOTROPIC
71.E3,0.45
*PLASTIC,HARDENING=ISOTROPIC
213,0.
220,0.000315645
230,0.000839192
```

240,0.00145529
250,0.002172158
260,0.002998366
270,0.003942834
280,0.005014831
290,0.006223978
300,0.007580242
310,0.009093944
320,0.010775752
330,0.012636684
340,0.014688108
350,0.016941744
360,0.019409658
370,0.022104269
380,0.025038344
390,0.028225001
400,0.031677706
410,0.035410276
420,0.039436879
430,0.04377203
440,0.048430596
450,0.053427794
460,0.058779188
470,0.064500695
480,0.07060858
490,0.077119459
500,0.084050296
525,0.103329197
550,0.125622123
575,0.151222847
600,0.180438807
625,0.213591103
650,0.251014502
700,0.340081984
750,0.450592653
800,0.585716528
850,0.748842253
900,0.943577094
950,1.173746935
1000,1.443396288
1050,1.756788284
1100,2.118404675
1150,2.532945837
1200,3.005330769

```
**
**HISTORY DATA
**
***EQUATION
**2
**CONTR_TOP,2,1.,12013,2,-1.
**2
**CONTR_UP,1,1.,12013,1,-1.
*STEP,NLGEOM,INC=400
*STATIC,RIKS
0.01,1.,0.0001,0.1,2.,1,1,14.
*CONTROLS,PARAMETERS=FIELD
.5E-4,,,,,,,,
*CONTROLS,PARAMETERS=TIME INCREMENTATION
14,15,15,30,,,,
**
**BOUNDARY CONDITIONS
**
*BOUNDARY
BOTTOM,YSYMM
LEFT,XSYMM
**
**LOADS
**
*DLOAD
UPE,P2,-1000.
TOPE,P2,-1000.
**
**OUTPUT REQUESTS
**
*RESTART,WRITE,FREQUENCY=400
*NODE PRINT,FREQUENCY=0
*EL PRINT,FREQUENCY=0
*MONITOR,NODE=1,DOF=1
*OUTPUT,FIELD,VARIABLE=PRESELECT
*OUTPUT,FIELD,OP=NEW
*NODE OUTPUT, NSET=UPP
COORD
*NODE OUTPUT, NSET=DOWNN
COORD
*OUTPUT, HISTORY,FREQ=1
*ELEMENT OUTPUT,ELSET=ELOUT
LE, S
*NODE OUTPUT, NSET=NODEOUT
```

U
*EL PRINT,ELSET=ELOUT
S,E
*END STEP

E.2.2 Input file: or100f01.inp

*HEADING
CAVITATION INSTABILITIES
**
**Figure 5.21-5.24 (Stress ratio = 1)
**
**
**NODAL COORDINATES
**
*NODE
1,1.,0.
25,0.,1.
8001,200.,0.
8025,0.,200.
11001,4000.,0.
11013,4000.,4000.
11025,0.,4000.
100000,0.,0.
*NGEN,LINE=C
1,25,1,100000
8001,8025,1,100000
**NGEN
**11013,11025,1
*NSET,NSET=N11001
11001
*NSET,NSET=N11013
11013
*NSET,NSET=N11025
11025
*NFILL,BIAS=0.98,TWO STEP
N11001,N11013,12,1
*NFILL,BIAS=.98,TWO STEP
N11025,N11013,12,-1
*NSET,NSET=DOWNN,GENERATE
1,25,1

```
*NSET,NSET=UPP1,GENERATE
8001,8025,1
*NSET,NSET=UPP2,GENERATE
11001,11025,1
*NFILL, BIAS=0.90, TWO STEP
DOWNN,UPP1,80,100
*NFILL, BIAS=0.8, TWO STEP
UPP1,UPP2,30,100
*NSET,NSET=TOP,GENERATE
11013,11025,1
*NSET,NSET=BOTTOM,GENERATE
1,11001,100
*NSET,NSET=LEFT,GENERATE
25,11025,100
*NSET,NSET=UP,GENERATE
11001,11013,1
*NSET,NSET=UPP,GENERATE
8001,8025,1
11001,11025,1
*NSET,NSET=NODEOUT
1,25
*NSET,NSET=CONTR_UP,GENERATE
11001,11012,1
*NSET,NSET=CONTR_TOP,GENERATE
11014,11025,1
**
**ELEMENT CONNECTIVITY
**
*ELEMENT,TYPE=CAX8R
1,1,201,203,3,101,202,103,2
481,8001,8201,8203,8003,8101,8202,8103,8002
*ELGEN,ELSET=ALLE
1,40,200,1,12,2,40
481,15,200,1,12,2,15
*ELSET,ELSET=TOPE,GENERATE
585,660,15
*ELSET,ELSET=UPE,GENERATE
495,570,15
*ELSET,ELSET=ELOUT
585
**
**MATERIAL PROPERTIES
**
*SOLID SECTION,MATERIAL=SILVER, ELSET=ALLE
```

```
*MATERIAL,NAME=SILVER
*ELASTIC,TYPE=ISOTROPIC
71.E3,0.37
*PLASTIC,HARDENING=ISOTROPIC
49.7,0.,70
100,0.001,70
115,0.002,70
139,0.004,70
153,0.006,70
164,0.00799,70
171,0.00999,70
182,0.01404,70
193,0.01998,70
208,0.02997,70
219,0.04002,70
233,0.06002,70
244,0.07996,70
251,0.09996,70
254,0.15002,70
256,0.19999,70
259,2.99635,70
260,99.99634,70
**
**HISTORY DATA
**
***EQUATION
**2
**CONTR_TOP,2,1.,11013,2,-1.
**2
**CONTR_UP,1,1.,11013,1,-1.
*STEP,NLGEOM,INC=400
*STATIC,RIKS
0.01,1.,0.0001,0.1,2.,1,1,10.
*CONTROLS,PARAMETERS=FIELD
.5E-4,,,,,,,,
*CONTROLS,PARAMETERS=TIME INCREMENTATION
14,15,15,30,,,,
**
**BOUNDARY CONDITIONS
**
*BOUNDARY
BOTTOM,YSYMM
LEFT,XSYMM
**
```

```
**LOADS
**
*DLOAD
UPE,P2,-1000.
TOPE,P2,-1000.
**
**OUTPUT REQUESTS (INC=100 is the last increment.)
**
*RESTART,WRITE,FREQUENCY=400
*NODE PRINT,FREQUENCY=0
*EL PRINT,FREQUENCY=0
*MONITOR,NODE=1,DOF=1
*OUTPUT,FIELD,VARIABLE=PRESELECT
*OUTPUT,FIELD,OP=NEW
*NODE OUTPUT, NSET=UPP
COORD
*NODE OUTPUT, NSET=DOWNN
COORD
*OUTPUT, HISTORY,FREQ=1
*ELEMENT OUTPUT,ELSET=ELOUT
LE, S
*NODE OUTPUT, NSET=NODEOUT
U
*EL PRINT,ELSET=ELOUT
S,E
*END STEP
```

E.3 ABAQUS SUBROUTINES

```
"""
Reads the output database file and imports the deformed shape of
the billet at the end of step 1 as an orphan mesh part.  The
orphan mesh part is then used to create a 2D solid part which
can be meshed by the user.
"""
from abaqus import *
from part import *

# NOTE:  USER MUST DEFINE THESE VARIABLES.
odbName = 'or100f01.odb'   # Name of output database file.
modelName = 'Model-1'       # Model name.
```

```
orphanInstance = 'PART-1-1'   # Deformed instance name.
deformedShape = DEFORMED     # Shape.
angle = 15.0              # Feature angle.
importStep = 1            # Step number.

# Import orphan mesh part.
orphanBillet = mdb.model['Model-1'].PartFromOdb(fileName=odbName,
                              name='orphanBillet',
                              instance=orphanInstance,
                              shape=deformedShape,
                              step=importStep)

# Extract 2D profile and create a solid part.
newBillet = mdb.model['Model-1'].Part2DGeomFrom2DMesh(name='newBillet',
                              part=orphanBillet,
                              featureAngle=angle)

print 'Deformed billet is now ready for rezoning.'
```

E.4 DYNAMIC ANALYSIS UNDER SPHERICALLY-SYMMETRIC LOADING

E.4.1 Input file: model0600c01sh02.inp

```
*HEADING
Cavity Expansion
**
**Figure 5.26 (S = 1.02 Scr and C = 0.1 sec)
**
*PARAMETER
delta_x=1000*cos(10*pi/180)
delta_y=1000*sin(10*pi/180)
**
**NODAL COORDINATES
**
*NODE,SYSTEM=C
1,1.,0.
2,1.,10
5001,600.,0.
5002,600.,10.
5101,1200.,0
```

```
5102,1200.,10.
10000,0.,0.
*NGEN,LINE=C
1,2,1,10000
5001,5002,1,10000
*NSET,NSET=DOWNN,GENERATE
1,2,1
*NSET,NSET=UPP,GENERATE
5001,5002,1
*NFILL, BIAS=0.87, TWO STEP
DOWNN,UPP,50,100
*NSET,NSET=BOTTOM,GENERATE
1,5001,100
*NSET,NSET=TOP,GENERATE
2,5002,100
*NSET,NSET=NODEOUT
1
*TRANSFORM,NSET=TOP,TYPE=R
<delta_x>,<delta_y>,0.,-<delta_y>,<delta_x>,0.
**
**ELEMENT CONNECTIVITY
**
*ELEMENT,TYPE=CAX4R
1,1,101,102,2
*ELGEN,ELSET=ALLE
1,50,100,1,1,1,50
*ELEMENT,TYPE=CINAX4,ELSET=INF
51,5002,5001,5101,5102
*ELSET,ELSET=UPE
50
*ELSET,ELSET=FMASS,GENERATE
1,901,50
*SOLID SECTION,ELSET=ALLE,MATERIAL=SILVER
1.,
*SOLID SECTION,ELSET=INF,MATERIAL=SILVER
2.,
**
**MATERIAL PROPERTIES
**
*MATERIAL,NAME=SILVER
*DENSITY
2.59E-4,
*ELASTIC,TYPE=ISOTROPIC
10E6,0.486
```

```
*PLASTIC
4E4,0.
*RATE DEPENDENT
10,1
**
**BOUNDARY CONDITIONS
**
*BOUNDARY
BOTTOM,YSYMM
TOP,YSYMM
*AMPLITUDE,NAME=RAMP,DEFINITION=SMOOTH STEP
0.,0.,4.5E-6,166355.086,10,166355.086
**
**STEP
**
*STEP,NLGEOM=YES
Step-1
*DYNAMIC,EXPLICIT
,1.
*BULK VISCOSITY
1.4,1.2
*ADAPTIVE MESH,ELSET=ALLE,CONTROLS=T1,MESH SWEEPS=3
*ADAPTIVE MESH CONTROLS,NAME=T1,SMOOTHING=GRADED
**FIXED MASS SCALING, FACTOR=1,ELSET=FMASS
*DLOAD,AMPLITUDE=RAMP
UPE,P2,-1
**
**OUTPUT REQUESTS
**
*RESTART,WRITE,NUMBER INTERVAL=1,TIME MARK=NO
*MONITOR,DOF=1,NODE=1
*OUTPUT,FIELD,NUMBER INTERVAL=200,VARIABLE=PRESELECT
*OUTPUT,HISTORY,VARIABLE=PRESELECT
*ENERGY OUTPUT
ALLAE, ALLCD, ALLFD, ALLIE, ALLKE,
ALLPD, ALLSE, ALLVD, ALLWK, ETOTAL
*OUTPUT,HISTORY,TIME INTERVAL=.005
*NODE OUTPUT,NSET=NODEOUT
U
*ELEMENT OUTPUT,ELSET=UPE
MISES,S,SP,LE
*END STEP
```

E.4.2 Input file: dyhard020c00.inp

```
*HEADING
Cavity Expansion
**
**Figure 5.28 (S = 163,094 psi)
**
**NODAL COORDINATES
**
*NODE
1,1.,0.
21,0.,1.
5001,300.,0.
5021,0.,300.
10000,0.,0.
*NGEN,LINE=C
1,21,1,10000
5001,5021,1,10000
*NSET,NSET=DOWNN,GENERATE
1,21,1
*NSET,NSET=UPP,GENERATE
5001,5021,1
*NFILL, BIAS=0.9, TWO STEP
DOWNN,UPP,50,100
*NSET,NSET=TOP,GENERATE
5001,5021,1
*NSET,NSET=BOTTOM,GENERATE
1,5001,100
*NSET,NSET=LEFT,GENERATE
21,5021,100
*NSET,NSET=NODEOUT
1,21
**
**ELEMENT CONNECTIVITY
**
*ELEMENT,TYPE=CAX4R
1,1,101,102,2
*ELGEN,ELSET=ALLE
1,50,100,1,20,1,50
*ELSET,ELSET=TOPE,GENERATE
50,1000,50
*ELSET,ELSET=ELOUT
```

```
550
*ELSET,ELSET=FMASS,GENERATE
 1,951,50
 2,952,50
 3,953,50
 4,954,50
 5,955,50
 6,956,50
 7,957,50
 8,958,50
 9,959,50
10,960,50
*SOLID SECTION,ELSET=ALLE,MATERIAL=SILVER
1.,
**
**MATERIAL PROPERTIES
**
*MATERIAL,NAME=SILVER
*DENSITY
2.59E-4,
*ELASTIC,TYPE=ISOTROPIC
10E6,0.499
*PLASTIC
4E4,0.
**RATE DEPENDENT
**2,1
**
**BOUNDARY CONDITIONS
**
*BOUNDARY
BOTTOM,YSYMM
LEFT,XSYMM
*AMPLITUDE,NAME=RAMP,DEFINITION=SMOOTH STEP
0.,0.,4.4797E-6,163094,10,163094
**
**STEP
**
*STEP,NLGEOM=YES
Step-1
*DYNAMIC,EXPLICIT
,0.017
*BULK VISCOSITY
.2,.12
*ADAPTIVE MESH,ELSET=ALLE,CONTROLS=T1,MESH SWEEPS=4
```

```
*ADAPTIVE MESH CONTROLS,NAME=T1,SMOOTHING=GRADED
*FIXED MASS SCALING, FACTOR=14,ELSET=AllE
*DLOAD,AMPLITUDE=RAMP
TOPE,P2,-1
**
**OUTPUT REQUESTS
**
*RESTART,WRITE,NUMBER INTERVAL=1,TIME MARK=NO
*MONITOR,DOF=1,NODE=1
*OUTPUT,FIELD,NUMBER INTERVAL=17,VARIABLE=PRESELECT
*OUTPUT,HISTORY,VARIABLE=PRESELECT
*ENERGY OUTPUT
ALLAE, ALLCD, ALLFD, ALLIE, ALLKE,
ALLPD, ALLSE, ALLVD, ALLWK, ETOTAL
*OUTPUT,HISTORY,TIME INTERVAL=.001
*NODE OUTPUT,NSET=NODEOUT
U
*ELEMENT OUTPUT,ELSET=ELOUT
MISES,S,SP,LE
*END STEP
*STEP,NLGEOM=YES
Step-2
*DYNAMIC,EXPLICIT
,0.184
*BULK VISCOSITY
.6,1.2
*ADAPTIVE MESH,ELSET=ALLE,CONTROLS=T2,MESH SWEEPS=1
*ADAPTIVE MESH CONTROLS,NAME=T2,CURVATURE REFINEMENT=10
*FIXED MASS SCALING, FACTOR=440,ELSET=ALLE
*DLOAD,AMPLITUDE=RAMP
TOPE,P2,-1
**
**OUTPUT REQUESTS
**
*RESTART,WRITE,NUMBER INTERVAL=1,TIME MARK=NO
*MONITOR,DOF=1,NODE=1
*OUTPUT,FIELD,NUMBER INTERVAL=41,VARIABLE=PRESELECT
*OUTPUT,HISTORY,VARIABLE=PRESELECT
*ENERGY OUTPUT
ALLAE, ALLCD, ALLFD, ALLIE, ALLKE,
ALLPD, ALLSE, ALLVD, ALLWK, ETOTAL
*OUTPUT,HISTORY,TIME INTERVAL=.004
*NODE OUTPUT,NSET=NODEOUT
U
```

```
*ELEMENT OUTPUT,ELSET=ELOUT
MISES,S,SP,LE
*END STEP
```

E.4.3 Input file: dyhardzc010n03.inp

```
*HEADING
Cavity Expansion
**
**Figure 5.30 (S = 163,094 psi and C = 0.1 sec)
**
**NODAL COORDINATES
**
*NODE
1,1.,0.
21,0.,1.
8001,300.,0.
8021,0.,300.
10000,0.,0.
*NGEN,LINE=C
1,21,1,10000
8001,8021,1,10000
*NSET,NSET=DOWNN,GENERATE
1,21,1
*NSET,NSET=UPP,GENERATE
8001,8021,1
*NFILL, BIAS=0.89, TWO STEP
DOWNN,UPP,80,100
*NSET,NSET=TOP,GENERATE
8001,8021,1
*NSET,NSET=BOTTOM,GENERATE
1,8001,100
*NSET,NSET=LEFT,GENERATE
21,8021,100
*NSET,NSET=NODEOUT
1,21
**
**ELEMENT CONNECTIVITY
**
*ELEMENT,TYPE=CAX8RH
1,1,201,203,3,101,202,103,2
```

```
*ELGEN,ELSET=ALLE
1,40,200,1,10,2,40
*ELSET,ELSET=TOPE,GENERATE
40,400,40
*ELSET,ELSET=ELOUT
400
**
**MATERIAL PROPERTIES
**
*SOLID SECTION,ELSET=ALLE,MATERIAL=SILVER
*MATERIAL,NAME=SILVER
*ELASTIC,TYPE=ISOTROPIC
10E6,0.499
*PLASTIC
4E4,0.
*RATE DEPENDENT
10,1
**
**BOUNDARY CONDITIONS
**
*BOUNDARY
BOTTOM,YSYMM
LEFT,XSYMM
*AMPLITUDE,NAME=STEP,DEFINITION=SMOOTH STEP
0.,163094,100,163094
**
**STEP
**
*STEP,NLGEOM=YES,AMPLITUDE=STEP,INC=1000
Step-1
*STATIC
1E-8,30
*DLOAD,AMPLITUDE=STEP
TOPE,P2,-1
*CONTROLS,PARAMETERS=FIELD
1E-4,,,,,,,,
*CONTROLS,PARAMETERS=TIME INCREMENTATION
100,100,100,100,50,,,
**25,25,25,30,,16,,
**
**OUTPUT REQUESTS
**
*RESTART,WRITE,FREQUENCY=1000
*NODE PRINT,FREQUENCY=0
```

```
*EL PRINT,FREQUENCY=0
*MONITOR,NODE=1,DOF=1
*OUTPUT,FIELD,VARIABLE=PRESELECT
*OUTPUT,FIELD,OP=NEW
*NODE OUTPUT, NSET=UPP
COORD
*NODE OUTPUT, NSET=DOWNN
COORD
*OUTPUT, HISTORY,FREQ=10
*ELEMENT OUTPUT,ELSET=ELOUT
LE, S
*NODE OUTPUT, NSET=NODEOUT
U
*EL PRINT,ELSET=ELOUT
S,E
*END STEP
```

E.4.4 Input file: special100n01z.inp

```
*HEADING
Cavity Expansion
**
**Figure 5.32 (S = 1.02Scr)
**
**NODAL COORDINATES
**
*NODE
1,1.,0.
21,0.,1.
5001,300.,0.
5011,300.,300.
5021,0.,300.
10000,0.,0.
*NGEN,LINE=C
1,21,1,10000
*NGEN
5001,5011,1
5011,5021,1
*NSET,NSET=DOWNN,GENERATE
1,21,1
*NSET,NSET=UPP,GENERATE
```

```
5001,5021,1
*NFILL, BIAS=0.9, TWO STEP
DOWNN,UPP,50,100
*NSET,NSET=TOP,GENERATE
5011,5021,1
*NSET,NSET=BOTTOM,GENERATE
1,5001,100
*NSET,NSET=LEFT,GENERATE
21,5021,100
*NSET,NSET=UP,GENERATE
5001,5011,1
*NSET,NSET=NODEOUT
1
*NSET,NSET=CONTR_UP,GENERATE
5002,5011,1
*NSET,NSET=CONTR_TOP,GENERATE
5011,5020,1
**
**ELEMENT CONNECTIVITY
**
*ELEMENT,TYPE=CAX4R
1,1,101,102,2
*ELGEN,ELSET=ALLE
1,50,100,1,20,1,50
*ELSET,ELSET=UPE,GENERATE
50,500,50
*ELSET,ELSET=TOPE,GENERATE
550,1000,50
*ELSET,ELSET=ELOUT
550
*ELSET,ELSET=FMASS,GENERATE
 1,951,50
 2,952,50
 3,953,50
 4,954,50
 5,955,50
 6,956,50
 7,957,50
 8,958,50
 9,959,50
10,960,50
*SOLID SECTION,ELSET=ALLE,MATERIAL=SILVER
1.,
**
```

```
**MATERIAL PROPERTIES
**
*MATERIAL,NAME=SILVER
*DENSITY
2.59E-4,
*ELASTIC,TYPE=ISOTROPIC
10E6,0.499
*PLASTIC
4E4,0.
**
**BOUNDARY CONDITIONS
**
*BOUNDARY
BOTTOM,YSYMM
LEFT,XSYMM
*AMPLITUDE,NAME=RAMP,DEFINITION=SMOOTH STEP
0.,0.,4.5E-6,163382.63,5,163382.63
**
**STEP
**
*STEP,NLGEOM=YES
Step-1
*DYNAMIC,EXPLICIT
,0.017
*BULK VISCOSITY
.2,1.2
*ADAPTIVE MESH,ELSET=ALLE,CONTROLS=T1,MESH SWEEPS=4
*ADAPTIVE MESH CONTROLS,NAME=T1,SMOOTHING=GRADED
*FIXED MASS SCALING, FACTOR=18,ELSET=AllE
*DLOAD,AMPLITUDE=RAMP
TOPE,P2,-1
UPE,P2,-1
**
**OUTPUT REQUESTS
**
*RESTART,WRITE,NUMBER INTERVAL=1,TIME MARK=NO
*MONITOR,DOF=1,NODE=1
*OUTPUT,FIELD,NUMBER INTERVAL=17,VARIABLE=PRESELECT
*OUTPUT,HISTORY,VARIABLE=PRESELECT
*ENERGY OUTPUT
ALLAE, ALLCD, ALLFD, ALLIE, ALLKE,
ALLPD, ALLSE, ALLVD, ALLWK, ETOTAL
*OUTPUT,HISTORY,TIME INTERVAL=.001
*NODE OUTPUT,NSET=NODEOUT
```

U
*ELEMENT OUTPUT,ELSET=ELOUT
MISES,S,SP,LE
*END STEP
*STEP,NLGEOM=YES
Step-2
*DYNAMIC,EXPLICIT
,0.184
*BULK VISCOSITY
.6,1.2
*ADAPTIVE MESH,ELSET=ALLE,CONTROLS=T2,MESH SWEEPS=1
*ADAPTIVE MESH CONTROLS,NAME=T2,CURVATURE REFINEMENT=10
*FIXED MASS SCALING, FACTOR=430,ELSET=ALLE
*DLOAD,AMPLITUDE=RAMP
TOPE,P2,-1
UPE,P2,-1
**
**OUTPUT REQUESTS
**
*RESTART,WRITE,NUMBER INTERVAL=1,TIME MARK=NO
*MONITOR,DOF=1,NODE=1
*OUTPUT,FIELD,NUMBER INTERVAL=41,VARIABLE=PRESELECT
*OUTPUT,HISTORY,VARIABLE=PRESELECT
*ENERGY OUTPUT
ALLAE, ALLCD, ALLFD, ALLIE, ALLKE,
ALLPD, ALLSE, ALLVD, ALLWK, ETOTAL
*OUTPUT,HISTORY,TIME INTERVAL=.004
*NODE OUTPUT,NSET=NODEOUT
U
*ELEMENT OUTPUT,ELSET=ELOUT
MISES,S,SP,LE
*END STEP

E.4.5 Input file: test100n01z.inp

*HEADING
Cavity Expansion
**
**Figure 5.35 (S = 1.02Scr)
**
**NODAL COORDINATES

```
**
*NODE
1,1.,0.
25,0.,1.
8001,300.,0.
8025,0.,300.
12001,10000.,0.
12013,10000.,10000.
12025,0.,10000.
100000,0.,0.
*NGEN,LINE=C
1,25,1,100000
8001,8025,1,100000
*NSET,NSET=N12001
12001
*NSET,NSET=N12013
12013
*NSET,NSET=N12025
12025
*NFILL,BIAS=.95,TWO STEP
N12001,N12013,12,1
*NFILL,BIAS=.95,TWO STEP
N12025,N12013,12,-1
*NSET,NSET=DOWNN,GENERATE
1,25,1
*NSET,NSET=UPP1,GENERATE
8001,8025,1
*NSET,NSET=UPP2,GENERATE
12001,12025,1
*NFILL, BIAS=0.9, TWO STEP
DOWNN,UPP1,80,100
*NFILL, BIAS=0.87, TWO STEP
UPP1,UPP2,40,100
*NSET,NSET=TOP,GENERATE
12013,12025,1
*NSET,NSET=BOTTOM,GENERATE
1,12001,100
*NSET,NSET=LEFT,GENERATE
25,12025,100
*NSET,NSET=UP,GENERATE
12001,12013,1
*NSET,NSET=UPP,GENERATE
8001,8025,1
12001,12025,1
```

```
*NSET,NSET=NODEOUT
1,25
*NSET,NSET=CONTR_UP,GENERATE
12001,12012,1
*NSET,NSET=CONTR_TOP,GENERATE
12014,12025,1
**
**ELEMENT CONNECTIVITY
**
*ELEMENT,TYPE=CAX8RH
1,1,201,203,3,101,202,103,2
481,8001,8201,8203,8003,8101,8202,8103,8002
*ELGEN,ELSET=ALLE
1,40,200,1,12,2,40
481,20,200,1,12,2,20
*ELSET,ELSET=TOPE,GENERATE
620,720,20
*ELSET,ELSET=UPE,GENERATE
500,600,20
*ELSET,ELSET=ELOUT
620
**
**MATERIAL PROPERTIES
**
*SOLID SECTION,MATERIAL=SILVER,ELSET=ALLE
*MATERIAL,NAME=SILVER
*ELASTIC,TYPE=ISOTROPIC
10E6,0.45
*PLASTIC
4E4,0.
*RATE DEPENDENT
2154.43469,3.333333333
*AMPLITUDE,NAME=STEP,DEFINITION=SMOOTH STEP
0.,163382.63,100,163382.63
**
**HISTORY DATA
**
*STEP,NLGEOM=YES,AMPLITUDE=STEP,INC=1000
Step-1
*STATIC
1E-6,20,1E-6
*CONTROLS,PARAMETERS=FIELD
0.5E-4,,,,,,,,,
*CONTROLS,PARAMETERS=TIME INCREMENTATION
```

```
25,25,25,30,,16,,
**
**BOUNDARY CONDITIONS
**
*BOUNDARY
BOTTOM,YSYMM
LEFT,XSYMM
**
**LOADS
**
*DLOAD,AMPLITUDE=STEP
UPE, P2,-1.
TOPE,P2,-1.
**
**OUTPUT REQUESTS
**
*RESTART,WRITE,FREQUENCY=1000
*NODE PRINT,FREQUENCY=0
*EL PRINT,FREQUENCY=0
*MONITOR,NODE=1,DOF=1
*OUTPUT,FIELD,VARIABLE=PRESELECT
*OUTPUT,FIELD,OP=NEW
*NODE OUTPUT, NSET=UPP
COORD
*NODE OUTPUT, NSET=DOWNN
COORD
*OUTPUT, HISTORY,FREQ=1
*ELEMENT OUTPUT,ELSET=ELOUT
LE, S
*NODE OUTPUT, NSET=NODEOUT
U
*EL PRINT,ELSET=ELOUT
S,E
*END STEP
```

E.4.6 Input file: f100e02.inp

```
*HEADING
Cavity Expansion
**
**Figure 5.38 (Stress ratio = 1)
```

```
**
**
**NODAL COORDINATES
**
*NODE
1,1.,0.
21,0.,1.
5001,300.,0.
5011,300.,300.
5021,0.,300.
10000,0.,0.
*NGEN,LINE=C
1,21,1,10000
*NGEN
5001,5011,1
5011,5021,1
*NSET,NSET=DOWNN,GENERATE
1,21,1
*NSET,NSET=UPP,GENERATE
5001,5021,1
*NFILL, BIAS=0.87, TWO STEP
DOWNN,UPP,50,100
*NSET,NSET=TOP,GENERATE
5011,5021,1
*NSET,NSET=BOTTOM,GENERATE
1,5001,100
*NSET,NSET=LEFT,GENERATE
21,5021,100
*NSET,NSET=UP,GENERATE
5001,5011,1
*NSET,NSET=NODEOUT
1
*NSET,NSET=CONTR_UP,GENERATE
5002,5011,1
*NSET,NSET=CONTR_TOP,GENERATE
5011,5020,1
**
**ELEMENT CONNECTIVITY
**
*ELEMENT,TYPE=CAX4R
1,1,101,102,2
*ELGEN,ELSET=ALLE
1,50,100,1,20,1,50
*ELSET,ELSET=UPE,GENERATE
```

```
50,500,50
*ELSET,ELSET=TOPE,GENERATE
550,1000,50
*ELSET,ELSET=ELOUT
550
*ELSET,ELSET=FMASS,GENERATE
1,951,50
2,952,50
3,953,50
4,954,50
5,955,50
6,956,50
7,957,50
8,958,50
*SOLID SECTION,ELSET=ALLE,MATERIAL=SILVER
1.,
**
**MATERIAL PROPERTIES
**
*MATERIAL,NAME=SILVER
*DENSITY
10490.,
*ELASTIC,TYPE=ISOTROPIC
71000.E+6,0.37
*PLASTIC,HARDENING=ISOTROPIC
49.7E+6,0.
100E+6,0.001
115E+6,0.002
139E+6,0.004
153E+6,0.006
164E+6,0.00799
171E+6,0.00999
182E+6,0.01404
193E+6,0.01998
208E+6,0.02997
219E+6,0.04002
233E+6,0.06002
244E+6,0.07996
251E+6,0.09996
254E+6,0.15002
256E+6,0.19999
256.075E+6,0.26990
256.150E+6,0.33981
256.225E+6,0.40972
```

256.300E+6,0.47963
256.375E+6,0.54954
256.450E+6,0.61944
256.525E+6,0.68935
256.600E+6,0.75926
256.675E+6,0.82917
256.750E+6,0.89908
256.825E+6,0.96899
256.900E+6,1.03890
256.975E+6,1.10881
257.050E+6,1.17872
257.125E+6,1.24862
257.200E+6,1.31853
257.275E+6,1.38844
257.350E+6,1.45835
257.425E+6,1.52826
257.500E+6,1.59817
257.575E+6,1.66808
257.650E+6,1.73799
257.725E+6,1.80790
257.800E+6,1.87781
257.875E+6,1.94772
257.950E+6,2.01762
258.025E+6,2.08753
258.100E+6,2.15744
258.175E+6,2.22735
258.250E+6,2.29726
258.325E+6,2.36717
258.400E+6,2.43708
258.475E+6,2.50699
258.550E+6,2.57690
258.625E+6,2.64680
258.700E+6,2.71671
258.775E+6,2.78662
258.850E+6,2.85653
258.925E+6,2.92644
259E+6,2.99635
**
**BOUNDARY CONDITIONS
**
*BOUNDARY
BOTTOM,YSYMM
LEFT,XSYMM
*AMPLITUDE,NAME=RAMP,SMOOTH=0

```
0.,0.,10.,1.,500.,1.
**
**STEP
**
*STEP,NLGEOM=YES
Step-1
*DYNAMIC,EXPLICIT
,15.
*ADAPTIVE MESH,ELSET=ALLE,CONTROLS=T1,MESH SWEEPS=5
*ADAPTIVE MESH CONTROLS,NAME=T1,SMOOTHING=GRADED
*FIXED MASS SCALING, FACTOR=500,ELSET=FMASS
*DLOAD,AMPLITUDE=RAMP
UPE,P2,-838E+6
TOPE,P2,-838E+6
**
**OUTPUT REQUESTS
**
*RESTART,WRITE,NUMBER INTERVAL=1,TIME MARK=NO
*MONITOR,DOF=1,NODE=1
*OUTPUT,FIELD,NUMBER INTERVAL=100,VARIABLE=PRESELECT
*OUTPUT,HISTORY,VARIABLE=PRESELECT
*Energy Output
ALLAE, ALLCD, ALLFD, ALLIE, ALLKE,
ALLPD, ALLSE, ALLVD, ALLWK, ETOTAL
*OUTPUT,HISTORY,TIME INTERVAL=0.15
*NODE OUTPUT,NSET=NODEOUT
U
*ELEMENT OUTPUT,ELSET=ELOUT
S,SP,LE
*END STEP
```